Master Thesis in Geosciences

Travel time approximations, including higher-order terms, to extend the applicability of Kirchhoff time migration.

Piratheeben Kulathilagan

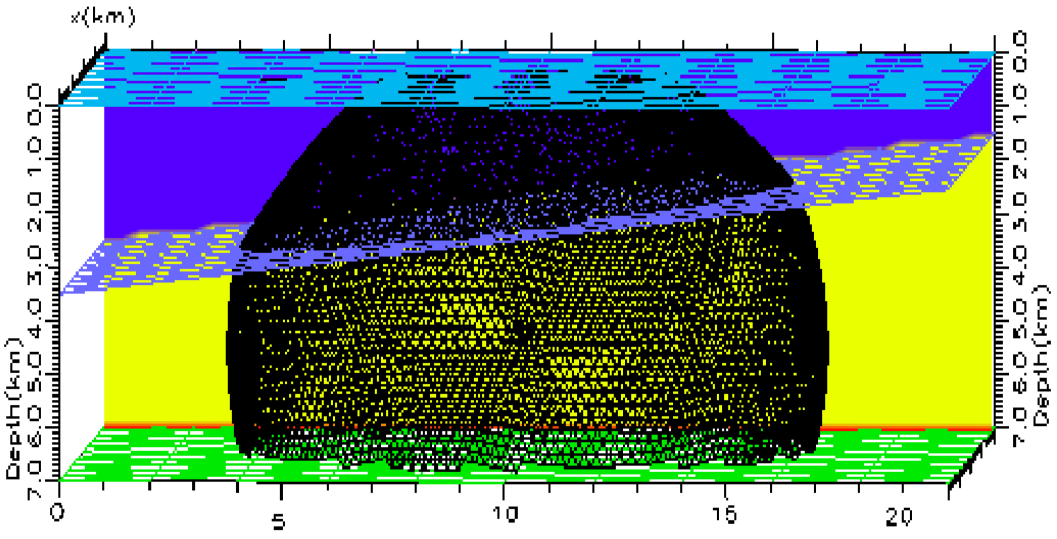

UNIVERSITY OF OSLO
FACULTY OF MATHEMATICS AND NATURAL SCIENCES

Travel time approximations, including higher-order terms, to extend the applicability of Kirchhoff time migration.

Piratheeben Kulathilagan

Master Thesis in Geosciences

Discipline: Geophysics

Department of Geosciences

Faculty of Mathematics and Natural Sciences

UNIVERSITY OF OSLO

01.06.2011

Tutor(s): **Valerie Maupin (UiO) and Einar Iversen (NORSAR)**
This work is published digitally through DUO – Digitale Utgivelser ved UiO
http://www.duo.uio.no
It is also catalogued in BIBSYS (http://www.bibsys.no/english)

Abstract

Seismic time migration is a cost and time effective process for imaging of the subsurface. However, the approach is traditionally limited to velocity models with mildly varying lateral variations.

The objective of the present work is to study the potential for extending the prestack Kirchhoff time migration method to cases where previously depth migration was required, because of lateral velocity variations and/or anisotropy. New additional higher-order terms have been introduced to the conventional double square root (DSR) diffraction-time function. The results of their approximations to diffraction-time surfaces obtained using the NORSAR-3D software have been discussed. Tests have been performed for both isotropic and anisotropic media. For the isotropic media, tests were performed for both vertically varying velocity fields, and also velocity fields dominated by lateral velocity variations. For the anisotropic media, tests have been performed for both vertical transverse isotropic (VTI) and tilted transverse isotropic (TTI) media with varying anisotropy parameter η. Here, the tests were performed on vertically varying velocity fields and when the velocity gradient was tilted 15 degrees with respect to the vertical.

The accuracy of the various diffraction-time surface approximations was determined by the root mean square (RMS) error in seconds. Our results show that additional terms can provide better approximations of the diffraction-time surface. Diffraction-time surfaces corresponding to a vertically varying velocity field are well approximated by symmetric functions of higher-order. This is also true for tests in anisotropic geomodels with a vertical symmetry axis. On the other hand, approximations of simple asymmetric diffraction-time surfaces caused by lateral velocity variation or TTI can benefit from introducing odd terms of higher-order to the DSR function. The results also underscores that additional terms are not a guarantee to achieve good approximations, as the possibility of a good result depends largely on the character of the diffraction-time surface to be approximated.

Our results also show that the diffraction-time surface approximation error is more sensitive to the lateral velocity gradient than to the vertical velocity gradient in isotropic media. Lastly, the effect of changing the axis of symmetry from vertical, to 15 degrees with respect to the vertical for anisotropic media had less impact on the approximation error, than when the velocity gradient was changed similarly.

Acknowledgements

With this I complete my M.Sc. in Geophysics at the University of Oslo.

I would like to show my gratitude to Professor Valerie Maupin at the University of Oslo for being an excellent supervisor. Throughout this work she has been available and helpful. The dedication she shows for her work should set an example for all of us.

A special thanks to Einar Iversen at NORSAR. His guidance and help has been essential for the completion of this thesis. The interest he shows and knowledge he has within the field of seismic signal processing is admirable. Through this work I have also developed an interest for the field, thanks to him.

I would like to thank my good friend Tashi Tshering for interesting discussions and proof reading of this thesis.

Last but not least, I would like to thank my family. They have always supported and encouraged me to pursue my dreams. Whenever I have doubted my abilities my mum, Sivaneswary Kulathilagan, has successfully given me my faith back. The endless love you all show can simply not be described by words.

Table of content

1 Introduction

Seismic reflection profiling is an echo-ranging technique used to measure the distance to subsurface reflectors. In modern seismic marine acquisition the streamer have hydrophones to measure pressure waves, and geophones to measure particle velocities. Shots are fired from the source, and their return signals are recorded by the receivers. The recorded signals can be considered as superpositioned seismic waves. The recorded waves are not necessarily from a reflector directly below the receiver, but can originate from any subsurface location. One of the main steps which modify the image in seismic signal processing is migration. Migration tries to move the observed events back to their true spatial position, and thereby create a more accurate image of the subsurface which eases interpretation compared to an unmigrated image. Migration is an inverse process where the recorded waves are propagated back to the reflector (Gazdag and Sguazzero, 1984). It can be performed on the seismic data before or after stacking, depending on the complexity of the subsurface. Performed before stacking, it is referred to as prestack migration, and accordingly, if performed after stacking it is referred to as post stack migration. Prestack migration is capable of handling more complex structures than post stack migration (Yilmaz, 2001). The term complex structures or complex geology is used in this work to characterize structures which cannot be easily imaged because of their characteristics (Fagin, 1991). Further, the migration procedure which produces a time image is referred to as time migration. Time migration tries to move dipping events from their apparent locations to their true locations in time, while flat events remain flat after the migration process. A migration procedure which produces a depth image is referred to as depth migration. Here, reflections in seismic data are moved to their correct positions in the depth domain.

Travel time approximation plays a vital role in seismic processing and is used for multiple attenuation, velocity analysis, AVO analysis, moveout corrections and time migration among other techniques (Causse, 2004). Considerable effort has been granted to develop travel time equations of higher-order to achieve better approximations in areas with complex geology for the first four procedures mentioned. For example, Fomel and Stovas (2010) developed a non-hyperbolic moveout approximation for both isotropic and anisotropic media. The new function involved five additional coefficients compared to the conventional function, and consequently improved the accuracy by several orders of magnitude. However, higher-order

travel time functions for the purpose of time migrations have received very little attention. Note that most of the developed functions are closely related to the series developed by Taner and Koehler (1969). This is also the case in the present work.

Time migration is a cost and time effective method compared to an equivalent depth migration method. However, lateral velocity variations have traditionally limited the applicability of time migration. It is a well documented phenomenon that lateral velocity variation results in mispositioning of events in time migration (Khare, 1991). By introducing higher-order terms (e.g. 3^{rd}, 4^{th}, 5^{th} and 6^{th}) to the diffraction-time functions, a better approximation of asymmetric diffraction-time surfaces both in isotropic and anisotropic media are believed to be achieved. Asymmetric diffraction-time surfaces corresponding to lateral velocity variations occur often, and should be granted more attention so the applicability of the time migration method can be extended.

In this work 2D prestack Kirchhoff time migration is investigated further to see if, and how diffraction time functions with additional terms (e.g. 3^{rd}, 4^{th}, 5th and 6^{th} order functions) are able to create improved subsurface images, compared to the classical double square root diffraction-time function in both isotropic and anisotropic media. If so, the applicability of prestack Kirchhoff time migration can be extended to work for more complex velocity models, and in particular replace prestack depth migration in cases with lateral velocity variations. This will obviously save time and cost associated with the migration process.

In order to study the approximation obtained by the new functions, both isotropic and anisotropic geomodels were created in NORSAR-3D with varying complexity. Travel times were generated, and the approximation was performed by a non linear least square surface fitting method in MATLAB. It enabled one to quantify the results and also determine the coefficients of the various tested functions. Finally, the results were discussed to determine how many, and which additional terms to include in the modified diffraction-time function. To keep the processing time associated with migration at a minimum it is desirable to keep as few additional terms as possible without reducing the image quality significantly. There is obviously a tradeoff between time and accuracy.

2 Review of seismic migration

Migration is a well established geophysical process and involves geometrical repositioning of returned signals to show an event where it has been scattered or reflected, rather than where it has been picked up (Yilmaz, 2001). The origin of the word in the field of geophysics is however not well documented. It is believed to originate from the geologic conception of how oil migrates up dip (Bednar, 2005). Migrating seismic sections started in the mid 1920's. It was performed by using graphical methods until the 1960's. Between the 1960's and the 1970's diffraction summation and wavefront migration based on ray theory was developed. During the 1970's several other important discoveries in the field of seismic migration were made. A completely different approach to migration based on wave theory was invented. Effective algorithms for downward extrapolation were developed from simplified finite-difference approximations of the wave equations. Processing operations which earlier were only possible in time domain became possible to carry out in the frequency domain by applying Fourier transform. Operating in the frequency domain also proved to be more accurate in the space-time coordinate frame than the finite-difference methods. Great improvements on diffraction summation migration were also made. Today, diffraction summation migration is frequently applied and referred to as Kirchhoff migration (Gazdag and Sguazzero, 1984).

Migration is most useful in areas with complex geology. In *Figure 2.1*, an example is shown for a zero offset section. A dipping reflector is mispositioned if the reflection travel times are plotted along a vertical travel path. The true position of the dipping reflector is obtained by plotting the reflection travel time along the inclined line that correspond to the actual ray path. From this simple illustration one can clearly see that the distortion is not a result of operating with incorrect travel times, but a result of plotting them at incorrect positions, or calculating depths based on correct travel times, and plotting them at incorrect positions.

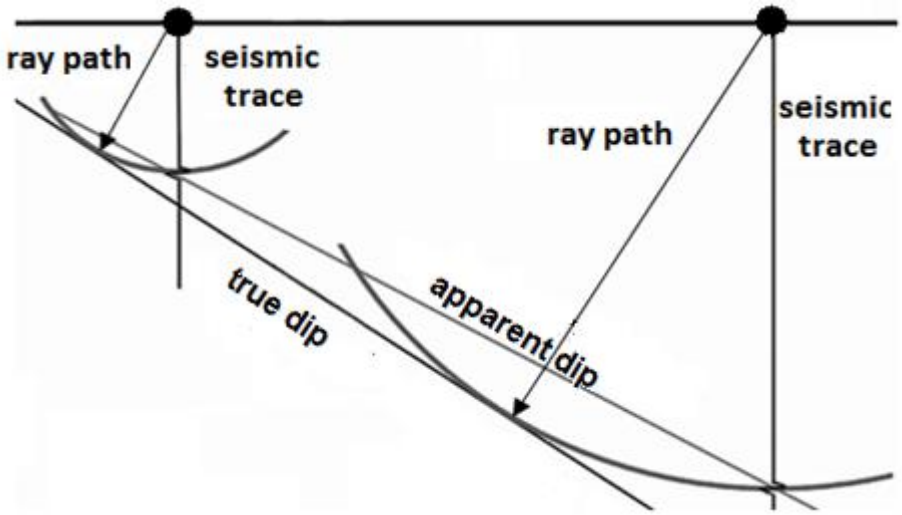

Figure 2.1: *Illustration of how a dipping reflector will be mispositioned if travel times are plotted along the vertical axis, rather than along their actual propagation path (Based on Mari et al, 1999).*

For simple velocity models, time migration is characterized by its ability to obtain focused images in time domain. On the other hand complex velocity models require depth migration. Depth migration is superior when it comes to producing focused structural images in the depth domain for complex velocity models (Khare, 1991; Black and Brzostowski, 1994; Yilmaz, 2001; Iversen and Tygel, 2008). Regardless of the migration approach, they all aim to create a focused image by un-wrapping bowties into synclines, and collapsing diffraction curves to single points. In *Figure 2.2* an un-migrated section (*Figure 2.2a)* and a migrated section (*Figure 2.2b)* are shown. A drastic improvement of the section after the migration procedure is observed. Note how the diffraction curves are collapsed to single points.

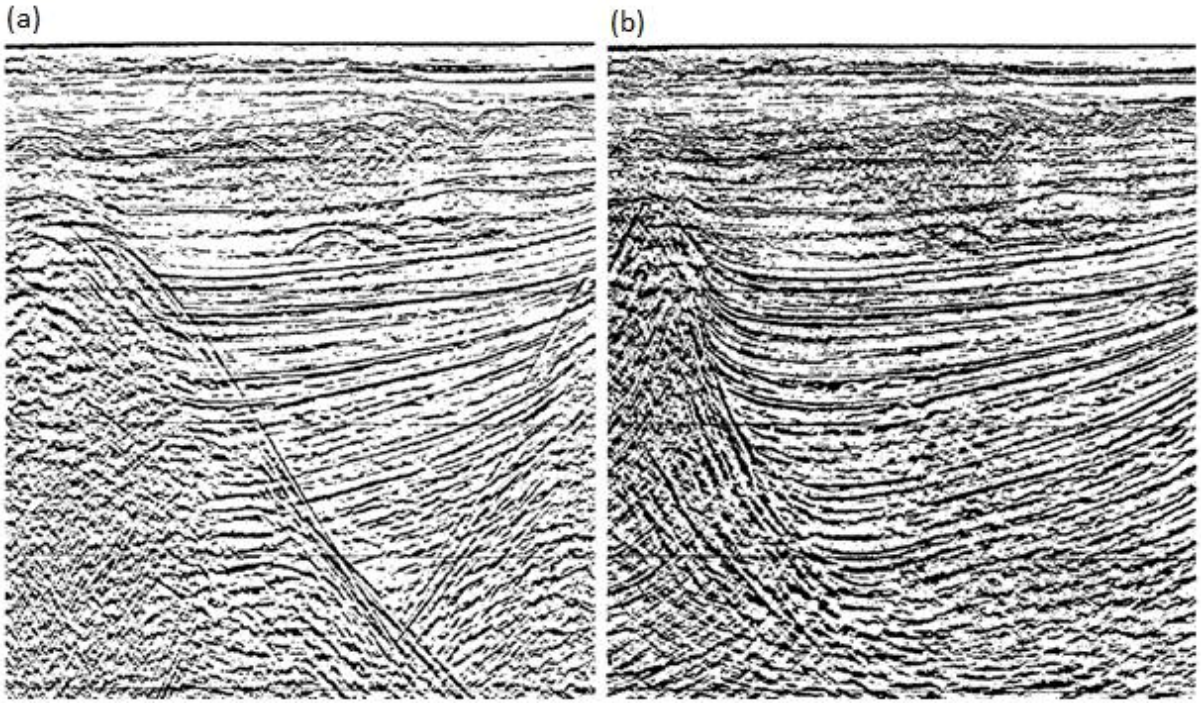

Figure 2.2: Same image before migration (a) and after migration (b). Migration collapses diffraction curves to single points. Also, dipping reflectors are shortened, steepened and moved up dip (Yilmaz, 2001).

Moreover, migration also shortens, steepens, and moves dipping reflectors up dip as can also be seen in the figure above. Thus, a more realistic image of the geology and its geological features are provided to the interpreter. This allows the interpreter to use his or hers expertise without the need to fully understand the applied migration process (Hubral, 1977). However, a migrated section does not always provide a more truthful image of the subsurface. As mentioned, complex velocity models requires depth migration, but if time migration is performed on seismic data with significant lateral velocity variations, the migrated image can be distorted. This is discussed in *Chapter 2.2*.

2.1 Kirchhoff time migration

Yilmaz (2001) stated that "*When the lateral velocity gradients are significant, time migration does not produce the true subsurface image. Instead, we need to use depth migration*". Time migration is frequently used in the industry, and for very good reasons. The main advantages with time migration are that it is cost effective, time effective and also quite robust with respect to the applied velocity field (Iversen and Tygel, 2008). It is robust to the velocity field because it does not require an accurate velocity analysis as compared to an equivalent depth

migration. This is highly advantageous if limited information about the velocity field is available, which is often the case when new prospects are explored. Thus, fairly accurate time images can be created with limited knowledge of the velocity model. Moreover, prestack time migration enables one to perform velocity analysis on the migrated section to assure that the correct velocities were applied in the migration process. The additional possibility to perform a quality control of the migration process has proven to improve the seismic image drastically and has therefore become a part of the standard processing procedure (Robein, 2003). If the wrong migration velocity is applied, the seismic section can either be over or under migrated as shown in *Figure 2.3.* The figure shows a diffraction hyperbola on top, which is collapsed to a single point when the correct migration velocity is used. However, if the migration velocity is too low the hyperbola is undermigrated, as shown from the images on the left. The migration velocity decreases from *c* to *f*. Similarly, if the applied migration velocity is too high, the hyperbola is overmigrated, as shown from the image on the right. Here, the migration velocity increases from *c* to *f*. *Figure 2.3* underscores how important it is to use the correct migration velocity, and also the importance of the additional quality control.

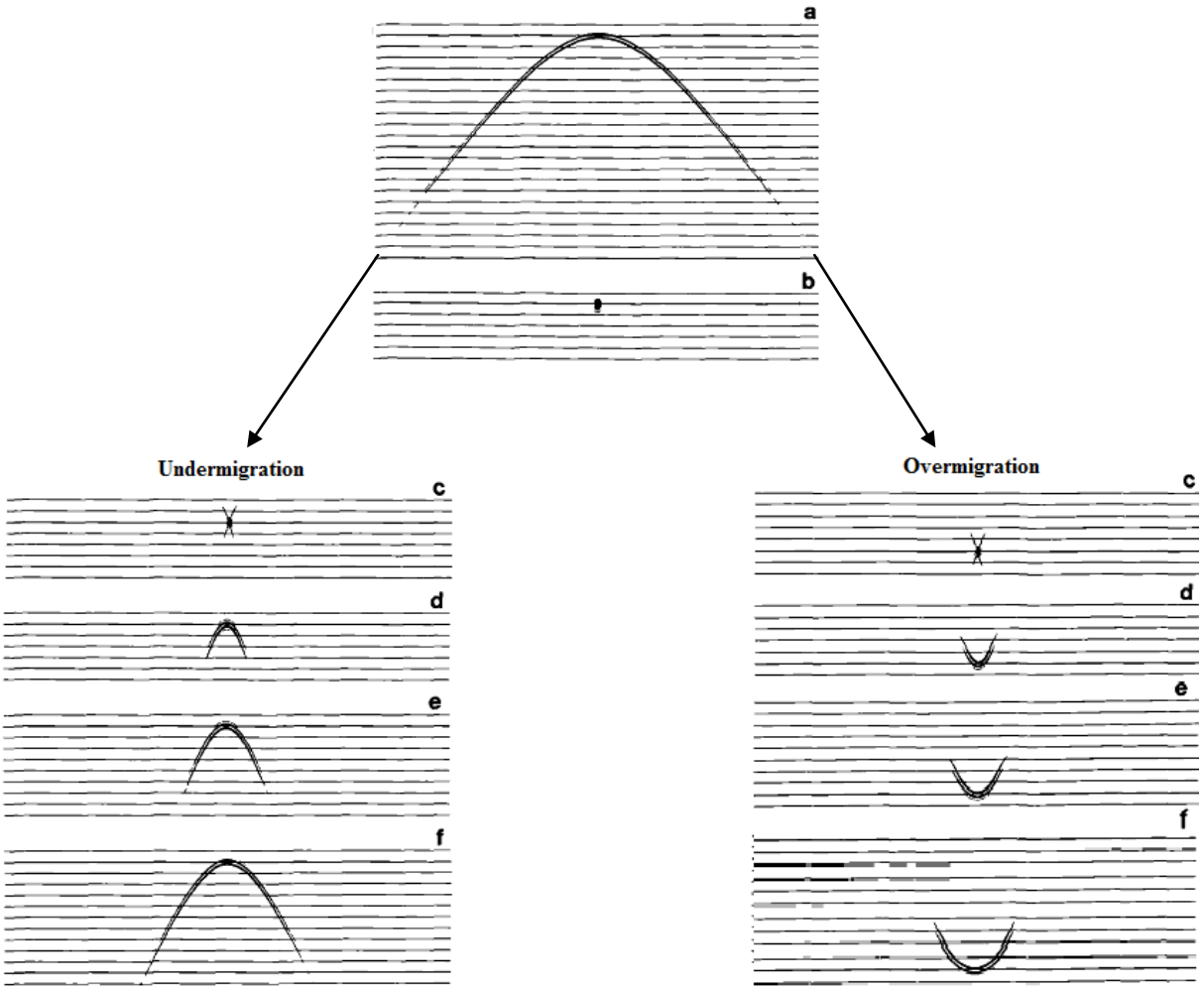

Figure 2.3: Illustration of how a diffraction hyperbola (a) is collapsed to a single point (b) when the correct migration velocity is applied. Sequence to the left, show the result of using too low migration velocities. The applied migration velocity decreases from c to f. The sequence to the right shows the result of using too high migration velocities. The applied migration velocity increases from c to f (Yilmaz, 2001-Modified).

For older producing fields, detailed information about the velocity field is most likely available from core samples, well logs and seismic data. Applying the velocity information from these different methods is not a straight forward process. In *Chapter 3.1* the scaling problem is shortly discussed.

As mentioned, time migration is time effective. A typical depth migration algorithm requires an order of magnitude more computer cycles than a time migration algorithm of comparable ability to preserve steep dips (Black and Brzostowski, 1993). This is significant knowing that

a 3D depth migrated section can take months to produce. In other words, in some cases the lateral velocity variation does not justify the application of depth migration.

Kirchhoff migration is based on the computation of diffraction-time surface over which energy from a subsurface point is scattered (Schneider, 1978). According to the Kirchhoff diffraction integral, input samples are summed directly to an output migrated sample. The migration approach considers a subsurface model to be composed of scatter points that scatter energy from any source to all receivers. Thus, reflectors can be considered as a smooth continuum of scatter points which produces a coherent reflection. The scattered energy which is recorded on the receivers is simply relocated to the position of the scatter point (Bancroft et al, 1998; Zhang et al, 2006). It basically assumes an output location, and then sums the appropriate energy from all available input traces. This procedure is repeated for every output sample in the subsurface model.

2.1.1 Application of Kirchhoff time migration

A graphical illustration and summary of the main steps in Kirchhoff time migration for a zero offset section can be found in *Figure 2.4.* Here, no lateral velocity variation is assumed, but vertical variations are present. Travel times are recorded for a diffraction point (*see Figure 2.4a*). Wave field propagation from any point in a given velocity model to a point at the acquisition surface can be represented by the Green's function. In this work, the high frequency approximation of the Green's function is of interest. The approximation enables one to perform ray tracing in heterogeneous media. The high frequency approximation of the Green's function is given by

$$GF(\vec{r}, \vec{r_s}, t) = A(\vec{r}, \vec{r_s})\delta[t - t(\vec{r}, \vec{r_s})],$$

Eq. 2.1

where A is the amplitude, δ is the initial impulse, t is the travel time, $\vec{r_s}$ is the source location and $\vec{r}$ is the distance between the source and the arbitrary point in depth (Gelius and Johansen, 2010).

Further, the recorded times defines a diffraction-time curve (*see Figure 2.4b*) which is approximated by a hyperbola. After the approximation is done and the diffraction-time curve is defined, a summation process takes place. The energy is summed along the curve, and placed at the apex point (see *Figure 2.4c*). The procedure is repeated for every point in the model.

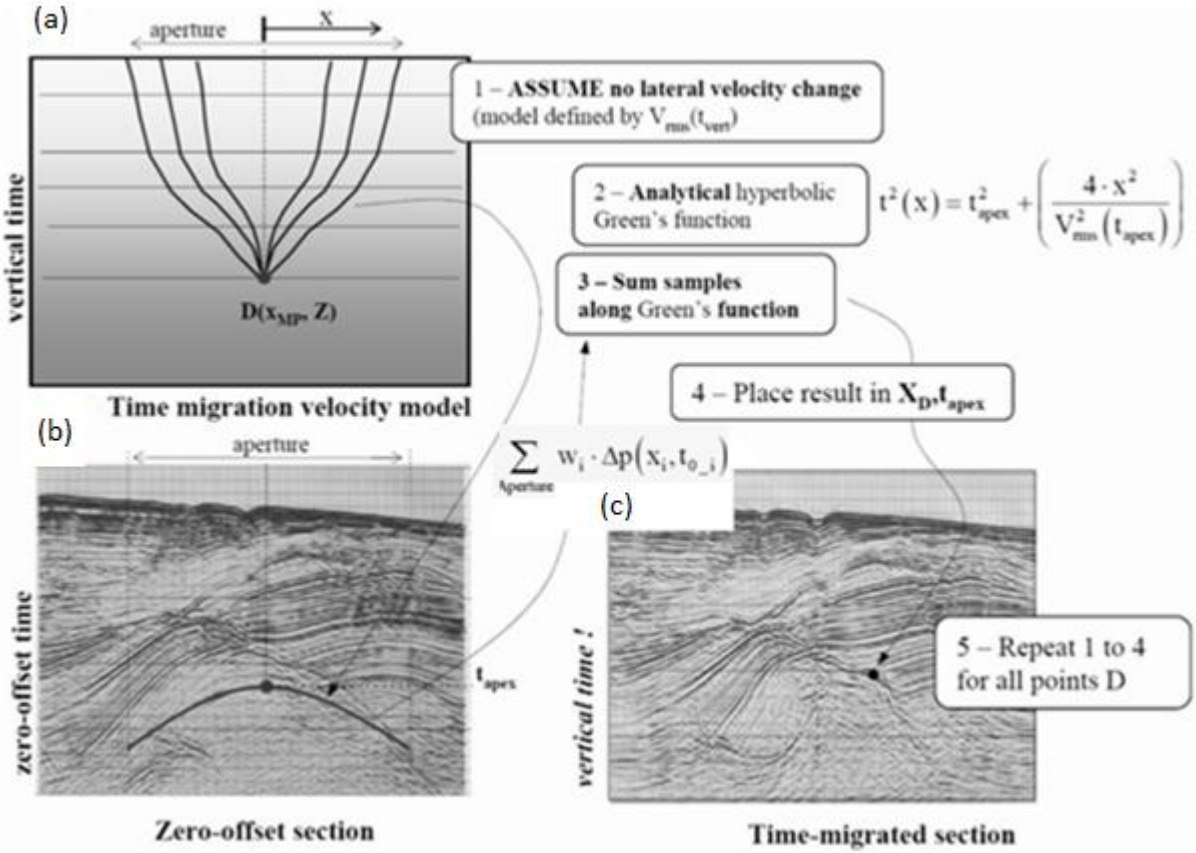

Figure 2.4: Illustration showing the main steps of Kirchhoff time migration on a zero offset section (Robein, 2003). The travel time in the Green's function is approximated by a hyperbola. Values are finally assigned to the apex of the approximated hyperbola.

To better understand how time migration is carried out, it is of interest to study 2D Kirchhoff post stack depth migration, as they have things in common. Consider a point *D* for a given depth model, and a seismic signal of infinite frequency bandwidth. Kirchhoff post stack depth migration sums the data samples along the diffraction-time curve associated with the point *D,* and assign the value to the point *D* (Iversen and Tygel, 2008). Significant values from the operation will be assigned to the point *D* which lies on the reflector, while surrounding areas will be assigned negligible values. In reality, the seismic signal has a limited frequency

bandwidth. Consequently, surrounding areas also contribute with energy which is assigned to the reflector after the migration process (Keydar and Mikenberg, 2010).

Kirchhoff time migration sums data samples along the diffraction-time curve associated with poind *D*, and assigns the value to the apex point of the curve. The operation can be seen on *Figure 2.5* for a diffraction curve. Assigning values to the apex is not unique for Kirchhoff time migration. It is performed for all time migration techniques (Fehler and Huang, 2002). This is done simply because the apex represents the position where a ray from a point *D* in depth emerges vertically to the surface (Hubral, 1977). The vertically emerging ray is called an image ray and represents the stationary travel time from a depth point to the measurement surface. Image rays are only naturally vertical if the overlying medium has constant or only vertically varying velocity field (Hubral, 1977). Note how the image ray emerges vertically on the measurement surface in the figure below, and also how the point *D* is contacted to the apex point by the image ray.

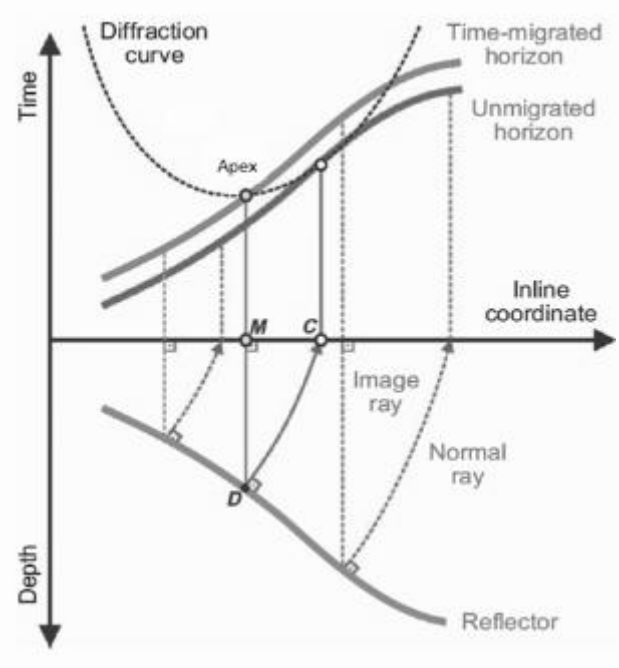

Figure 2.5: Geometrical outline of 2D Kirchhoff migration on a single stacked section. Also shown are normal rays, which are normal to the reflector in depth (Iversen and Tygel, 2008)

Even though it is advantageous to assign values to the apex, it can be complicated. First of all, a clear apex must exist. Lateral velocity variations can produce diffraction-time curves

without a clear apex, which complicates the process. If the values are not assigned to the apex, the outcome will conflict with the fundamental property of time migration. The fundamental property of time migration leaves a flat event unchanged after migration (Black and Brzostowski, 1994). If the values are not correctly positioned on the apex point of the diffraction -time curves, a flat event in depth will not appear flat on the time image after time migration.

2.2 Limitations of time migration

Time migration is the most widely used migration technique. Understanding the main limitations is therefore equally important as understanding the advantages. Understanding both pros and cons can help to avoid pitfalls before one embarks into the migration process. Ignoring limitations can potentially lead to wrong interpretation and understanding of the geological setting.

For complex geological settings where lateral velocity variation occurs, apparent dips can be inverted after the time migration process. It is well known that time migration methods which depend on image rays have steep dip limitations (Khare, 1991). In *Figure 2.6* the dipping reflector, highlighted in yellow, is inverted on the time image compared to the depth image. At the center the images one can also see red arrows illustrating how a dipping reflector is mispositioned on the time image as a result of the complex geology. In addition the thickness of the same layers appears differently on the two images. This is because high velocity layers appear thinner than they actually are, compared to low velocity layers on the time section.

If fast layers are located above the reservoir, time migration can miscalculate the overburden thickness. This will indirectly affect the understanding of the reservoir. On the other hand, if the fast layers are below the reservoir, the effect of the errors associated with the layers will be less significant for the interpretation.

It is worth emphasizing that the errors shown on *Figure 2.6* cannot be discovered before a depth migration of the same section is performed.

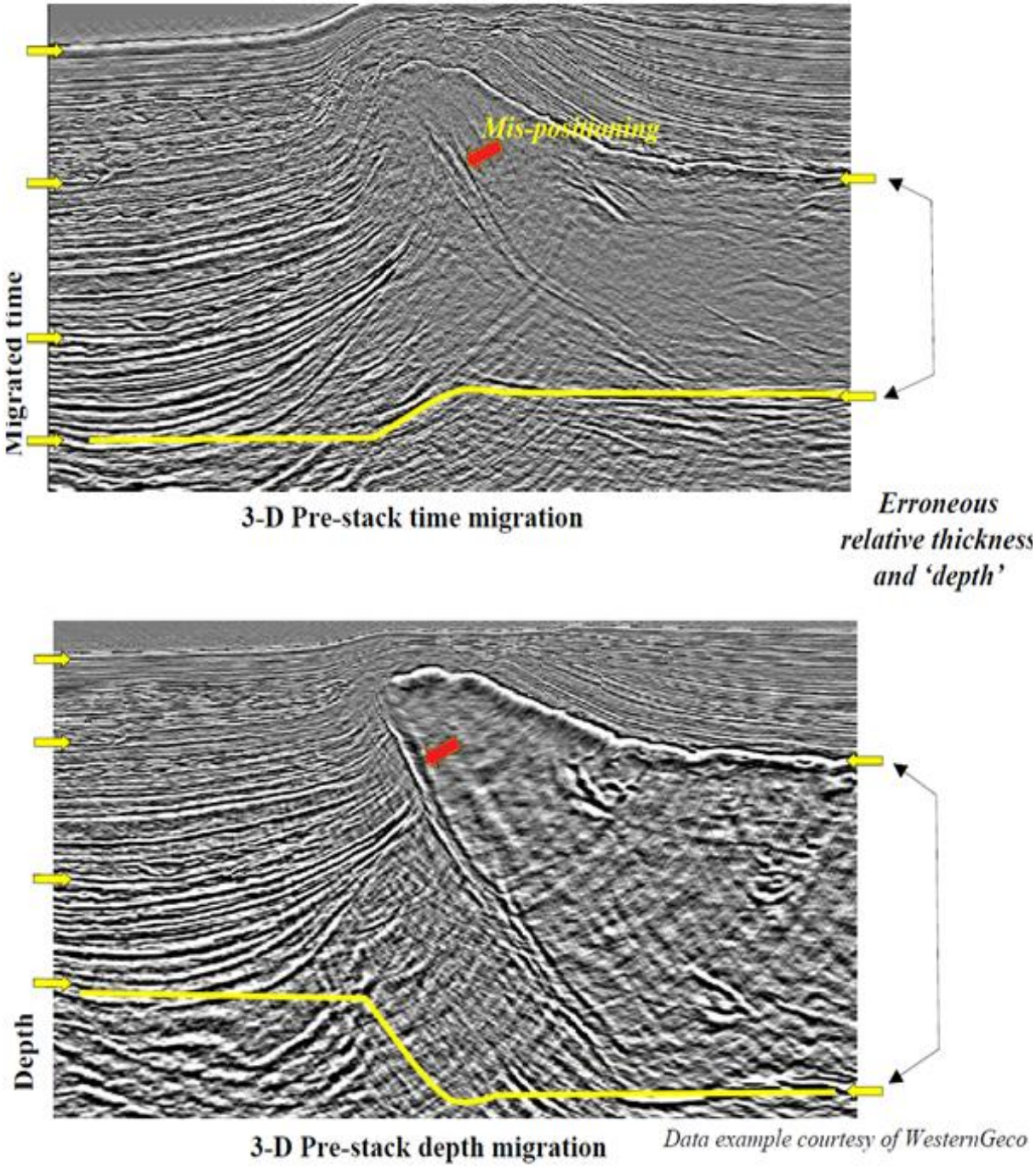

Figure 2.6: Comparison of time and depth migration images. The comparison reveals potential pitfalls associated with time migration (Robein, 2003).

2.3 2D versus 3D migration

In this section, the difference between 3D and 2D migration will be discussed, with the errors that occur if 2D migration is applied on a 3D data set. In *Figure 2.7* a dipping layer in a homogeneous medium is shown. Line *A* is in the dip – direction, while line *B* is in the strike direction.

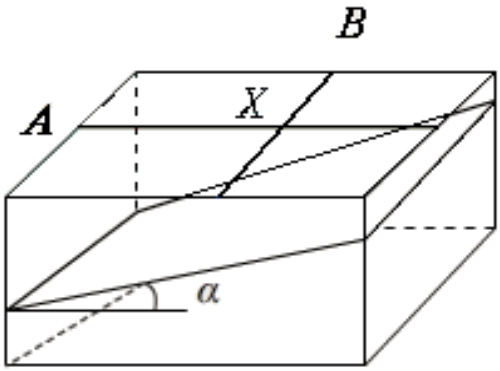

Figure 2.7: Homogeneous 3D volume with lines A and B in the dip- direction (Gelius and Johansen, 2010).

If 2D migration is performed on the 3D volume along lines *A* and *B*, the point *X* on the two lines in *Figure 2.7* will migrate to different subsurface positions, as shown in *Figure 2.8*.

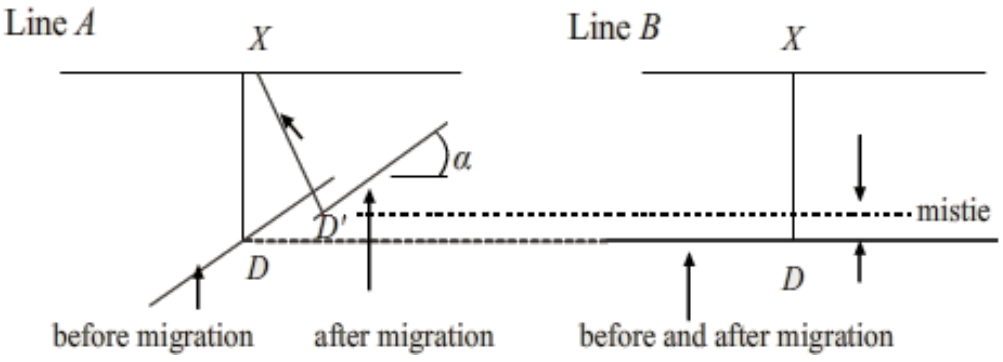

Figure 2.8: Illustrating processing error if 2D migration is applied on a 3D volume. Note how line B is unaffected by the migration (Gelius and Johansen, 2010).

Note that reflection in line *A* is shortened, steepened and has moved updip, while line *B* is unaffected by the migration process. To solve this problem, 3D migration must be applied on a 3D volume to correctly position the event along both directions.

If the subsurface structures are three dimensional in character, then 3D migration is also required. This phenomenon is demonstrated in *Figure 2.9. Figure 2.9a* is a stacked section of a salt dome, which has three dimensional characteristics. Below the results of 2D migration (*Figure 2.9b)* and 3D migration (*Figure 2.9c*) performed on the same section are shown. Here one can clearly see the difference in imaging of the top *T* of the salt, and the base *B* of the salt. It is evident that 2D migration is not able to handle the three dimensional structure, and this requires 3D migration.

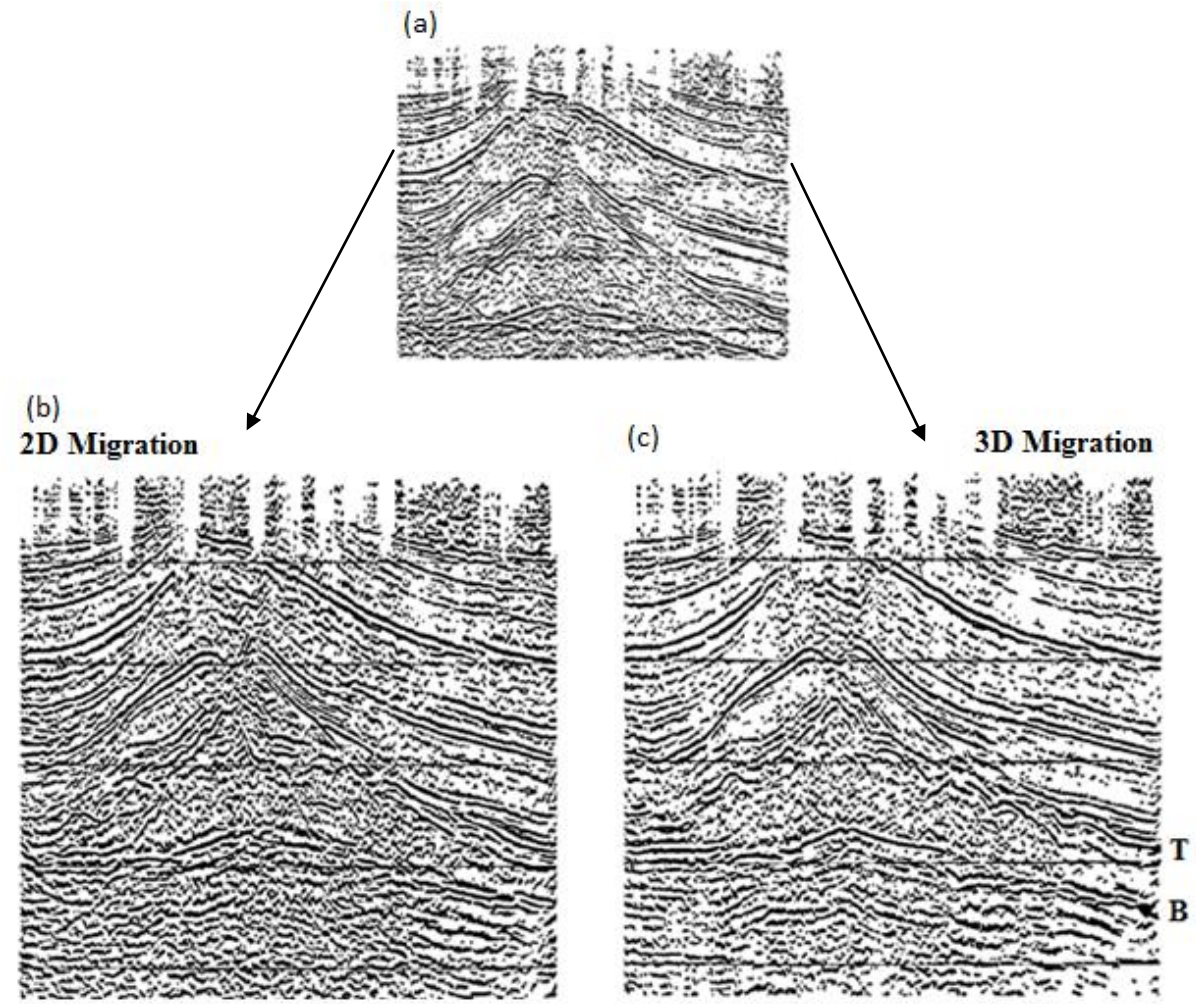

Figure 2.9: On top a stacked section of a three dimensional character (a) is shown. On the bottom a 2D migrated section (b) and 3D migrated section (c) of the top image are shown (Yilmaz, 2001-Modified).

In this work the focus is on 2D prestack Kirchhoff time migration. However, the obtained results can be extended and validated for 3D prestack Kirchhoff time migration.

3 Diffraction-time functions

The hyperbolic approximation used in *Chapter 2.1.1* is only accurate for a constant velocity medium with coinciding source and receivers, or when the aperture length is zero. Any deviation from these criteria requires other diffraction-time functions to approximate the travel times.

In this chapter a set of functions where the source and receivers are not coinciding, which is the case for pre stack time migration, will be derived. The philosophy of pre stack time migration method is similar to what we saw in *Chapter 2.1.1*, but now we operate with diffraction-time surfaces, and not diffraction-time curves. The diffraction-time functions define a diffraction-time surface in pre stack time migration.

The total travel time t can be obtained by adding the travel time from the source to the diffraction point t_s, to the travel time from the diffraction point to the receivers t_r (Bancroft et al, 1998). It is given by

$$t = t_s + t_r.$$

Eq. 3.1

For a constant velocity model, *Eq. 3.1* can be written as

$$t = \sqrt{\frac{z_0^2}{V^2} + \frac{d_s^2}{V^2}} + \sqrt{\frac{z_0^2}{V^2} + \frac{d_r^2}{V^2}}.$$

Eq. 3.2

Here, z_0 is the depth to the image point, V is the constant velocity, and d_s and d_r are given by

$$d_s = s - m,$$

Eq. 3.3

$$d_r = r - m,$$

Eq. 3.3

where *s*, *r* and *m* denote, respectively, the lateral coordinates of the source point, *S*, the receiver point, *R*, and the diffraction apex location, *M* (see *Figure 3.1)*. Note that the point *M* is located directly above the diffraction point.

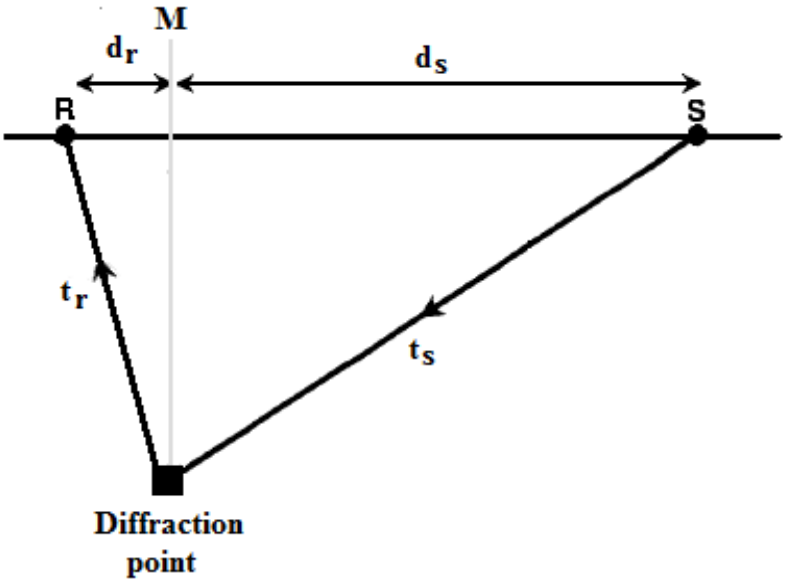

Figure 3.1: Geometry of Kirchhoff prestack time migration. The total travel time from the source S to the receiver R is the sum of t_s and t_r. M represents the diffraction location

In the case of vertical velocity variation only, one can observe that the first terms under the square roots in *Eq. 3.2* is $\frac{t^0}{2}$.

The modified formula will be referred to as the conventional double square root (DSR) diffraction-time function in this work (Fowler, 1997; Bancroft et al, 1998; Hellman, 2007). The function is known to adequately handle vertical velocity variation and weak lateral velocity variation. It is given by

$$t_{input} = \sqrt{\frac{(t^0)^2}{4} + \frac{d_s^2}{V_{mig}^2}} + \sqrt{\frac{(t^0)^2}{4} + \frac{d_r^2}{V_{mig}^2}},$$

Eq. 3.4

where V_{mig} is the RMS velocity of Taner and Koehler (1969), evaluated at t_0 (Bancroft et al, 1998).

The velocity *V* is then replaced by the root mean square velocity V_{mig}, which is referred to as migration velocity.

New and more advanced approaches to the DSR function have been developed by introducing additional terms. The aim is to achieve better approximations in areas with complex geology. The new terms provide additional degrees of freedom to the DSR function, enabling one to achieve better approximations of the diffraction-time surfaces. Hellman (2006) introduced a new diffraction-time function including terms of 4th and 6th order. In this work, the function is referred to as the Hellman diffraction-time function, given by

$$t_{input} = \sqrt{\frac{(t^0)^2}{4} + \frac{d_s^2}{V_{mig}^2} + c_4 d_s^4 + c_6 d_s^6} + \sqrt{\frac{(t^0)^2}{4} + \frac{d_r^2}{V_{mig}^2} + c_4 d_r^4 + c_6 d_r^6},$$

Eq. 3.5

where c_4 and c_6 are constants.

In the introduction chapter it was briefly mentioned that functions with 3rd and 5th order terms have been granted very little, or no attention. One of the main tasks in this work is to quantify how the various diffraction -time functions can handle velocity variations, and to study how 3rd and 5th order terms improve the results when operating with asymmetric diffraction-time surfaces. The additional diffraction-time functions tested in this work are shown below.

$$t_{input} = \sqrt{\frac{(t^0)^2}{4} + \frac{d_s^2}{V_{mig}^2} + c_3 d_s^3} + \sqrt{\frac{(t^0)^2}{4} + \frac{d_r^2}{V_{mig}^2} + c_3 d_r^3},$$

Eq. 3.6

$$t_{input} = \sqrt{\frac{(t^0)^2}{4} + \frac{d_s^2}{V_{mig}^2} + c_3 d_s^3 + c_4 d_s^4} + \sqrt{\frac{(t^0)^2}{4} + \frac{d_r^2}{V_{mig}^2} + c_3 d_r^3 + c_4 d_r^4},$$

Eq. 3.7

$$t_{input} = \sqrt{\frac{(t^0)^2}{4} + \frac{d_s^2}{V_{mig}^2} + c_3 d_s^3 + c_4 d_s^4 + c_5 d_s^5} + \sqrt{\frac{(t^0)^2}{4} + \frac{d_r^2}{V_{mig}^2} + c_3 d_r^3 + c_4 d_r^4 + c_5 d_r^5},$$

Eq. 3.8

Diffraction-time functions

$$t_{input}\sqrt{\frac{(t^0)^2}{4}+\frac{d_s^2}{V_{mig}^2}+c_3d_s^3+c_4d_s^4+c_5d_s^5+c_6d_s^6}+\sqrt{\frac{(t^0)^2}{4}+\frac{d_r^2}{V_{mig}^2}+c_3d_r^3\ +c_4d_r^4+c_5d_r^5+c_6d_r^6}.$$

Eq. 3.9

For practical reasons, the term with the highest order in each equation was used to classify the function. Thus, *Eq. 3.6* is called High 3, *Eq. 3.7* is called High 4 and so on. The equations *Eq. 3.4* to *Eq. 3.9* define the diffraction-time surface over which the Kirchhoff summation process takes place. As mentioned, the new terms provide additional degrees of freedom compared to the conventional DSR function. Thus, a better approximation of the travel time in the Green's function is believed to be achieved, which again is expected to yield a better time image after the summation process has been carried out. Note that each of the equations *Eq. 3.4* to *Eq. 3.9* approximate the diffraction-time surface differently.

In this work, the coefficients involved in each diffraction-time function were determined by performing a least square surface fitting to the synthetic data. In reality this approach is not possible to use for real data. The coefficients are determined through a velocity analysis. To understand how the coefficients are determined, it is of interest to understand how the best image is obtained. The best image is obtained when each event is migrated back to the same time for all offsets. Thus, the goal of prestack time migration velocity analysis is to find a velocity function which enables one to move the recorded event back to the same time for all offsets.

One of the common techniques used to perform the analysis is called the scanning technique. For the conventional DSR function, several V_{mig} are scanned for each t_0. The resulting semblance value for each V_{mig} at t_0 is determined, and the one that gives the highest semblance is kept. Further, the best result is judged by objective criteria. It is common to add or remove 5-10 % to the initial velocity field (Robein, 2003). Note that this velocity analysis is never performed on the migrated section. For more complex diffraction-time functions with additional terms, the scanning technique becomes cumbersome. It is therefore desirable to use another approach to determine the coefficients. Fomel and Stovas (2010) used one normal incident-ray and one ray at a large offset for this purpose. When these coefficients are

determined through the velocity analysis, they are used as input for the time migration functions. During the migration process the coefficients are not approximated.

4 Implementation

4.1 Model building with NORSAR- 3D

Seismic reflection profiling aims to achieve a cross-sectional image of the layered portions of the earth's crust. The grade of success depends on how well a geologist with little or no understanding of the applied imaging method is able to use his knowledge and experience to solve problems. For simple structures the interpreter can consider the cross section as a photographic image to solve the problems. When complex structures are imaged, seismic reflection profiling produces cross sections which deviate from a photographic image. Thus, there is a need for an analysis which derives cross sections without relaying on the seismic section as a photographic image. Seismic modeling satisfies this need (Fagin, 1991).

When the model is built one has to determine the size of the model, number of surfaces and their orientation, the direction of velocity variation, if the model should be a 2D or 3D model, the level of structural detail required to solve the problem and also how to obtain information about the velocity.

When considering these issues one should be aware of the advantages and disadvantages of each element, and how they affect the main goal. For example a 3D model requires more time to create and more computing resources. On the other hand it can simulate sideswipes and enables one to model series of in-lines or cross-lines in one single model. The size of the model should also be taken into consideration. It is important that the model is wide enough to capture rays from any feature under investigation. Building a model which extends outside the seismic control may also be of interest of the modeler to investigate if reflections have not been recorded because of the length limitation of the receiver array (Fagin, 1991).

The modeler also has to decide how to obtain information about the velocity. The interval velocities can be determined by well logs, laboratory measurements on core samples or seismic data. In *Table 4.1 t*he frequency and scale vary between the methods. The obtained velocity from the different methods can vary significantly. Therefore, care should be taken when applying them in the model. Regardless of the chosen method, the velocities should

represent the travel time through the model correctly (Fagin, 1991; Gelius and Johansen, 2010).

	Laboratory Measurement	Well-Logs	Seismic Data
Frequency	Decreasing →		
Scale	Increasing →		

Table 4.1: Shows how frequency, scale and resolution vary for laboratory measurements, well-logs and seismic data.

In this work, NORSAR-3D software was used to build geomodels. The software uses ray tracing to generate travel times. In order to apply ray tracing in heterogeneous media, a high frequency approximation is required. This means that the wavelength λ of the seismic signal must be smaller than the heterogeneities in the media in order for ray tracing to function correctly. Here, we consider a geomodel to contain information about layer orientation, diffraction point location, receiver position, density distribution with a incorporated velocity field.

In *Figure 4.1* the main steps in the building process are shown. First the size of the geomodel was specified. For convenience all the models tested were 20 km by 20 km by 10 km. Then numbers of layers, layer orientation and velocity field were specified in the model builder. An example of the model builder is shown on the top image in *Figure 4.1*. Further, the location, length, and spacing of the receiver was specified in the receiver and shot survey. Here, every diffraction point is located at the center of the model, at a depth of 6 km. The length of the receiver array is 18 km and the spacing is 100 m. A typical receiver array length used to acquire seismic data is around 10 km. It is desirable to use a larger receiver array in this work when the diffraction-time surface is transformed from the shot-receiver domain to the aperture-half offset domain.

The anisotropy parameters ε and δ was specified in the model builder, when geomodels with anisotropy were created.

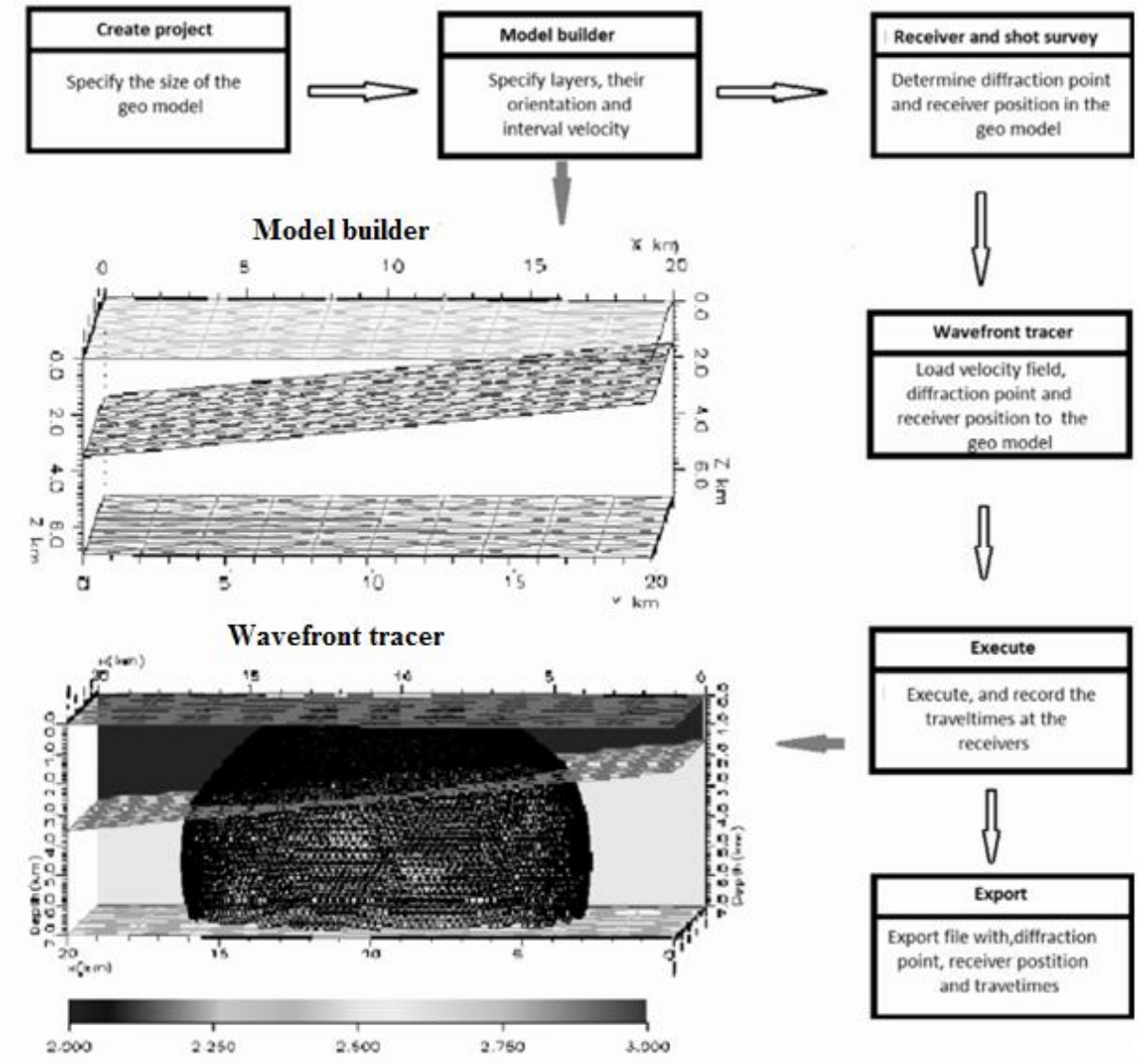

Figure 4.1: Illustration and description of the main steps involved in model building. For anisotropic models ε, δ and axis of symetry was spesified in the Model builder. On the bottom left, one can see how the wavefront propagates through the model.

Further, the location of the diffraction point as well as the location, length, and spacing of the receiver was specified in the receiver and shot survey. Finally, the geomodel and survey were loaded and executed in the wavefront tracer. On the bottom image in *Figure 4.1* one can see how the wavefront propagates through a model in the wave front tracer, and gets recorded at the surface. The one way travel time and receiver positions were extracted and exported as an *ascii file. The extracted one way travel times were later used to generate two-way travel times.

4.1.1 Velocity models

A constant velocity field was used to confirm that the different diffraction-time functions were functioning correctly. Constant vertical and lateral velocity gradients were also tested. As previously mentioned, time migration is only applicable when no, or small lateral velocity variation are present. Thus, lateral velocity variations are expected to affect the approximation results more than the vertical velocity variations. Velocity fields were obtained by

$$V(x, y, z) = V_0 + V_x(x - x_0) + V_z(z - z_0),$$

Eq. 4.1

where V_0 is the reference velocity, V_x is given in velocity per unit distance in the lateral direction, V_z is given in velocity per unit distance in the vertical direction. x_0 is the reference location along the x axis, and z_0 is the reference location along the z axis.

An additional term was added to the velocity model to create a periodic variation in the velocity field. This enabled one to generate more complex velocity models. *Eq. 4.2* is capable of generating velocity models which enables one to study how well different diffraction-time functions can handle complex velocity variations, and is given by

$$V(x, y, z) = V_0 + V_x(x - x_0) + V_z(z - z_0) + B\cos[\frac{(x-x_0)}{L}2\pi],$$

Eq. 4.2

where B is the velocity amplitude and L determines the period of the cosine function.

Tables 4.2 to *4.6* show the typical densities and P-wave velocities for chalks, tight-gas sandstones, high-porosity sandstones, limestones and dolomites, in respective order (Mavko et al, 2009). The majority of the models were created within the velocity limits mentioned in the tables. However, some of the tested velocity models also deviated from the above mentioned velocities. The two extremities used in this work are 1.50 km/s and 7.90 km/s. The maximum velocity is very high compared to what is common in nature. Some models are also more complicated than what is common. By pushing the limits it becomes easier to quantify which of the diffraction-time functions is capable of handling the velocity variations.

Chalks			
ρ (g/cm^3)		Vp (km/s)	
Min	Max	Min	Max
1.43	2.57	1.53	4.30

Table 4.2: Typical density and velocity range for chalks.

Tight–gas sandstones			
ρ (g/cm^3)		Vp (km/s)	
Min	Max	Min	Max
2.26	2.67	3.81	5.57

Table 4.3: Typical density and velocity range for tight-gas sandstones.

High-porosity sandstones			
ρ (g/cm^3)		Vp (km/s)	
Min	Max	Min	Max
2.12	2.69	3.46	4.79

Table 4.4: Typical density and velocity range for high-porosity sandstones.

Limestones			
ρ (g/cm^3)		Vp (km/s)	
Min	Max	Min	Max
2.00	2.56	3.39	5.79

Table 4.5: Typical density and velocity range for Limestones.

Dolomites			
ρ (g/cm^3)		Vp (km/s)	
Min	Max	Min	Max
2.27	2.84	3.41	7.02

Table 4.6: Typical density and velocity range for Dolomites

Rock densities also affect the velocity. The density was kept constant and equal to 2.4 g/cm^3 in each model throughout this work. The chosen density value is reasonable as it is within the range of the densities of the four rock types shown in y are compared against *Tables 4.2* to *4.*6. The subsurface is far from a constant density medium, but the effect of the density

variations are considered as too small to influence the final conclusions in this work, and thereby justifies the use of constant density.

4.2 MATLAB programs and Root mean square error

Root mean square (RMS) error is commonly used to measure the error when theoretical data is compared with actual measurements (Taylor, 1982). In this work the RMS value is used to quantify the error in seconds (s). Thus, one can compare the different diffraction-time function used. This will eventually allow us to determine the function that works best for the tested scenarios.

A set of parameters must be defined to arrive on the RMS formula. For this work the actual data X_{best} is the extracted data from NORSAR-3D. On the other hand, the actual measurements X_i, are calculated by the diffraction-time functions. The residual D_i will then be the difference between X_i and X_{best}. D_i is given by

$$D_i = X_i - X_{best},$$

Eq. 4.3

where X_i and X_{best} are measured in seconds in this work.

A small D_i represents a small residual. This means that there is a good match between the calculated result, and the measured data. On the other hand, a large residual represents a mismatch between the calculated and measured data. A challenge with this definition is that the residuals can sometimes be positive or negative in a way that the sum of the residuals becomes zero. To avoid this problem the sum of the squared residuals is used. Thus, all values become positive. By averaging them and taking the square root one eventually arrives with the formula for the RMS error, which is given by

$$RMS = \sqrt{\frac{1}{N}\sum_{i=1}^{N}(D_i)^2},$$

Eq. 4.4

where N is the number of measurements, and D_i is given in seconds. Thus, the RMS error is also in seconds.

MATLAB was used to compare the data generated from NORSAR-3D with the diffraction-time functions. The aim is to determine the values of the coefficients in each function which gives the smallest RMS error.

4.2.1 Scanning technique

The scanning technique requires the user to specify the range and interval of V_{mig}, t_0 and the belonging coefficients in *Eq. 3.4* to *Eq. 3.9*. Thus, a parameter space was created and the RMS error was calculated for every possible combination of values within the parameter space. In *Figure 4.2* a schematic illustration including the main steps involved in the scanning technique are shown.

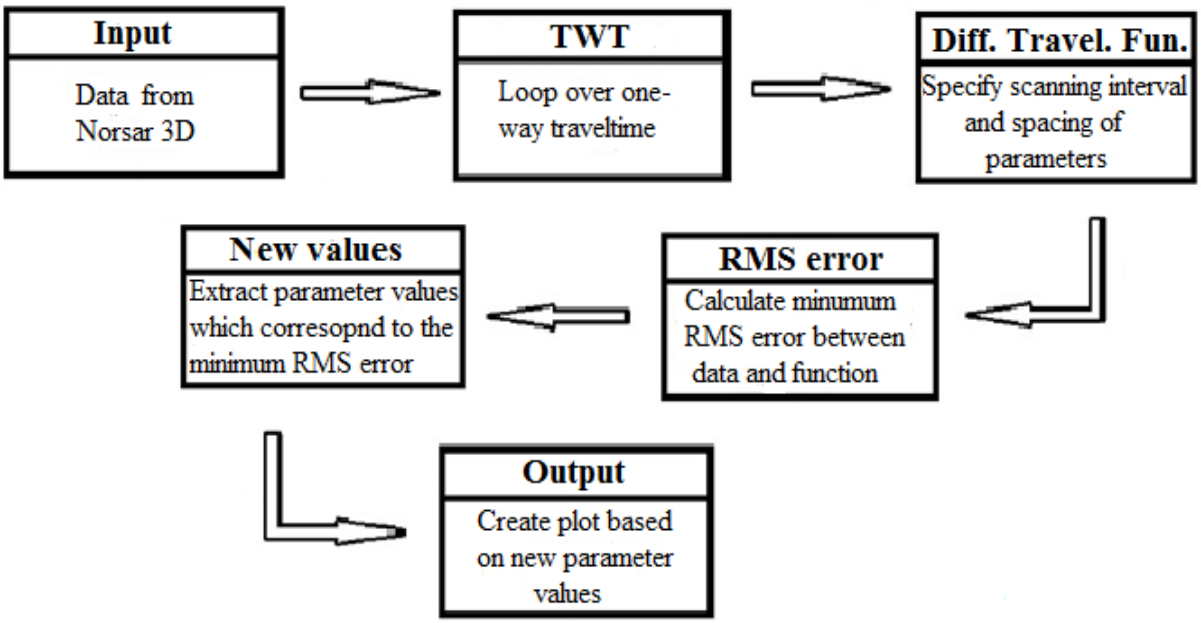

Figure 4.2: Main steps involved using the scanning technique. A parameter space is created, and RMS errors were calculated for every possible combination within the parameter space.

After scanning through the parameter space and determining the values which gave the smallest RMS error, diffraction-time surface plots were created based on these new values. However, specifying the interval and spacing proved to be a challenging task when the number of terms increased to more than three, because the method proved to be time consuming. Depending on the diffraction-time function, testing took between one to two days to achieve an acceptable result for one single geomodel. The MATLAB code for this approach is found in *Appendix 1*. A new approach was needed to be able to test efficiently.

4.2.2 Non linear least square surface fitting

An optimizer called non linear least square fitting in MATLAB was used to determine the coefficients in each diffraction-function which gave the smallest RMS error, in addition to the RMS error itself. The optimizer is capable of solving least square problems, and also capable of performing least square non linear surface fitting. In *Figure 4.3* the main steps involved in the approach are shown. The two first steps are similar to the scanning technique. In the third step, the function to be minimized is defined. In this work the input data are the travel times provided by NORSAR-3D and the diffraction-time function. The aim is to find the values of the coefficients in the diffraction-time functions which minimize the RMS error as mentioned earlier. The function is stored as an *m-file. Later, the optimization is performed by selecting a starting point, and invoking the optimizer. The optimizer finds the minimum of the sum of squares of the defined function. Finally, the results are normalized to find the RMS error in seconds, and the parameter values of the diffraction-time function are determined. The plots presented in *Chapter 4* and *5* are based on these values. An example involving the High 3 function is shown in *Appendix 2*. The example contains the actual MATLAB code for the High 3function used in this work.

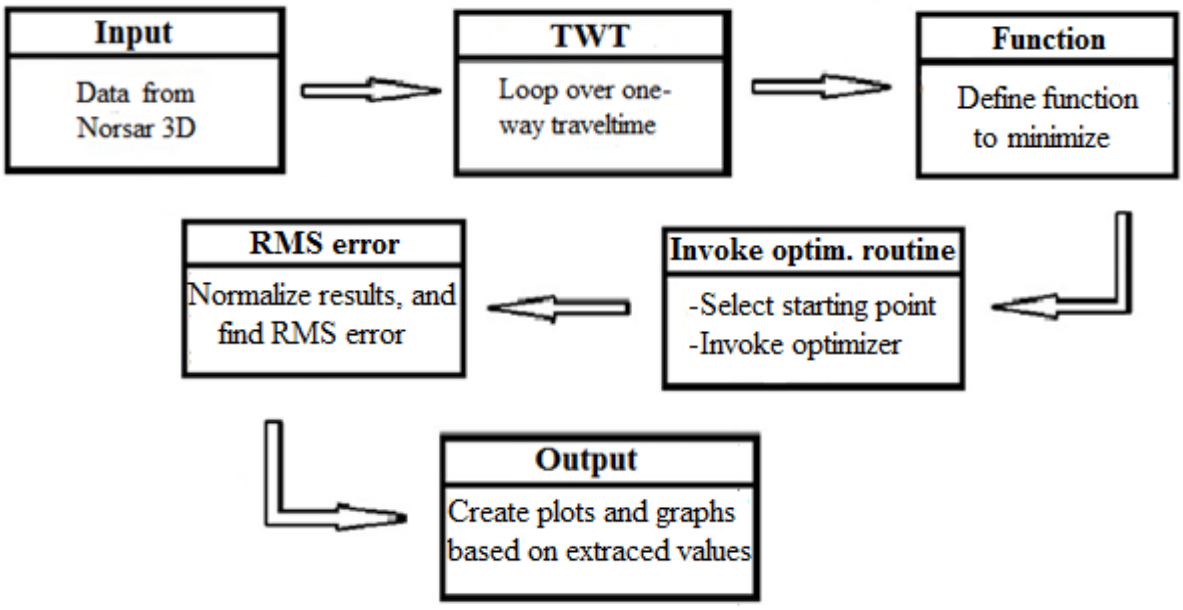

Figure 4.3: Main steps involved using the non linear least square fitting technique.

5 Isotropic media

In the following chapter, results performed on isotropic media are presented and discussed. The results are also shown in table form in *Appendix 3*. An isotropic medium represents the highest degree of symmetry of an elastic solid, and properties are not directionally dependent (Stein and Wysession, 2003). For an isotropic medium two independent elastic constants are enough to represent the medium. The independent elastic constants are given by the two Lamè parameters λ and μ. μ is also called the shear modulus. The Voigt representation of the elastic constant matrix C for an isotropic medium can be written as

$$C_{\alpha\beta} = \begin{Bmatrix} \lambda+2\mu & \lambda & \lambda & & & \\ \lambda & \lambda+2\mu & \lambda & & & \\ \lambda & \lambda & \lambda+2\mu & & & \\ & & & \mu & & \\ & & & & \mu & \\ & & & & & \mu \end{Bmatrix}.$$

Eq. 5.1

5.1 Results

The characteristics of the tested models are shown in *Figure 5.1*. The models are grouped in series depending on the direction of the velocity variation. In D-series the constant vertical velocity gradient (dV/dz) was increased gradually in each geomodel created in NORSAR-3D. In A15-series the horizontal velocity gradient (dV/dx) and vertical velocity gradient (dV/dz) were changed to create a velocity gradient with a direction of 15 degrees with respect to the vertical, while the other properties were kept constant. Accordingly, in A30-series dV/dx and dV/dz were changed to create a velocity gradient with a direction of 30 degrees with respect to the vertical, and so on. Note that D-series and G-series represent the two extremities in the table. D-series has only vertical velocity variation, while G-series is entirely dominated by lateral velocity variation. The only vertical velocity variation in G-series is caused by the period L and velocity amplitude B in *Eq. 4.2*. Between the two extremities, test series have been performed as shown in *Figure 5.1*.

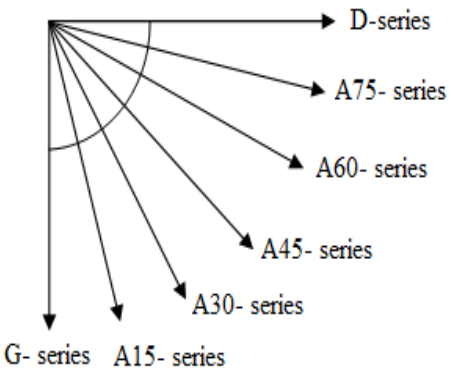

Figure 5.1: Showing velocity gradient direction for each test series. For example A15 has a velocity gradient direction of 15 with respect to the vertical.

In *Table 5.1* the minimum and maximum values of the varying property in each series is showed in the gray area. Unchanged properties are shown with numbers in the table.

	X_0 (km)	V_0 (km/s)	dV/dz (s^{-1})	dV/dx (s^{-1})	B (km/s)	L (km)
D- series	0.0	2.0	0.0000-0.5000	0.0	0.0	0.0
A15- series	0.0	2.0	0.0342-0.3073	0.0091-0.0824	0.0	0.0
A30- series	0.0	2.0	0.0306-0.2756	0.0177-0.1591	0.0	0.0
A45- series	0.0	2.0	0.0250-0.2250	0.0250-0.2250	0.0	0.0
A60- series	0.0	2.0	0.0177-0.1590	0.0306-0.2756	0.0	0.0
A75- series	0.0	2.0	0.0092-0.0824	0.0341-0.3073	0.0	0.0
G- series	0.0	5.6	0.0	0.0000-0. 2500	0.3	5.0

Table 5.1: Constant property displayed with values, and minimum and maximum values of the varying properties are highlighted in the gray boxes for each test series. X_0 and V_0 *is the reference point and reference velocity in the velocity model. B and L are the velocity amplitude and period from Eq. 4.2.*

Further, two test series were tested where only the period *L* in *Eq. 4.2* was changed, as shown in *Table 5.2.* Geomodels in P1-series were symmetric because the reference point X_0 of the incorporated velocity field was placed at the center geomodels. Thus, the diffraction-time surfaces were also symmetric. In order to study how asymmetry affected the results, P2-series was also created.

	X_0 (km)	V_0 (km/s)	dV/dz (s^{-1})	dV/dx (s^{-1})	B (km/s)	L (km)
P1- series	10	2	0	0	0.1	1.5-7.0
P2- series	7	2	0	0	0.1	1.5-7.0

Table 5.2: Input values used in Eq. 4.2 for P1-series and P2-series.

The last isotropic series tested in this work was the K-series. Here the period *L* in *Eq. 4.2* was changed to create geomodels with gradually increasing level of complexity as shown in *Table 5.3*. Even though the period is changed the same way as in the tested P1 and P2-series, there are important differences. The average velocities used in these models are higher. The amplitude *B* is also larger. Thus, the velocity gradients are larger and steeper in this series. The level of complexity resulted in caustics for models K5 and K6, as the rays were severely bent. The complexity level of the geomodels is pushed to the extreme to study how the modified diffraction -time functions were able to cope. Even though the subsurface velocities do not change in the same manner in nature, caustics occur when data are acquired, and is therefore of interest.

	X_0 (km)	V_0 (km/s)	dV/dz (s^{-1})	dV/dx (s^{-1})	B (km/s)	L (km)
K1	3.0	4.0	0.1	0.1	0.5	4.0
K2	3.0	4.0	0.1	0.1	0.5	3.5
K3	3.0	4.0	0.1	0.1	0.5	3.0
K4	3.0	4.0	0.1	0.1	0.5	2.5
K5	3.0	4.0	0.1	0.1	0.5	2.0
K6	3.0	4.0	0.1	0.1	0.5	1.5

Table 5.3: Input values for each model in K-series.

In *Figure 5.2* the first model in A45-series is shown. It illustrates the acquisition geometry used for every geomodel in this work. In the figure one can see the velocity field in colors as also shown in the colorbar legend. Here the velocity gradient is 0.035 s^{-1}, and 45 degrees with respect to the vertical. In the background the diffraction point located at 6 km depth is shown, and the receiver array stretching from 1 km to 19 km in the model is also visible. The spacing between each receiver is 100 m. One can also see the ray path from the diffraction point to the receivers, illustrated by the black lines on the figure.

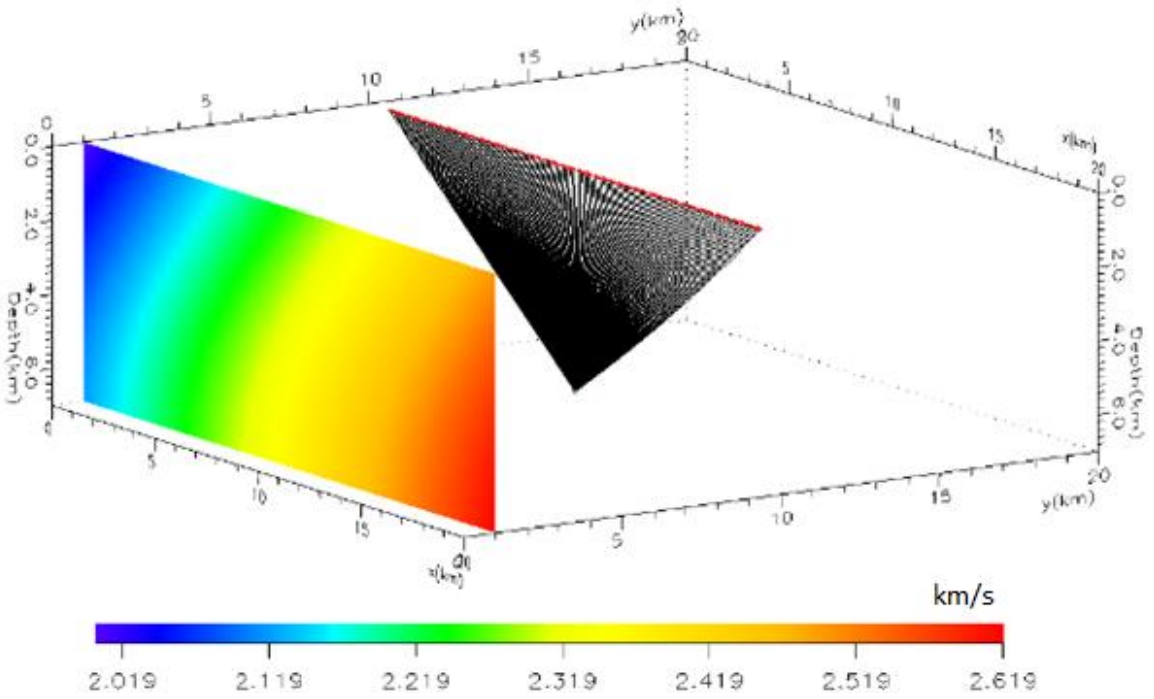

Figure 5.2: Showing acquisition geometry for the first model in A45-series. The velocity field, diffraction point location, ray path and receiver location are shown on the image. Similar acquisition geometry was used for every model in this work.

The results obtained for the isotropic models are displayed and discussed as follows:

5.1.1 Vertical velocity variation (D-series)

Ten geomodels were created and tested with gradually increasing vertical velocity gradient dV/dz from 0.0 s^{-1} to 0.5 s^{-1}. *Eq. 4.1* was used to create the velocity model. The aim was to verify the test procedure, and also to confirm that prestack time migration is efficient in media with little or no lateral velocity variation. In *Figure 5.3* the RMS errors increase with increasing vertical velocity gradient. Each color in the plots corresponds to a diffraction-time function. For example the High 5 function (green) represents the results obtained by *Eq. 3.8*, and the Hellman function (red) represents the results obtained by *Eq. 3.5*, and so on.

The black arrow on the bottom left shows how well the diffraction-time functions are handling a constant velocity medium. For a constant velocity medium all the functions are expected to be able to approximate diffraction-time surface perfectly. RMS error values equal to zero indicates a perfect approximation.

Figure 5.4 and *Figure 5.5* show velocities and two-way travel times, respectively, determined by the diffraction-time functions for D-series.

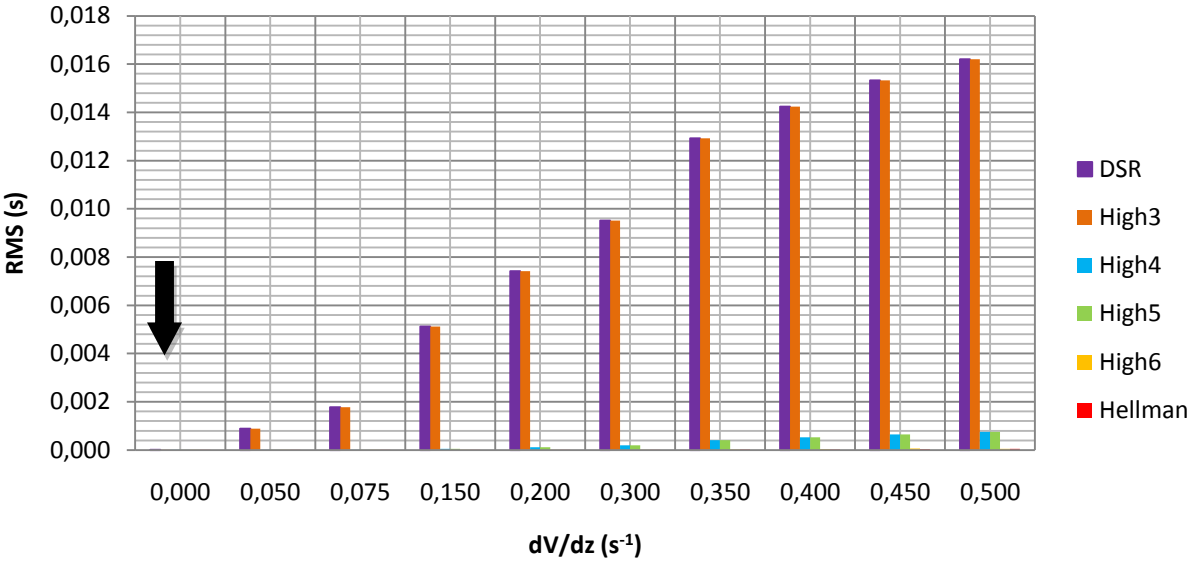

Figure 5.3: RMS error for a constant medium model shown by the black arrow, and geomodels with vertically varying velocity field.

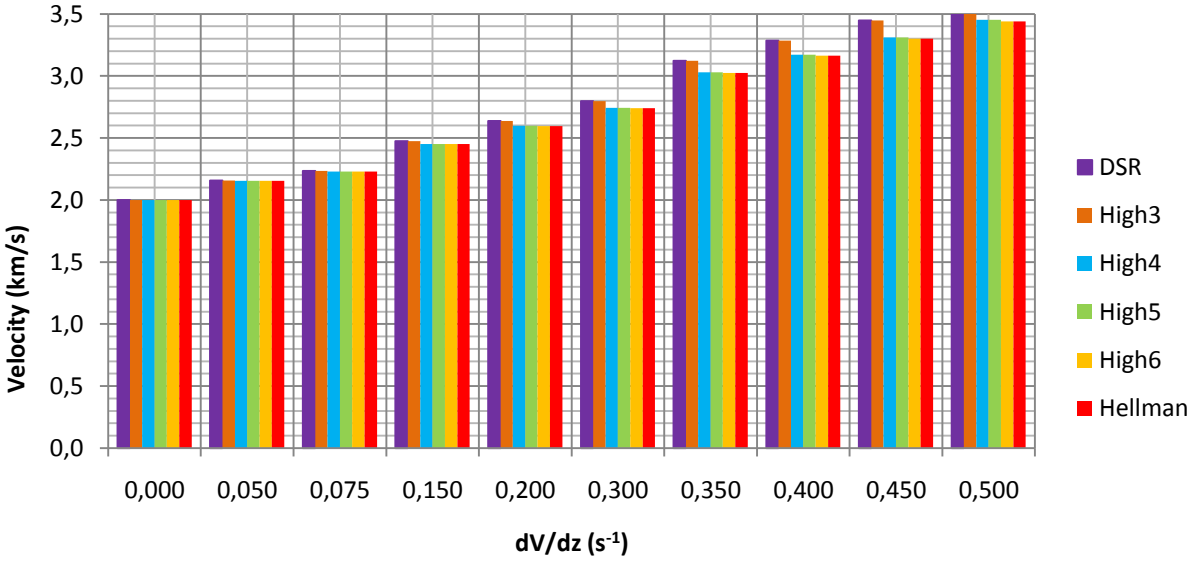

Figure 5.4: Velocities determined by diffraction-time functions for D-series.

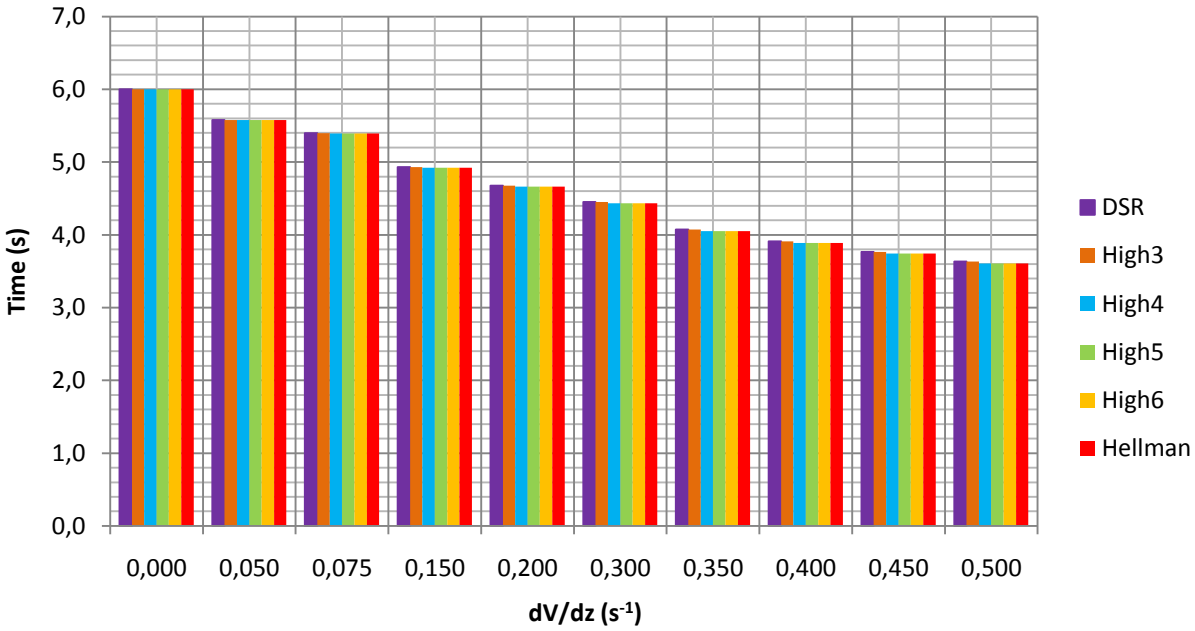

Figure 5.5: TWT determined by diffraction-time functions for D-series.

The reference velocity V_0 is equal to the medium velocity for the homogenous isotropic model. Comparing results from the diffraction-time functions, with the reference velocity V_0 for the homogeneous isotropic model, show perfect match equal to 2 km/s. In this case the two-way travel time is expected to be 6 s, which is also verified by *Figure 5.5*. The result for the constant velocity medium verifies that the test procedure functions correctly. The other velocities are also as expected, and are close to the average velocity in the neighborhood of the diffraction point.

In D-series the RMS error increases for each function when the vertical velocity gradient increases. There is a clear tendency that the DSR and High 3 functions obtain the largest errors. However, the overall magnitude of the RMS errors for all the tested functions are low. The largest RMS errors, obtained with the DSR and High 3 functions, are approximately 16 ms when dV/dz = 0.5 s^{-1}. When the diffraction point is back propagated to the reflector, an error of 16 ms is negligible. To get an idea of the error one can compare it with the period of the seismic signal. As mentioned the seismic signal is band limited. A typical frequency range for the seismic signal is between 30 Hz to 80 Hz. The corresponding period of the seismic signal is between 0.033 s and 0.013 s. It may be noted that high frequencies get attenuated at shallow depth. Thus, only the lower frequencies are recorded from great depths. When the RMS error of 0.016 s is compared to the low frequency, one can see that the period of 0.033 is

larger. RMS errors below below the period of the seismic signal are considered as good approximations and will provide good images after the migration process. This confirms that the DSR function is well applicable when only vertical velocity variations are present.

It is also clear that the High 3 function give the same results as the DSR function. Even though the overall RMS errors are small, it shows that the additional odd term in High 3 has no effect. This is because of the symmetric character of the diffraction-time surfaces in this series. The observation is also verified when High 4 and High 5 are compared. It is evident that both functions give the same results, and that the additional odd term of 5^{th} order in High 5 does not provide a better approximation of the diffraction-time surfaces. In *Appendix 3.1* the constants c_3 and c_5 in the two functions are zero, which reduces them in practice. The observations are also consistent with the observations made for the Hellman function. Hellman has two additional even terms of 4^{th} and 6^{th} order. The even terms reduces the RMS error to approximately zero seconds throughout the series, and proves to be efficient in cases with only vertical velocity variations.

In *Figure 5.6* a diffraction-time surface for a vertically varying velocity field is shown by the ceops pyramid. The image is showing a geomodel where $dV/dz = 0.075\ s^{-1}$in D-series. These results indicate that functions with higher-order even terms are likely to improve the approximation for simple symmetric diffraction-time surfaces. However, a symmetric diffraction- time surface is not a guarantee for a good approximation, and as we will see later it depends on the character of the time surface. In D-series we have seen how the conventional DSR function obtains acceptable results, and the efficiency of the additional even terms introduced in the functions for vertically varying velocity fields.

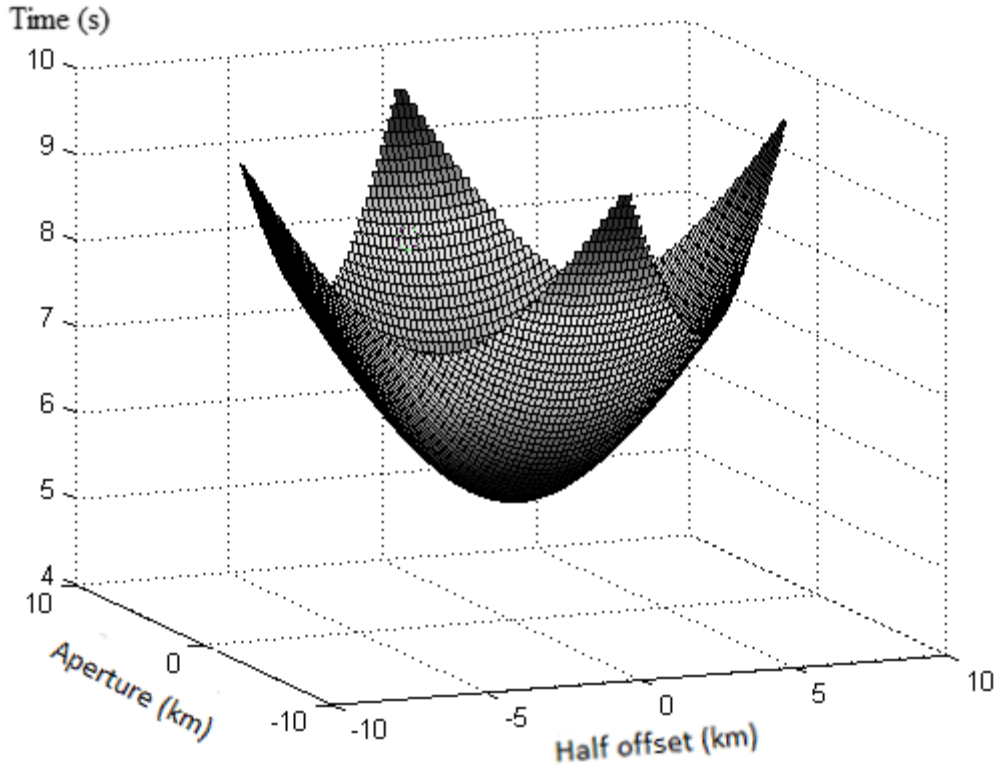

Figure 5.6: Diffraction-time surface for a vertically varying velocity field. Image is showing geomodel with dV/dz = 0.075 s^{-1} in D-series.

5.1.2 Tilted velocity gradient (A-series)

In all the A-series the velocity gradient is tilted with respect to the vertical. Here, lateral velocity gradient increases from one series to the other because the velocity gradient changes direction. In order to introduce gradually some form for lateral variation, the velocity gradient was tilted with an interval of 15 degrees with respect to the vertical for different series. In other words, the lateral velocity contribution was gradually increased. The magnitudes of the velocity gradients were similar in each series. The RMS errors for A15-series, A30-series, A45-series, A60-series and A75-series are shown in *Figures 5.7* to *5.11*, respectively. The plots are displayed with the same vertical scale for easier visual comparison.

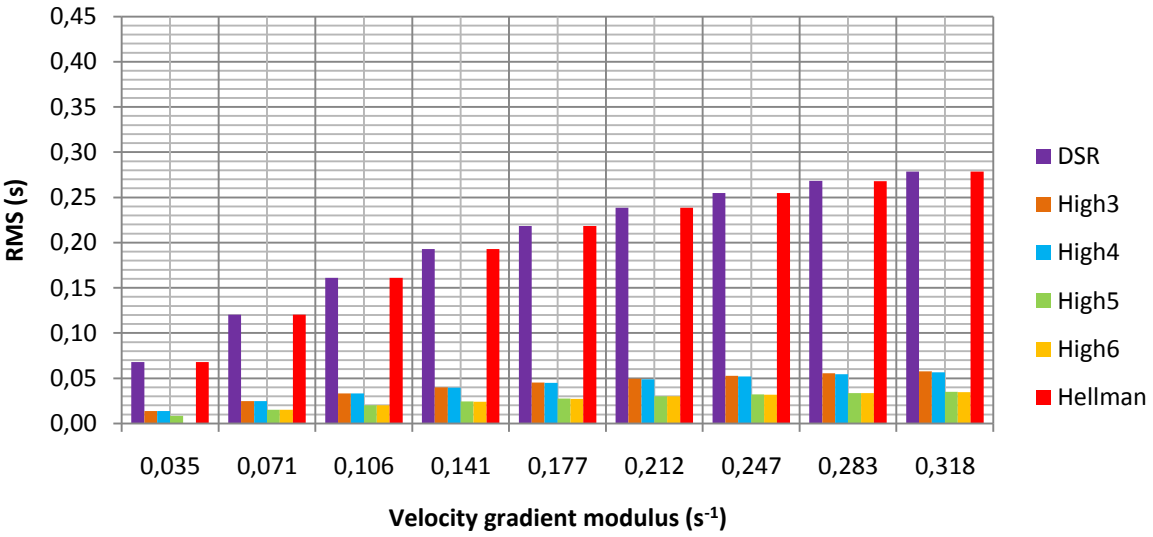

Figure 5.7: RMS errors for A15-seies. Velocity gradient modulus is 15 degrees with respect to the vertical, and gradually increased.

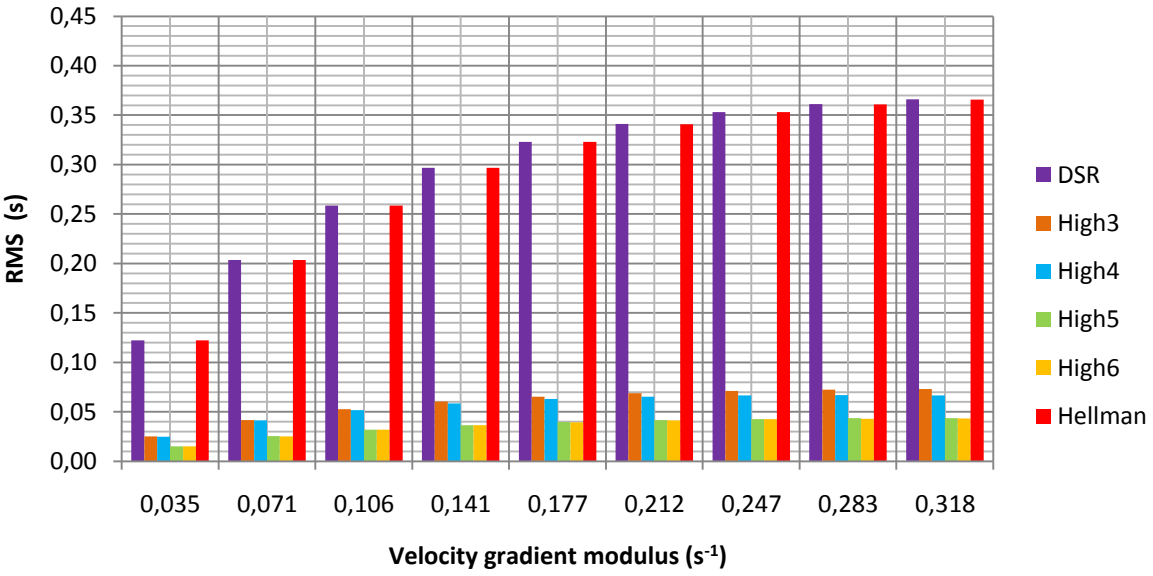

Figure 5.8: RMS errors for A30-seies. Velocity gradient modulus is 30 degrees with respect to the vertical, and gradually increased.

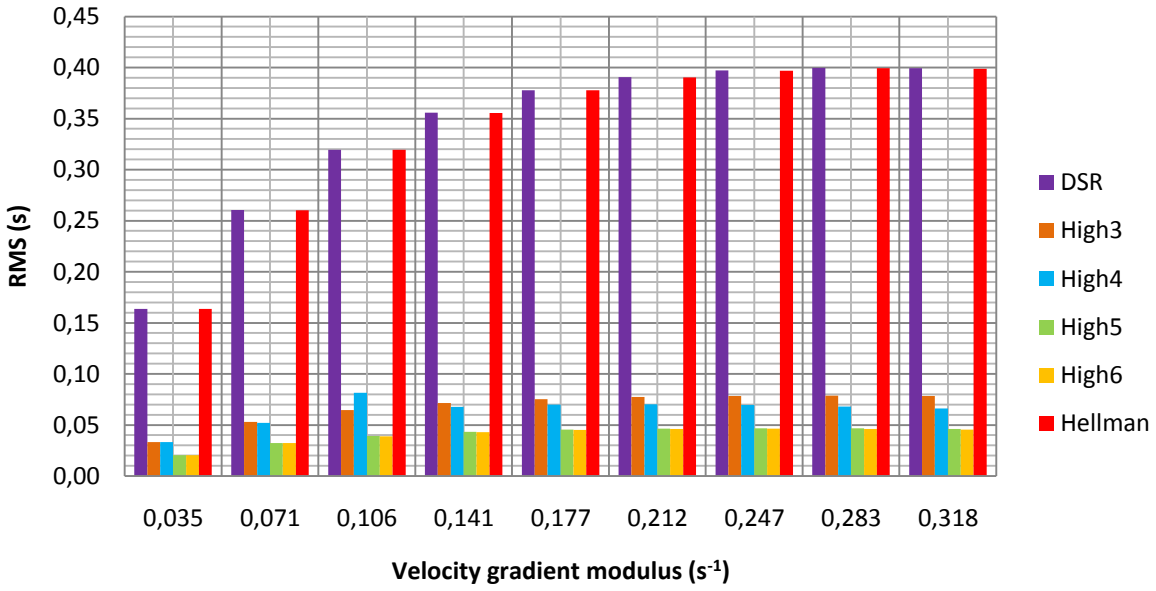

Figure 5.9: RMS errors for A45-seies. Velocity gradient modulus is 45 degrees with respect to the vertical, and gradually increased.

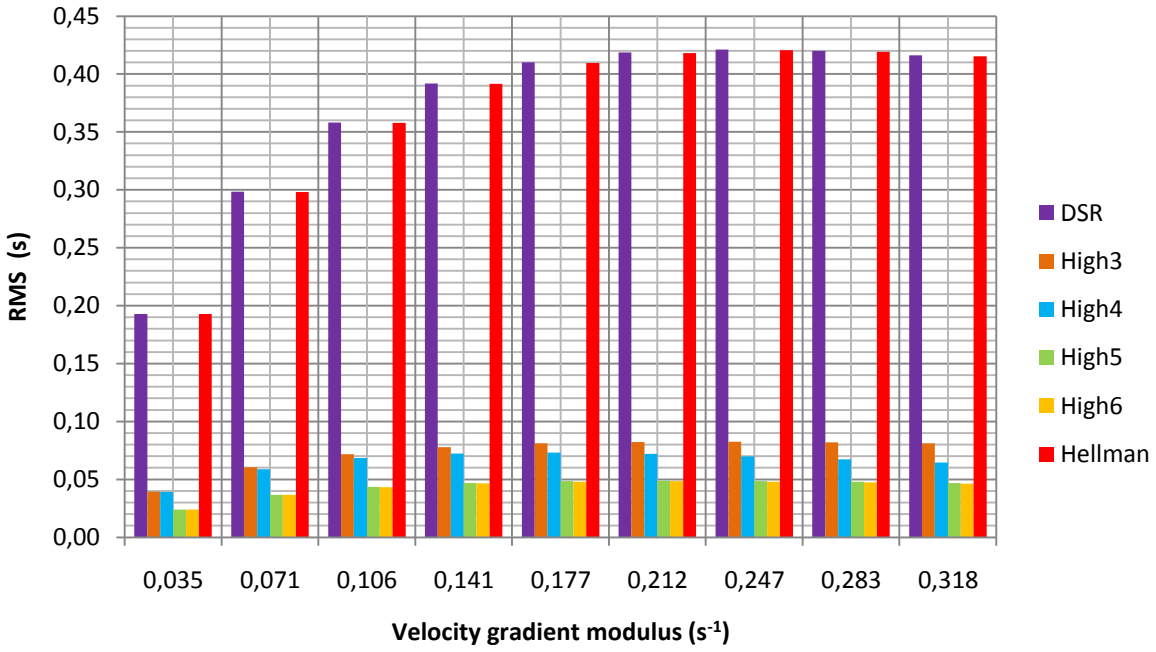

Figure 5.10: RMS errors for A60-seies. Velocity gradient modulus is 60 degrees with respect to the vertical, and gradually increased.

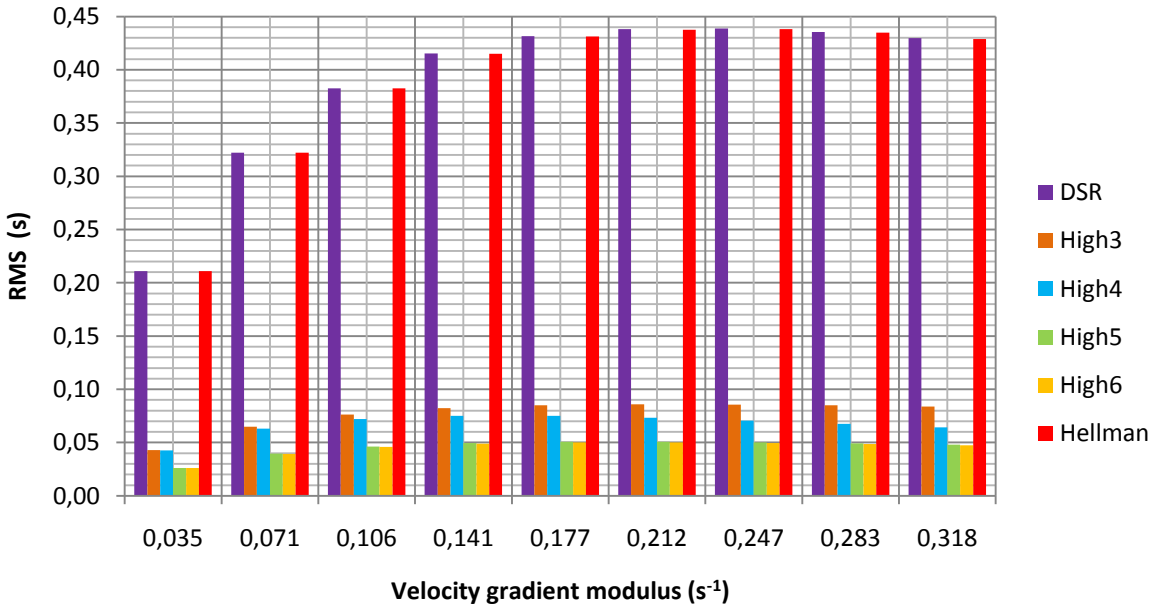

Figure 5.11: RMS errors for A75-seies. Velocity gradient modulus is 75 degrees with respect to the vertical, and gradually increased.

Due to the lateral velocity variations the diffraction-time surfaces are not symmetric, as the one shown for the last model in A75-series in *Figure 5.12*. The lateral velocity variation here is significant, and it explains the character of the time surface. The level of asymmetry increases for each series as the lateral velocity contribution increases. Similar to D-series, the overall RMS error for each series increases with increasing magnitude of the velocity gradient, but here the functions DSR and Hellman are not able to cope with the lateral velocity variations. The contribution of the even terms to reduce the RMS error is negligible. This is seen when High 3 is compared with High 4. They both give similar results. The functions High 5 and High 6 are also giving similar results. It is therefore not surprising that the functions Hellman and DSR give the same results, as we have seen that the contribution of the even terms are negligible. On the other hand, the odd term of 3rd order contribute greatly to reduce the RMS error as shown in *Appendix 3.2*. Here, the overall value of c_3 does not only increases with increasing magnitude of the velocity gradient modulus in each series. It also increases relatively between each series.

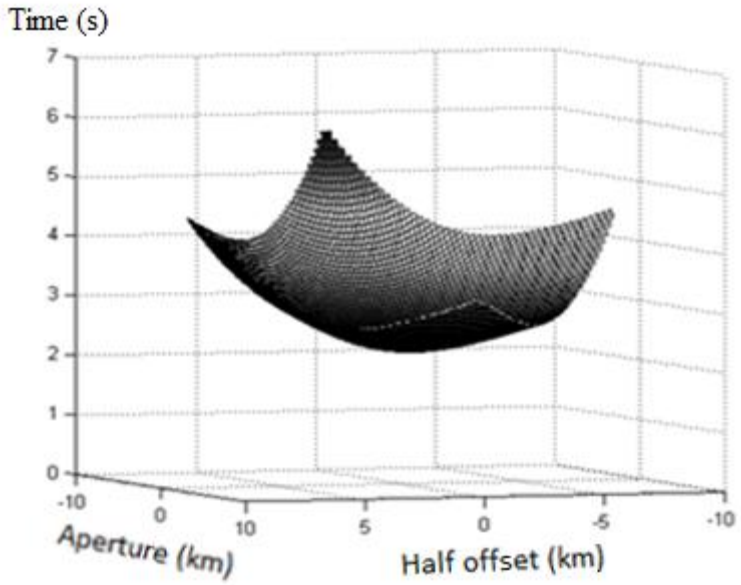

Figure 5.12: Diffraction -time surface when the velocity gradient is tilted 75 degrees with respect to the vertical (A75-series). Here the velocity modulus is 0.318 s^{-1}.

For the series A45, A60 and A75 the errors are somewhat large for the higher velocity gradients. However, the results obtained for the smaller velocity gradients and the other A-series, A30 and A15, the RMS errors are low and comparable with the results obtained in D-series. The odd term introduced are proving to be efficient in A-series.

Based on the period of the seismic signal, any RMS errors lower than 33 ms provides a good approximation. Consequently RMS errors larger than 33 ms indicates a poorer approximation, and thus a poorer resulting image than if the value was lower than 33 ms. However, the resulting image is not entirely dependent on the RMS error, but this gives an indication. Coherent noise corresponding to non-wanted sesmic energy (e.g. multiple reflections) can also affect the result. The data used in this work is noise free, which is not the case when real data is processed.

If geomodels with the same velocity gradient modulus are compared for each series, as shown on *Figure 5.13*, the RMS error increases with increasing lateral velocity contribution. Take for example the first model in A15 (*Figure 5.13a)* and A75 (*Figure 5.13b*), and compare the RMS errors for High 3. The RMS errors are 0.07 s and 0.21 s respectively. It indicates that the results are not only dependent on the magnitude of the velocity gradient, but also its direction.

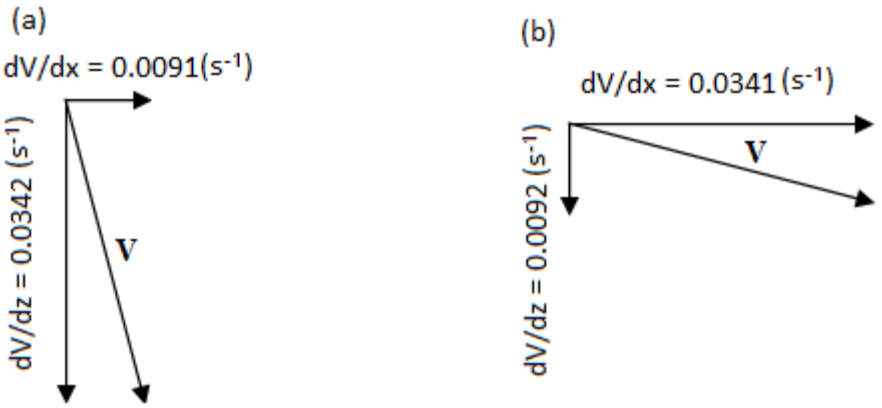

Figure 5.13: Showing the velocity gradients for the first model in A15-series (a) and A75-series (b).

Another interesting trend is observed when the second model in A30-series (*Figure 5.14a)* is compared with the first model in A75-series (*Figure 5.14b)*. Here, the lateral gradients (dV/dx) are similar, while the vertical gradient (dV/dz) is larger for the model in A30-series. The velocity gradient values are shown in *Figure 5.14*.

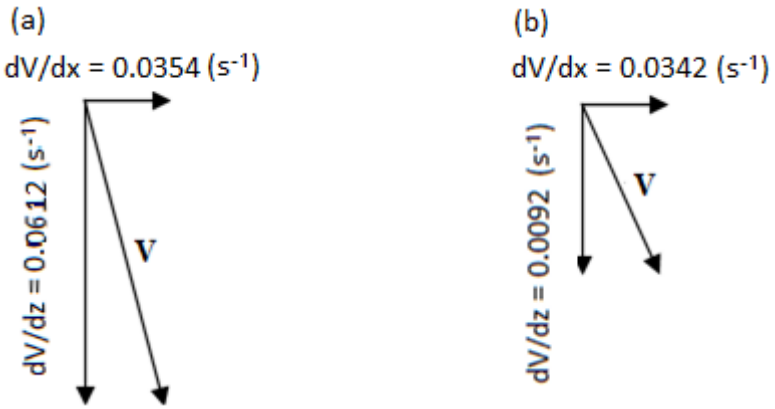

Figure 5.14: Showing the velocity gradients for second model in A30-series (a) and first model in A75-series (b).

The obtained RMS errors for each of the tested functions are shown for the two models in *Table 5.4.* From the table it is clear that the obtained results are almost identical. This indicates that the RMS error is much more sensitive to the lateral velocity gradient than to the vertical velocity gradient.

	A30-series	A75-series
DSR	0.204 s	0.210 s
High 3	0.042 s	0.043 s
High 4	0.043 s	0.043 s
High 5	0.025 s	0.026 s
High 6	0.025 s	0.026 s
Hellman	0.204 s	0.210 s

Table 5.4: RMS errors obtained for the second model in A30-series, and the first model in A75-series. Here the lateral gradients are similar, while the vertical gradient in A30-series is larger.

From the RMS error plots on *Figure 5.7* to *5.11*one can also see a clear tendency that the functions with odd terms have similar RMS errors, while DSR and Hellman continue to increase without any indication of stabilizing. For the purpose of illustration one can compare DSR and High 3 for the smallest and largest velocity gradient modulus in A30-series. The error for DSR increases from 0.122 s to 0.366 s, an increase of 300 %. High 3 increases from 0.025 s to 0.073 s, an increase of 292 %. Judging by these numbers the increase in RMS is similar, but in terms of mispositioning on the time image the additional odd term in High 3 improves the results evidently. In *Figure 5.15* the approximation of the diffraction-time surface done by the DSR function (*Figure 5.15b*) and High 3 function(*Figure 5.15c*) are shown for the diffraction-time surface where the velocity gradient modulus is 0.177 s^{-1} in the A75-series (*Figure 5.15a*). Due to the strong lateral velocity variation, there is a clear mismatch between the diffraction-time surface obtained by the DSR function and the synthetic diffraction-time surface. On the other hand the High 3 approach clearly yields a much better approximation.

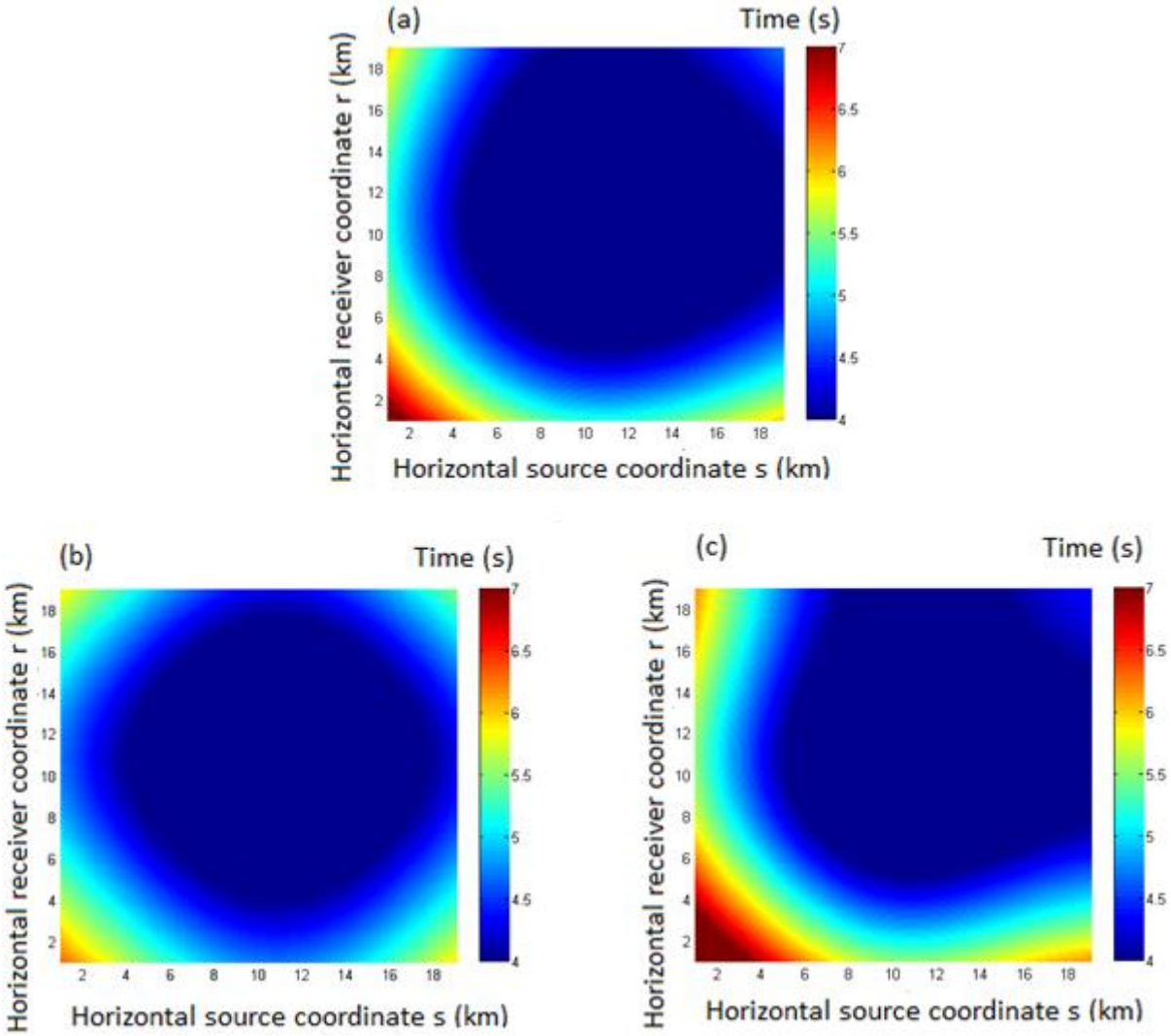

Figure 5.15: Comparison of synthetic diffraction-time surface, and approximated diffraction-time surface by DSR (b) and Hellman (c), for geomodel with velocity gradient modulus of 0.177 s^{-1} in the A75-series (a).

In *Appendix 3.2* one can see that the diffraction-time functions sometimes chose slightly different velocities to approximate the diffraction-time surface, as they have different degrees of freedom. For example, High 5 may choose a slightly lower migration velocity to achieve a better approximation than DSR for one model. For another model it can be opposite. Based on the results there is not a clear tendency showing that one or more functions are consequently choosing a lower or higher velocity than the others.

5.1.3 Lateral velocity variation (G- series)

For G-series the velocity gradient is in the lateral direction. Note that the geomodel where dV/dx is zero is not a homogenous isotropic medium, but one with periodic variations of amplitude *B* and period *L*. In *Figure 5.16* one can also see how the RMS error increases gradually with increasing lateral velocity gradient for DSR and Hellman, while High 3, 4, 5 and 6 stabilizes at 0.023 ± 0.003 s, 0.022 ± 0.004 s, 0.019 ± 0.001 s and 0.015 ± 0.003 s respectively.

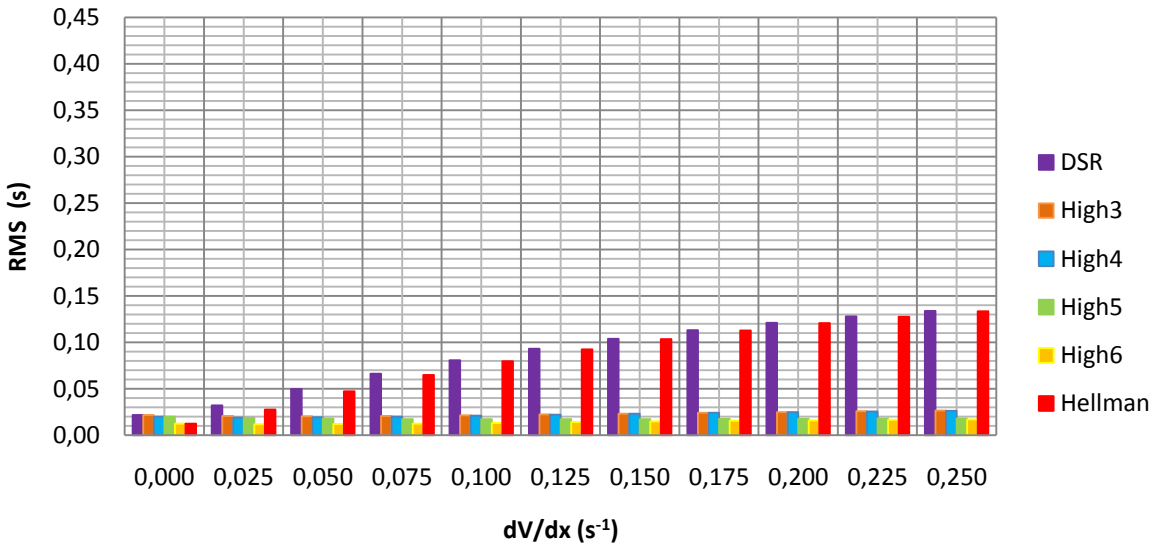

Figure 5.16: RMS values for G-series. DSR and Hellman increases with increasing lateral velocity. High 3, 4, 5 and 6 stabilizes at low RMS values

The observations made for the G-series are similar to the observations made for every A-series. In practice the G-series represents a continuation of the A-series where the velocity gradient is 90 degrees with respect to the vertical. Even terms in the diffraction-time functions do not contribute significantly to reduce the RMS error, while odd terms do. The overall magnitude of the RMS error is smaller than for the A-series. The reason is that the relative lateral velocity variation is much smaller for the G-series than for A-series.

5.1.4 Periodic subsection (P-series)

Two series, P1 and P2 were created with periodic changes in the velocity field. The RMS errors are shown in *Figure 5.17* and *Figure 5.18.* Recall that the reference position X_0 of the

incorporated velocity field is placed at the center of the geomodel in P1-series. In P2-series the reference point X_0 is shifted away from the center.

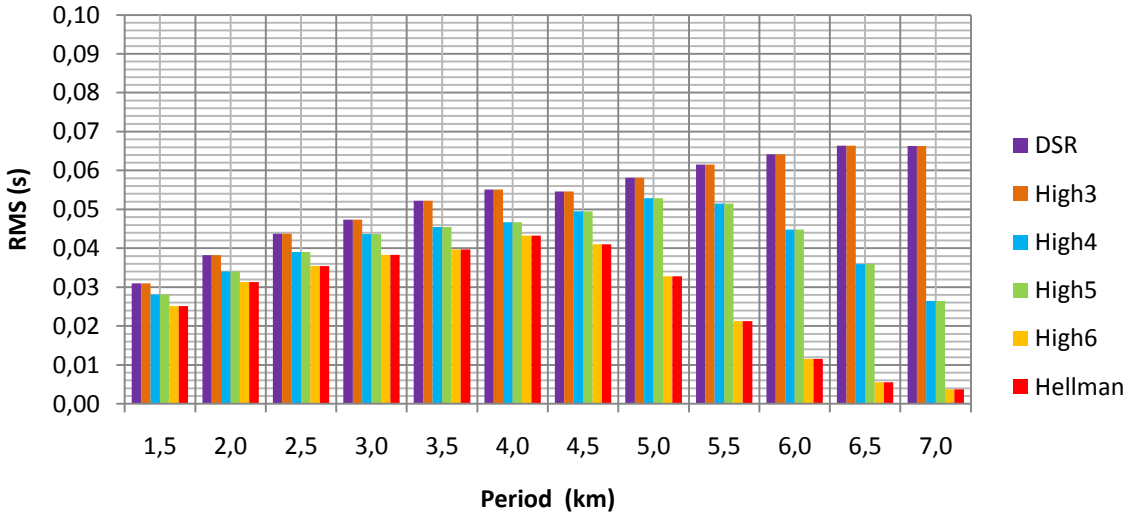

Figure 5.17: RMS errors for P1- series. DSR and High 3 are giving similar results. High 4 and High 5 are giving similar results. High 6 and Hellman are giving similar results.

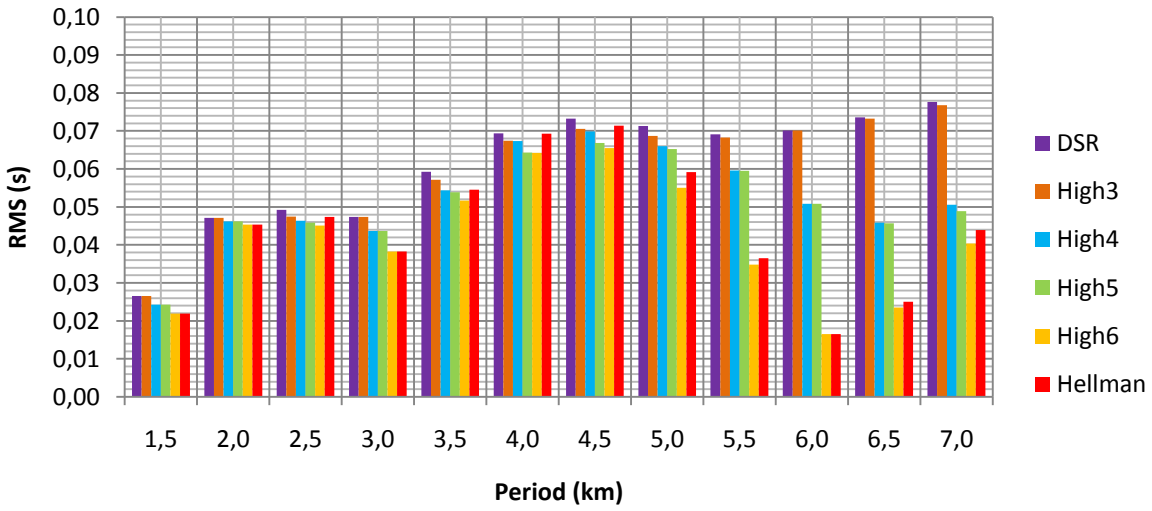

Figure 5.18: RMS errors for various diffraction-time functions. Geomodels are non symmetric, with periodic velocity changes.

The RMS error for both DSR and High 3 increases with increasing period L, while the remaining functions tend to reach a peak before they descend for the longer periods. A long period is in reality equivalent to a smoother velocity field, and the RMS errors are expected to be lower compared to the shorter periods. The observations made are therefore counterintuitive both in P1 and P2-series. For the shorter periods the functions give better results than when the period is for example 4.5 km. One possible explanation can be that the

periodic changes in the velocity fields are too rapid for the ray paths to get affected, and thereby create a simple diffraction-time surface to approximate as shown in *Figure 5.19.* The figure shows the diffraction-time surface when the period is 1.5 km in P2-series. On the other hand, models with slightly longer periods give the rays more space to bend, and hence create a more complex diffraction-time surfaces to approximate.

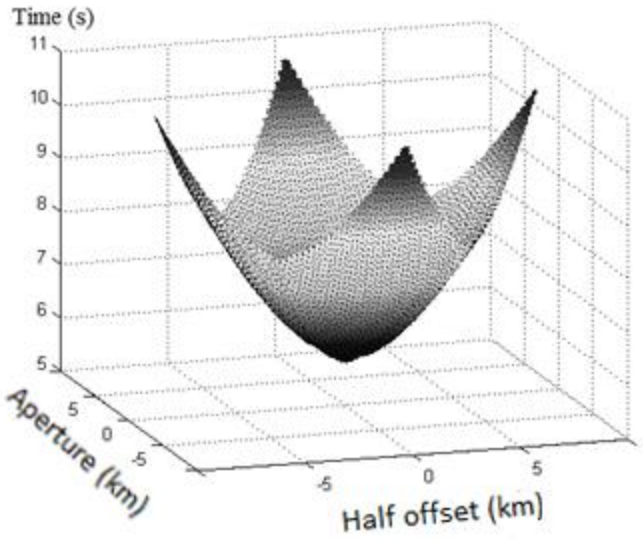

Figure 5.19: Diffraction -time surface for a model in P2-series. Here the period L is 1.5 km in Eq. 4.2.

In P2-series the RMS error also increases again for High 4, High 5 and High 6 and Hellman when the period is larger than 6.5 km. An explanation for this observation is unknown. For future studies, it is recommended to conduct more test series where the reference point X_0 is shifted to see if this trend is consistent.

In *Figure 5.20* the diffraction-time surface for two models in P2-series are shown. The periods *L* used in *Eq. 4.2* in the respective models are 4.5 km (*Figure 5.20a)* and 6.0 km (*Figure 5.20b). Figure 5.20a* shows an asymmetric diffraction-time surface, while *Figure 5.20b* shows a symmetric diffraction-time surface. When the figures are compared with their respective RMS errors in *Figure 5.18* one can see that Hellman efficiently reduces the RMS error to a value below 0.033 ms for the model represented by *Figure 5.20b.* The Hellman function gives the same results as High 6. On the other side none of the higher-order functions are obtaining acceptable RMS errors when the period *L* is 4.5 km. Previously we saw that simple asymmetric diffraction-time surfaces were better approximated by the new functions with higher-order odd terms. Here, the character of the time surface is more complex. Thus, it

becomes more difficult to approximate, even for the new functions tested here. It is therefore reasonable to believe that odd terms of higher-order are not always effective for asymmetric diffraction-time surfaces, but depend on the shape of the time surface. Other studies have also shown that additional terms in the diffraction-time functions do not necessarily provide a better approximation (Causse, 2004).

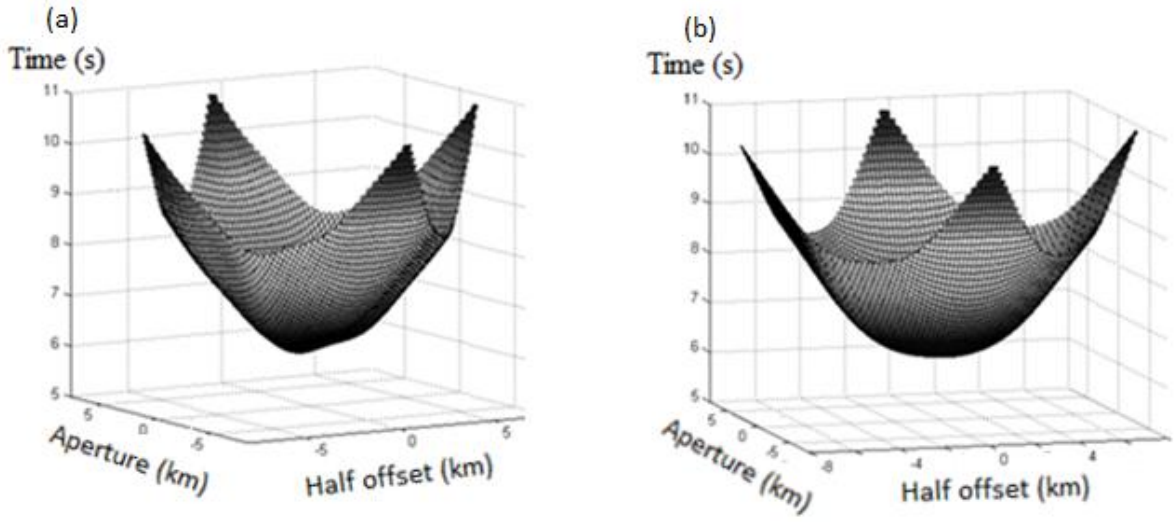

Figure 5.20: Diffraction-time surface for two models in P2-series. Left image showing when the period is equal to 4.5 km and right image showing when the period is 6.0 km in Eq. 4.2.

The diffraction-time surface in *Figure 5.20a* also appears to be more complex than the time surface represented in *Figure 5.19.* It probably explains why RMS errors are lower for the shorter periodic velocity changes, rather than higher as one would expect.

Even though the earlier observations indicate that better approximations of the diffraction-time surface is possible by introducing higher-order terms, these results above clearly indicate a weakness of the new functions, and show that depth migrations is still necessary in areas with complex velocity distribution.

5.1.5 Caustics (K-series)

The last isotropic series tested in this work is the K-series. The complexity of the velocity model was increased gradually. The complexity was increased by reducing the period *L* in *Eq. 4.2,* and caustics were observed for K5 and K6. For the tested models the overall observations show that the higher-order functions are achieving better result than the conventional DSR

function, as shown in *Figure 5.22*. Note that also the Hellman function is marginally better than the DSR function. The contribution of the odd terms to reduce the RMS error is greater than the even terms, but as one can see the even terms also contribute. For model K2, the RMS error decreases from 0.040 s for High 5 to 0.036 s for High 6.

The obtained RMS errors are generally too high in this series. From the ray path for K6 in *Figure 5.21* it becomes clear that the resulting diffraction-time surface is far from simple and explains the overall high RMS error for this series. But, one can clearly see the benefit of introducing the additional constants to the conventional diffraction-time function. The results indicate that in areas where the velocity field changes less drastically, one can achieve acceptable approximations by introducing even and odd terms of higher-orders. Thus, it also emphasize that the applicability of prestack time migration can be extended by introducing the additional higher-order terms.

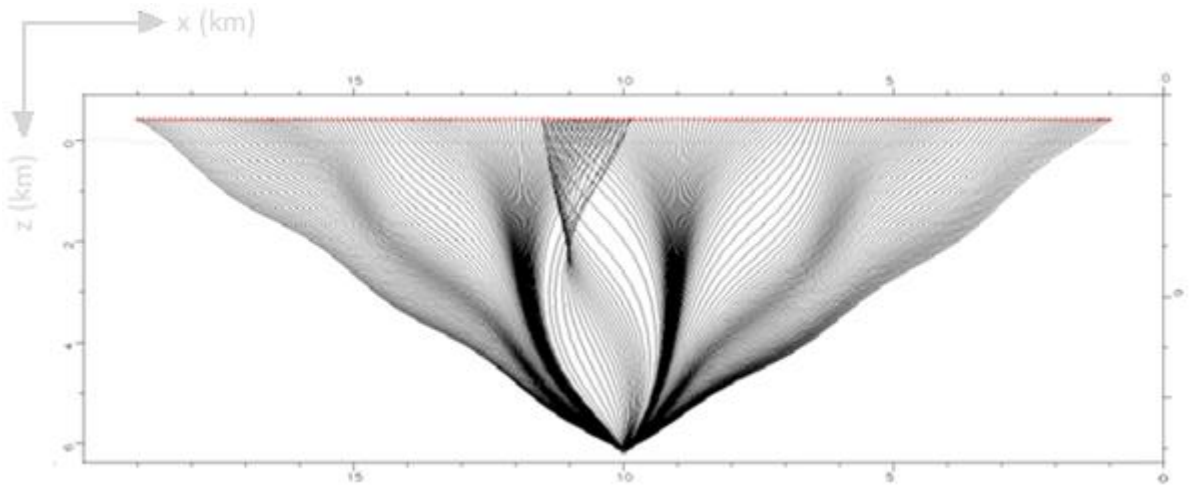

Figure 5.21: Ray paths for model K6. The figure shows how rays intersect for a complicated velocity model and creates caustics.

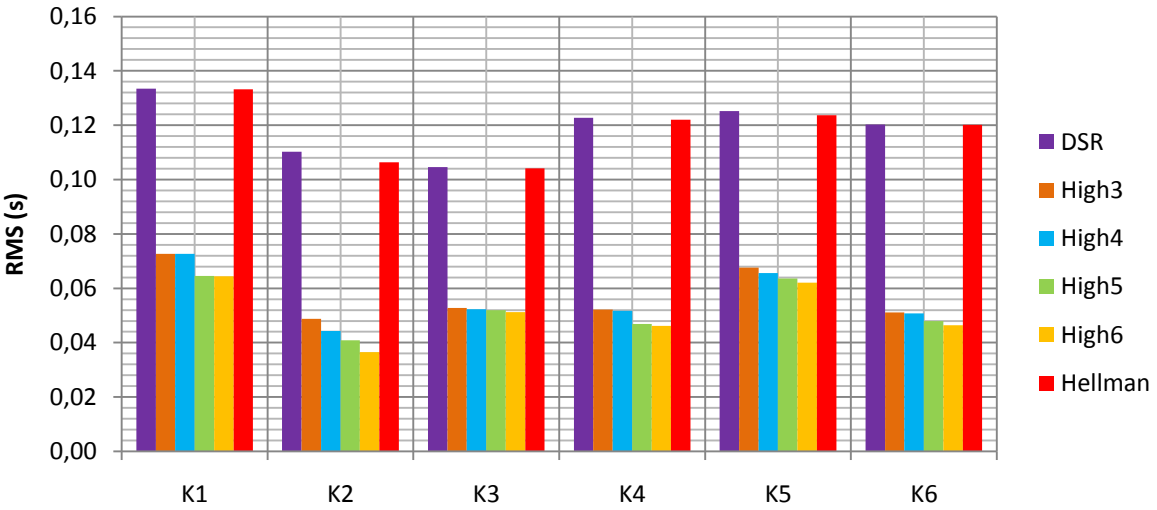

Figure 5.22: RMS errors for K- series. Caustics were observed for K5 and K6.

5.2 Discussion

Causse (2004) developed a travel time approximation for the purpose of non-hyperbolic move out. His approach was similar to what is done in this work. Synthetic models were created, and a least square fitting approach was used to determine the five additional coefficients in the new function. The models were tested on isotropic media, and he found that the new function improved the results with several orders of magnitude. However his approach is only valid for vertically varying velocity fields with little or no lateral variations. He indicates that his function also should be applicable for time migration purposes for both isotropic and anisotropic cases, though it has not been tested. We have also observed the advantage of introducing additional terms to the diffraction-time functions. However, our results have not shown improvements of the same magnitude as found in Causse (2004).

For the isotropic models, we have seen an overall improvement by introducing additional terms to the diffraction-time functions when simple diffraction-time surfaces are approximated. Using both even and odd terms has lead to reduced diffraction-time errors. We have also seen that for more complex diffraction-time surfaces, where lateral velocity variations are present, the additional terms are not able to reduce the RMS error below 33 ms. However, the results indicate that prestack Kirchhoff time migration can be extended to work in areas with moderate lateral velocity variations, while more complex velocity variations still requires depth migration.

Determining the additional coefficients used in this work must be done by velocity analysis when processing the actual seismic data. As this is not a straight forward process, it is desirable to keep the number of additional coefficients at a minimum. Keeping the numbers at a minimum also reduces computer time. When it comes to determining which additional terms to include, I suggest that one should consider the velocity distribution in the subsurface. In areas with moderate lateral velocity variations, which results in simple asymmetric diffraction-time surfaces, odd terms can improve the approximation. In areas where only vertical or periodic velocity variations which results in simple symmetric diffraction-time surfaces, additional even terms can also improve the resulting time image. The lateral velocity distribution can be determined if velocity analysis is performed at several points along the acquisition surface.

As mentioned, coherent noise can also affect the results. Further testing of diffraction-time functions should therefore be conducted using real seismic data.

6 Anisotropic media

In this chapter, test results performed on anisotropic heterogeneous media are presented and discussed. The results are also shown in tables in *Appendix 4*. Media are anisotropic if material properties are directionally dependent. It can result from materials being non-uniform in an especially organized way. Anisotropy is affected by several lithological parameters such as composition, shape, orientation, size and packing and is present in different geological settings at different scales (Gelius and Johansen, 2010).

Although anisotropy is present at different scales, seismic data analysis is often performed based on the assumption that the subsurface behaves as an isotropic medium on a seismic scale. Isotropic media have material properties which are not directionally dependent as mentioned in *Chapter 4*. This is often good as a first approximation in the earth, but it is sometimes important to consider deviations from isotropy (Stein and Wysession, 2003). If an anisotropic medium is assumed to be isotropic, and the acquired data is processed without taking anisotropy into account, it can potentially produce seriously biased results.

If more than two independent elastic parameters are needed to represent a medium, one have an anisotropic medium. The simplest anisotropic case of broad geophysical applicability has one distinct direction, while the other two are identical (Thomsen, 1986). It is known as a transverse isotropic (TI) medium.

In this work, we are testing the effect of vertical transverse isotropy (VTI) and tilted transverse isotropy (TTI). For the VTI medium the axis of symmetry is vertical, and for the TTI medium the axis of symmetry is tilted 15^o with respect to the vertical. VTI media can be observed in the subsurface, as a result of deposition of sediments which creates horizontally layered sections. An example can be seen in *Figure 6.1*, where the axis of symmetry is in the X_3 direction.

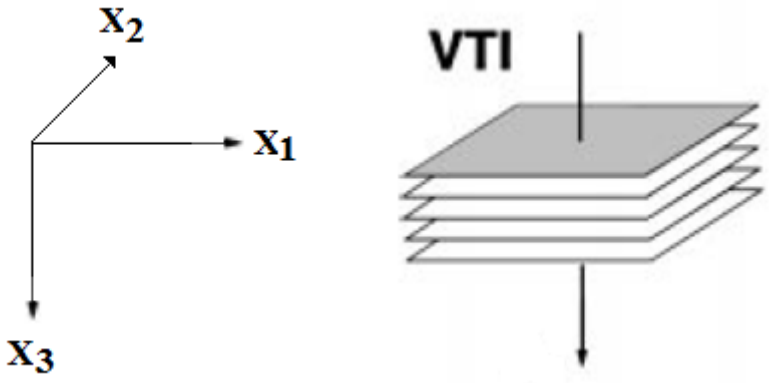

Figure 6.1: Illustration of a VTI medium. Axis of symmetry along the X_3 axis (Rüger, 1997).

The elastic constant matrix for a VTI medium is given by

$$C_{\alpha\beta} = \begin{Bmatrix} C_{11} & C_{11}-2C_{66} & C_{13} & & & \\ C_{11}-2C_{66} & C_{11} & C_{13} & & & \\ C_{13} & C_{13} & C_{33} & & & \\ & & & C_{44} & & \\ & & & & C_{44} & \\ & & & & & C_{66} \end{Bmatrix}, \qquad \text{Eq. 6.1}$$

where C_{11} is $\lambda + 2\mu$ in the X_1 and X_2 direction. C_{66} is μ in the X_3 direction, and C_{44} is μ in the X_1 and X_2 direction. The entity C_{13} can also be interpreted geometrically, as will be described by *Eq. 6.5* below.

TTI media are also commonly present in the subsurface. TTI media can be found in areas with up-thrusting geological features. In areas with salt domes one can often observe dipping shale layers truncating towards the flanks (Yilmaz, 2001).

In a homogeneous isotropic medium, a point source would generate expanding waves with spherical shape. That is not the case for anisotropic media. Here, properties are directionally dependant, including medium velocities. The propagating wave will therefore deviate from the perfectly spherical shape. The directional change of the velocity can be visualized by a skewed ellipse as shown in *Figure 6.2*.

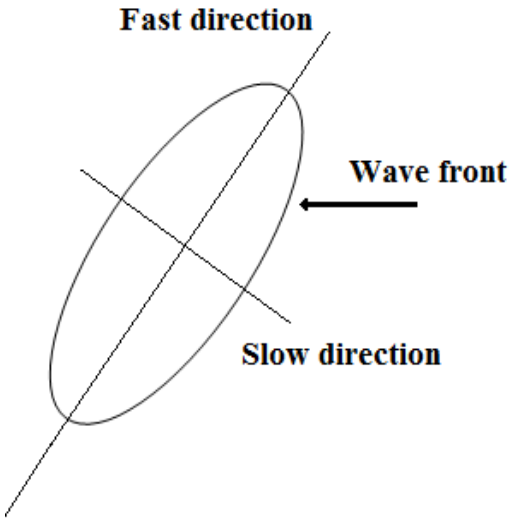

Figure 6.2: Skewed ellipse illustrating a wavefront propagating in a TTI medium.

Here the velocity is faster along the major axis, and slower along the minor axis. The wavefront is skewed in the fast direction. When the wavefronts are skewed, rays are not necessarily perpendicular to the wavefronts anymore (Alkhalifah and Tsvankin, 1995).

Thomsen (1986) suggested a new notation to represent anisotropy. In addition to two established velocities P-velocity (α_0) and S-velocity (β_0) along the symmetry direction, he introduced three new parameters ε, γ and δ which directly reflect the degree of anisotropy. The P-velocity and S-velocity is given by

$$\alpha_0 = \sqrt{\frac{C_{33}}{\rho}},$$

Eq. 6.2

$$\beta_0 = \sqrt{\frac{C_{44}}{\rho}},$$

Eq. 6.3

where ρ is the density.

Further, ε, δ and γ are given by

$$\varepsilon = \frac{(C_{11}-C_{33})}{2C_{33}},$$

Eq. 6.4

where ε represents the fractional difference between the horizontal and vertical P-velocity.

$$\delta = \frac{(C_{13}+C_{44})^2-(C_{33}-C_{44})^2}{2C_{33}(C_{33}-C_{44})},$$

Eq. 6.5

where δ represents the near vertical velocity variation.

$$\gamma = \frac{(C_{66}-C_{44})}{2C_{44}},$$

Eq. 6.6

where γ represents the fractional change in SH-velocity. In this work the parameter has not been granted any further attention as we are working with P-velocities.

In 1995 a new effective anisotropy parameter η was introduced by Alkhalifah and Tsvankin. η is given by

$$\eta = \frac{(\varepsilon-\delta)}{(1+2\delta)}.$$

Eq. 6.7

In *Figure 6.3* the wavefronts for both isotropic and anisotropic cases are shown. The isotropic case, illustrated by the dotted line, has a spherical shape. On the other hand, the wavefront (solid line) deviates from the spherical shape for the case of anisotropy where $\varepsilon = 0.2$ and $\delta = -0.2$. The wavefront is skewed, similar to *Figure 6.2* but in a more complex fashion. Here the velocity is faster in the vertical direction, which can be considered as the major axis.

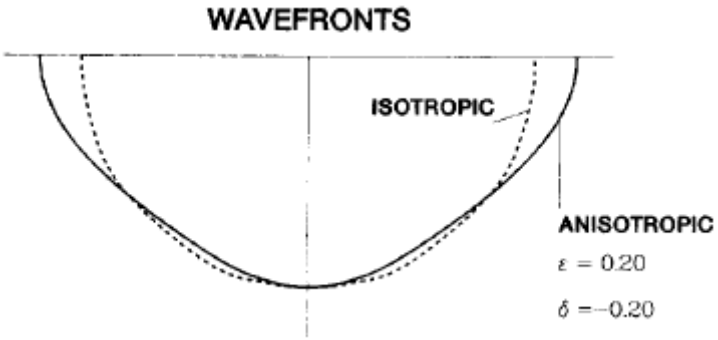

Figure 6.3: Comparison of wavefronts. Solid line representing wavefront for anisotropic case. Note the skewed character. Dotted line representing wavefront for isotropic case (Thomsen, 1986).

If $\varepsilon = \delta$ one has an elliptically shaped wavefront. Hence it is referred to as elliptical anisotropy. However, it does not serve any physical justification (Thomsen, 1986; Alkalifah and Tsvankin, 1994). As a matter of fact ε and δ sometimes have opposite signs in nature (Gelius and Johansen, 2010). In *Table 6.1* laboratory measurements for ε, δ are shown for a few rocks and crystals, and the calculated η from *Eq. 6.7*.

Sample	ε	δ	η
Mesaverde - clayshale	0.189	0.204	-0.010
Mesaverde - sandstone	-0.026	-0.033	0.007
Green River shale	0.195	-0.220	0.741
Oil Shale	0.200	-0.075	0.323
Calcite crystal	0.369	0.579	-0.097
Muscovite crystal	1.120	-0.235	2.557

Table 6.1: Values for ε, δ obtained in laboratory test (Thomsen, 1986), and calculated η from Eq. 6.7.

In this work, tests have been performed with δ ranging from -0.2 to 0.2, while ε was fixed as 0.2. It enabled one to study the effect of anisotropy of different amplitude. A total of four series were tested. The first series had a vertical varying velocity field and was tested for VTI. The second had a vertically varying velocity field and was tested for TTI, where the axis of symmetry was tilted 15^0 with respect to the vertical. The third series had a velocity gradient 15^0 with respect to the vertical, and was tested for VTI. The last series was tested for TTI when both the velocity gradient was 15^0 with respect to the vertical, and the axis of symmetry for anisotropy was tilted 15^0 with respect to the vertical.

6.2 Results

Receiver position, diffraction point and density used for each model were the same as for the isotropic models. The velocity gradient for the tested models had a magnitude of 0.247 s^{-1} in each model. It is the same value used for the 7^{th} model in each series in *Chapter 4.1.2*. *Figure 6.4* shows the RMS errors for the vertically varying velocity field with VTI. The arrows show the axis of symmetry for the tested anisotropy and the direction of the velocity variation. δ

decreases from 0.2 to -0.2 towards the right with an interval of -0.1. For example VTI1 has the anisotropy parameters δ = 0.2 and ε = 0.2, while VTI5 has the value δ = -0.2 and ε =0.2.

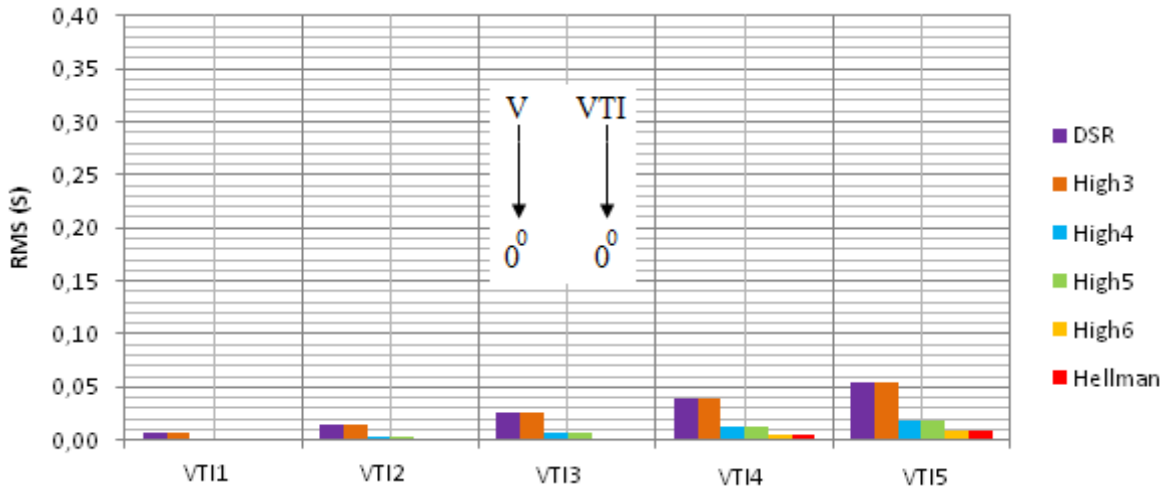

Figure 6.4: RMS errors for vertically varying velocity field tested for VTI.

Figure 6.5 show the RMS errors for a vertically varying velocity field, and TTI with a symmetry axis of 15^0 with respect to the vertical. The Thomsen parameters change in the same manner as mentioned above. For example, TTI1 has the anisotropy parameters δ = 0.2 and ε = 0.2, while TTI4 has the values δ = -0.1 and ε = 0.2.

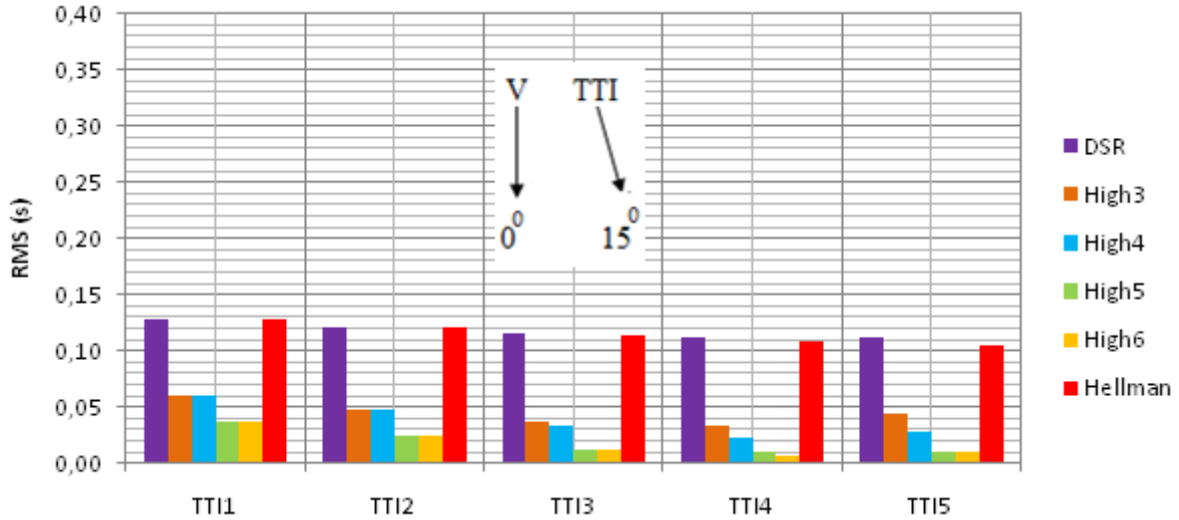

Figure 6.5: RMS errors for vertically varying velocity field tested for TTI.

Figure 6.6 show the RMS errors when the velocity gradient is 15^0 with respect to the vertical and VTI. This is also indicated by the arrow on the figure. ε is unchanged, while δ changes similar to the previous series in this chapter.

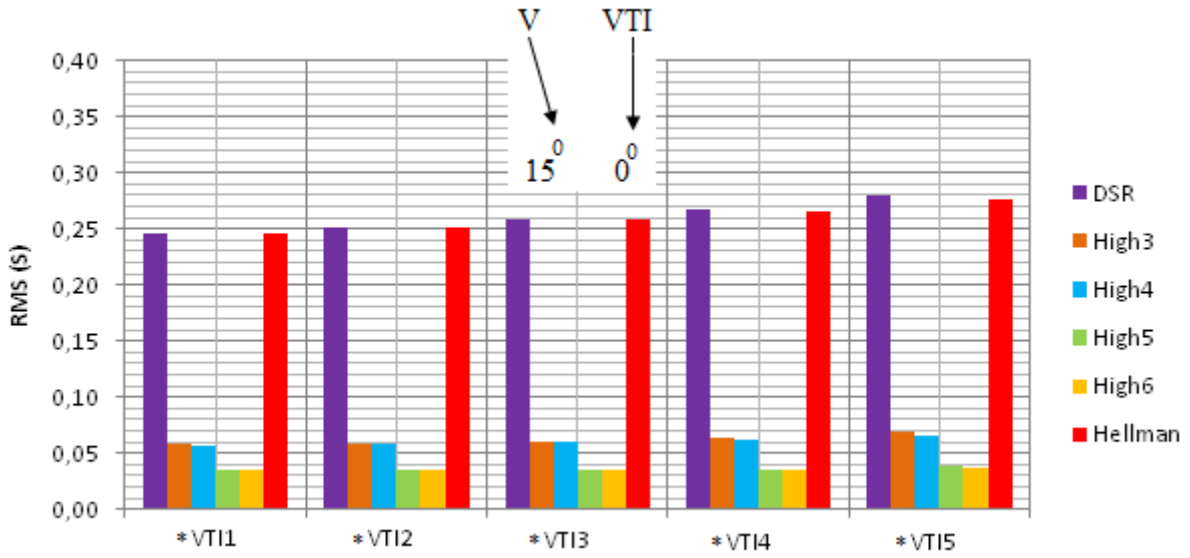

Figure 6.6: RMS errors for tilted velocity field tested for VTI.

Figure 6.7, show the RMS errors when the velocity gradient is 15^0 degrees with respect to the vertical, and the axis of symmetry for anisotropy is tilted 15^0.

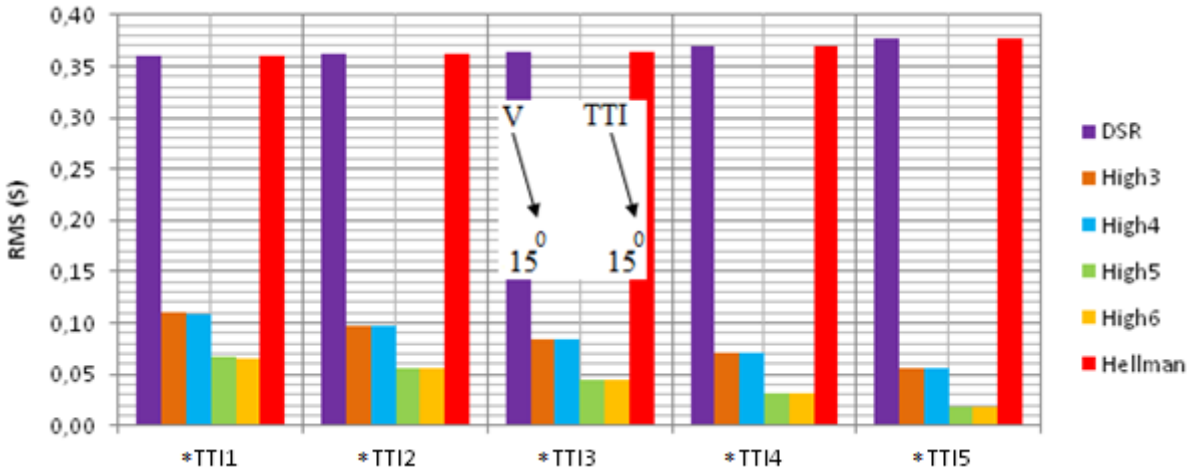

Figure 6.7: RMS errors for tilted velocity field tested for TTI.

6.3 Discussion

In anisotropic heterogeneous media the energy propagates at different speeds not only because of variation in velocity with position, but also because of its variation with direction of propagation. The diffraction-time functions therefore have to cope with both types of variations, while previously in the isotropic models they only had to cope with velocity variation with position.

Low RMS errors were obtained when the diffraction- time functions approximated the travel times in vertically varying velocity fields with VTI symmetry (*Figure 6.4)*. The highest RMS errors were then obtained by DSR and High 3. The highest error is just below 0.06 s, when $\delta = -0.2$ and $\varepsilon = 0.2$. Due to the symmetry of the diffraction- time surface, the additional term in High 3 does not have any affect. The simple symmetric character also enables the Hellman approach to function effectively. These observations are similar to what was made in D-series for the isotropic models. Thus, the RMS errors obtained by the Hellman function are very low compared to the other functions except the High 6 function which also have two additional even terms similar to Hellman. In *Appendix 4.1* the coefficients c_3 and c_5 in High 6 were approximately equal to zero. Thus, the High 6 function was reduced to become a Hellman function in practice. Note that the values for c_6 are larger than zero, but too small to be shown in *Appendix 4.1* . The diffraction-time surface for VTI1 is shown in *Figure 6.8*.

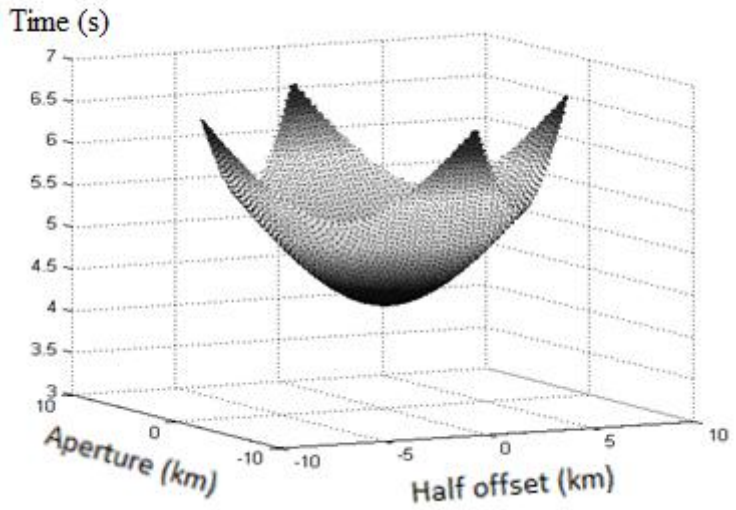

Figure 6.8: Diffraction-time surface for VTI1.

Another key observation made is that the RMS errors are sensitive to the parameter η in TI media. Within each series the RMS error changes with η. When the models are tested for VTI, a small increase in RMS values with increasing η is observed. On the other hand, when the models are tested for TTI a small decrease is observed with increasing η for some of the functions. For future studies it is recommended that tests are conducted with different symmetry axis to confirm this trend.

In the next three following test series (*Figure 6.5, 6.6 and 6.7)*, it is clear that DSR and Hellman obtain the largest RMS errors, even for the vertically varying velocity field tested for TTI. *Figure 6.9* shows the diffraction-time surface in the source-receiver domain obtained by synthetic data and the approximated surface from DSR and High 3 function. The comparison is done for model *TTI3. There is a distinct difference. The surface obtained by the synthetic data (*Figure 6.9a)* is asymmetric as a result of the lateral velocity variation and anisotropy. When DSR tries to approximate the synthetic data (*Figure 6.9b*) one can clearly see by the color coding that it is not very accurate. High 3, clearly yields a much better approximation (*Figure 6.9c*).

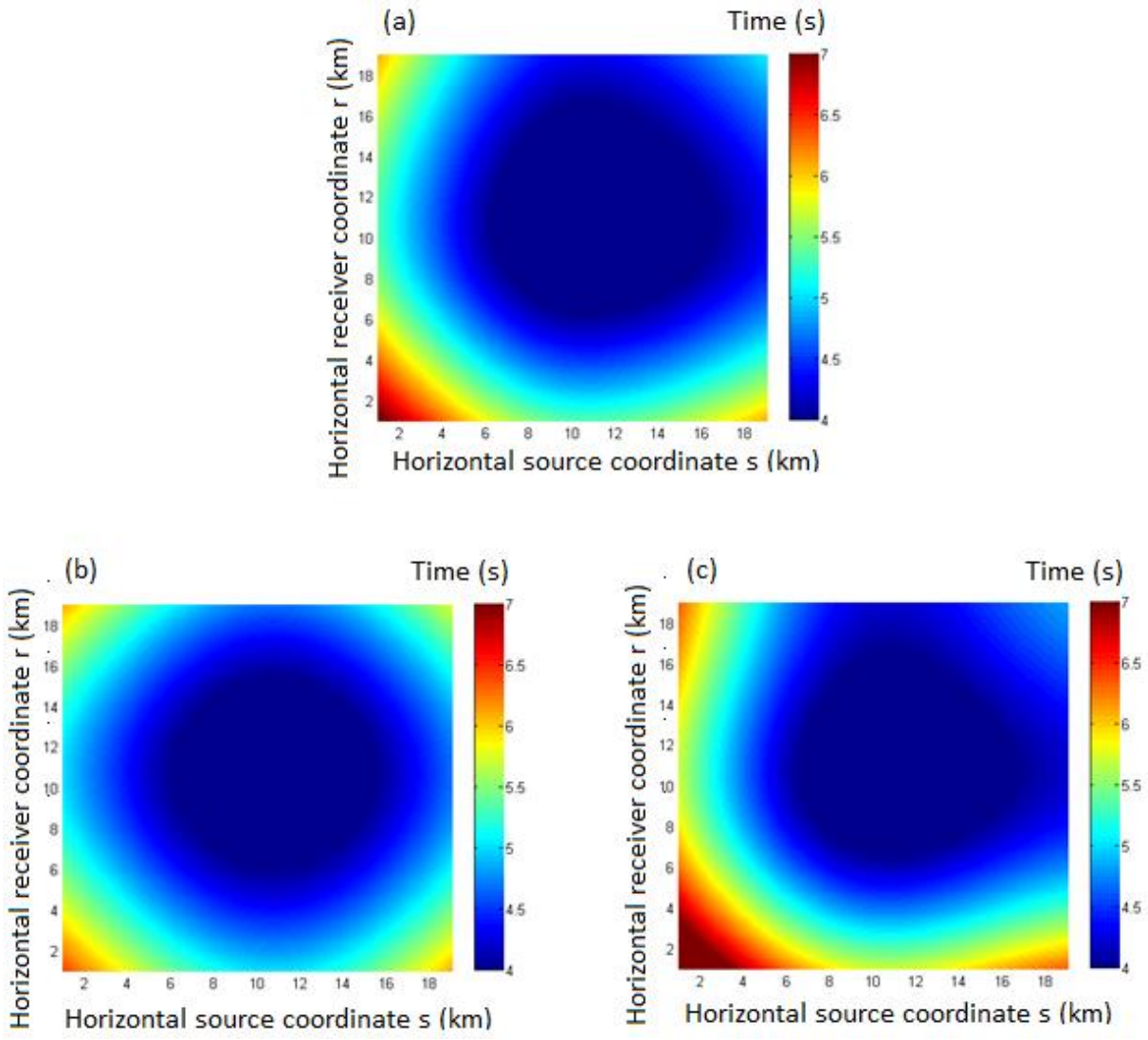

*Figure 6.9: Comparison of synthetic diffraction-time surface (a) and the one approximated by DSR (b) and High3 (c) for *TTI3.*

If a similar comparison is done for model VTI3, it is clear that the DSR function (*Figure 6.10b)* achieves a better approximation of the synthetic diffraction time surface (*Figure 6.10b)* as seen in *Figure 6.10*. From a visual point of view the two time surfaces look almost identical.

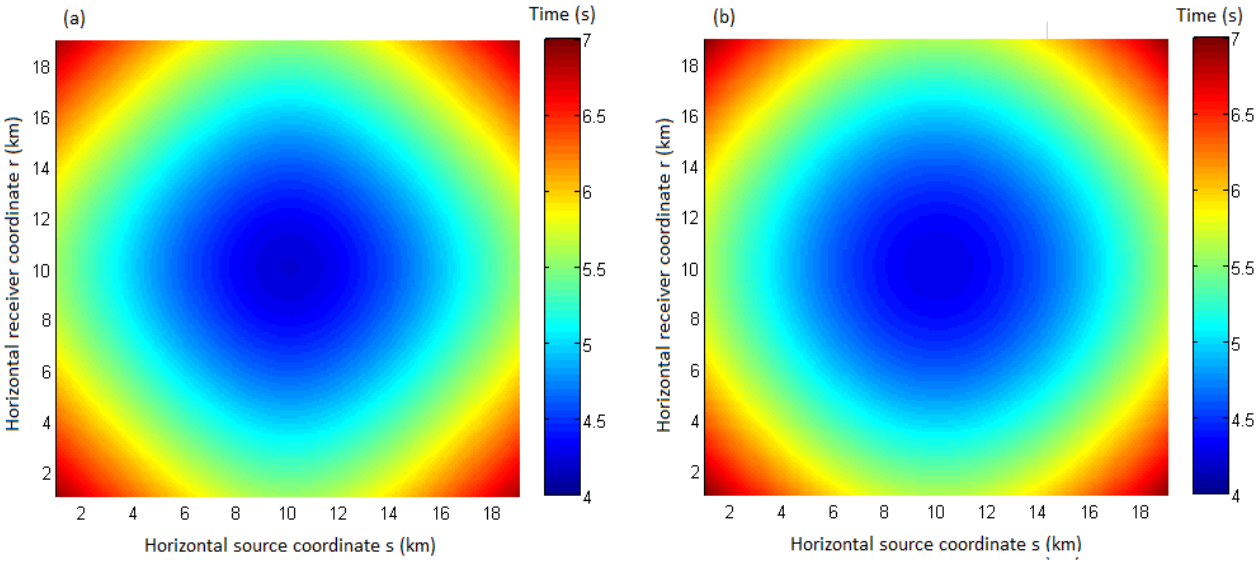

Figure 6.10: Comparison of synthetic diffraction-time surface (a) and the one approximated by DSR (b) for VTI3.

These observations point towards the same conclusion made for the isotropic models. Simple asymmetric diffraction-time surfaces require at least one odd term to become an acceptable approximation. Simple symmetric diffraction-time surfaces become better approximations by adding even higher-order terms. *Figure 6.5*, *6.*6 and *6.7* also indicate that it is advantageous to introduce not only one, but two odd terms to reduce the RMS error to be comparable with the typical period of the seismic signal. On the other hand one additional even term is enough to achieve acceptable results for the tested models in *Figure 6.4.*

One can also see that the effect of changing the direction of the velocity gradient from 0^0 to 15^0 has a larger impact on the RMS error than changing the axis of symmetry for anisotropy correspondingly. This can be seen when *Figure 6.5* and *Figure 6.6* is compared. The largest RMS errors overall are obtained when both direction of the velocity gradient is 15^0, and the axis of symmetry is tilted 15^0.

It was mentioned above that ignoring anisotropy could potentially result in biased images. Studies have shown that the travel time approximation error increases with offset (Al-Dajani

and Tsvankin; 1998). Seismic processing often neglects anisotropy because it is complicated, and lead to slow and costly processing. The most difficult task has proven to be to recover the anisotropic velocity field. To recover the anisotropic velocity field one has to determine the independent elastic coefficients (Alkhalifah and Tsvankin, 1995). Recovering the independent coefficients is especially difficult because of the limited angle coverage of the reflection survey. Another explanation for why anisotropy has been neglected is because the processing approaches used in isotropic media have functioned well, even in presence of anisotropy. Ignoring anisotropy has most likely led to errors which have been unrecognized, and therefore untreated (Alkhalifah and Larner, 1994).

Alkhalifah and Larner (1994) showed how δ and ε affected the approximation error, similar to what is observed here. They also showed that the error versus dip behavior depends in a complicated way on the vertical velocity gradient, vertical travel time and the orientation of the symmetry axis. Even though their approach to prove this behavior is different from the one used in the present work, the results are interesting. We have shown for the anisotropic models that the error is mainly dependent on the magnitude of the lateral velocity gradient, and less on the anisotropy parameters. Note that we have not studied the error dependency with respect to the dip behavior for transversely isotropic media, and are therefore not able to determine if the error versus dip is greatly dependent on the vertical velocity gradient for transversely isotropic media. However, the observations made for the isotropic models show that the vertical velocity gradient has less influence on the RMS error.

Assuming that the anisotropic velocity field is recoverable, our observations indicate that it can be advantageous to introduce additional terms. For a vertically varying velocity field, with a vertical axis of symmetry even terms contribute to reduce the RMS error. For the other three tested scenarios odd terms have proven to be most efficient. Depending on the information gained by the recovered velocity field one should determine which additional term to include in the conventional DSR diffraction-time function.

7 Conclusions

Velocity fields were created and incorporated into isotropic and anisotropic geomodels to study the effect of introducing additional terms to the conventional DSR diffraction-time function. The results obtained using the new functions were compared to the pre-existing DSR and Hellman functions. The comparison was first performed by a scanning technique, which proved to be too time consuming. A new least square surfaces fitting method was developed which enabled one to test accurately and efficiently.

The main conclusions from this work are summarized below:

- We have seen that the RMS diffraction-time error increases with increasing lateral and vertical velocity gradient. For isotropic media, we have also seen that the diffraction-time error is more sensitive to the lateral velocity gradient than to the vertical velocity gradient.

- Introducing higher-order even terms can improve the diffraction-time error of simple symmetric diffraction-time surfaces corresponding to vertically varying velocity fields. This is also true for tests conducted on anisotropic models with vertical axis of symmetry.

- The Hellman approach obtained good approximations for vertically varying velocity fields in isotropic models, and vertically varying velocity fields in anisotropic models with a vertical symmetry axis.

- The results indicate that the applicability of prestack Kirchhoff time migration can be extended. For asymmetric diffraction-time surfaces corresponding to TTI and/or laterally varying velocity media it can be advantageous to introduce higher-order odd terms to improve the approximation, both for isotropic and anisotropic media, as long as the diffraction-time surfaces are simple.

- Additional terms are not a guarantee to achieve better approximations, as the possibility of a good result depends largely on the character of the diffraction-time surface to be approximated.

- We have confirmed that the RMS error is sensitive to the anisotropy parameter η. The RMS errors increased with increasing η for VTI media. On the other hand a small decrease was observed for TTI media with increasing η. More tests must be conducted to verify the observation.

Which additional term to introduce should be determined by the character of the velocity field. It is desirable to keep the additional terms at a minimum, as it is no a straight forward process to determine them. It will also keep the computer time associated with the migration process at a minimum. In some areas a combination of even and odd terms of higher-order can be required.

In the present work, the actual migration process has not been carried out. We have performed travel time approximations for the purpose of prestack migration. Causse (2004) and, Fomel and Stovas (2010) also tried more advance travel time functions to achieve better approximations of the travel times. The functions they tested were developed for the purpose of non-hyperbolic move out, and they indicate that their functions are also applicable for the purpose of time migration.

The tested functions in the present thesis works for prestack time migration. However, the tested functions with higher-order odd terms will lose their advantage when they are applied for the purpose of non hyperbolic move out. Travel time approximations for the purpose of a move out is not a function of aperture, but when it is done for the purpose of time migration it is.

8 References

Al-Dajani, A., and Tsvankin, I., 1998. *Nonhyperbolic moveout for horizontal transverse isotropy.* Geophysics, 63, 1738-1753.

Alkhalifah, T., and Lamer, K., 1994. *Migration error in transversely isotropic media*. Geophysics, 59, 1405-1418.

Alkhalifah, T., Tsvankin, I., 1995. *Velocity analysis of transversely isotropic media*. Geophysics, 60, 1550-1566.

Bancroft, J.C., Geiger, H.D., Margrave, G.F., 1998. *The equivalent offset method of prestack time migration*. Geophysics, 63, 2042-2053.

Black, J.L., Brzostowski, M.A., 1994. *Systematics of time-migration errors.* Geophysics, 59, 1419-1434

Bednar, J.B., 2005. *A brief history of seismic migration*. Geophysics, 70, 3MJ-20MJ.

Bottiglieri, M., Martino, S.D., Falanga, M., Godano, C., 2005. *Chaotic ray propagation in corrugated layers*. Nonlinear Processes in Geophysics, 12, 1003-1009.

Causse, E., 2004. *Approximations of reflection travel times with high accuracy at all offsets*. Journal of Geophysics and Engineering, 1, 28-45.

Virieux, J., 1996. *Seismic ray tracing in seismic modelling of earths structure.* Bologna: Editrice compositori.

Ewing, J., Ewing, M., 1959. *Seismic-refraction measurements in the Atlantic ocean basins, in the Mediterranean sea, on the Mid- Atlantic ridge, and in the Norwegian sea*. Bulletin of the geological society of America, 70, 291-318.

Fagin, S.W., 1991. *Seismic modeling of geologic structures: Applications to exploration problems*. Tulsa, Oklahoma: Society of Exploration Geophysicists (SEG).

Fehler, M.C., Huang, L., 2002. *Modern imaging using seismic reflection data*. Annu. Rev. Earth Planet. Sci, 30, 259-284.

Fomel, S., Stovas, A., 2010. *Generalized nonhyperbolic moveout approximation*. Geophysics, 75, U9-U18.

Fowler,P.J., 1997. *A comparative overview of prestack time migration methods*. SEG annual meeting expanded technical program abstracts with biographies, 16, 1571-1574.

Gazdag, J., Sguazzero, P., 1984. *Migration of Seismic Data*. Proceeding of the IEEE, 72, 1302-1315.

Gelius, L.J., Johansen, T.A., 2010. *Petroleum geophysics.* Bergen: Unigeo.

Gray, S.H., May, W.P., 1994. *Kirchhoff migration using eikonal equation traveltimes*. Geophysics, 59, 810-817.

Hellman, K.J., 2006. *Pre-stack time migration and velocity analysis methods with common scatter-point ghaters*. Journal of Geophysics and Engineering, 3, 283-289.

Hubral, P., 1977. *Time migration-Some ray theoretical aspects*. Geophysical Prospecting, 25, 738-745.

Iversen, E., Tygel, M., 2008. *Image-ray tracing for joint 3D seismic velocity estimation and time-to-depth conversion*. Geophysics, 73, S99-S114.

Keydar, S., Mikenberg, M., 2010. *Prestack time migration using the Kirchhoff sum along a new approximation of the reflection travel time curve.* Barcelona: Presented at the 72nd EAGE Conference Exhibition incorporating SPE EUROPEC 2010.

Khare, V., 1991. *New ray-theoretic interpretation of time migration.* SEG annual meeting expanded technical program abstracts with biographies, 61, 1492-1496.

Larner, K., Cohen, J.K., 1993. *Migration error in transversely isotropic media with linear velocity variation in depth*. Geophysics, 58, 1454-1467.

Mari, J.L., Glangeaud, F., Coppens, F., 1999. *Signal processing for geologists and geophysicists.* Paris: Éditions technip.

Mavko, G., Mukerji, T., Dvorkin, J., 2009. *The rock physics handbook: Tools for seismic analysis of porous media*. 2nd ed: Cambridge University Press.

Mjelde, R., Digranes, P., Shimamura, H., Shiobara, H., Kodaira, S., Brekke, H., Egebjerg, T., Sørenes, N., Thorbjørnsen, S., 1998. *Crustal structure of the northern part of the Vøring Basin, mid-Norway margin, from wide-angle seismic and gravity data*. Tectonophysics, 293, 175-205.

Robein, E., 2003. *Velocities, time-imaging and depth-imaging in reflection seismic: Principles and methods*. Houten: European association of Geoscientists & Engineers.

Rüger, A., 1997. *P-wave reflection coefficients for transversely isotropic models with vertical and horizontal axis of symmetry*. Geophysics, 62, 713-722.

Schneider, W.A., 1978. *Integral formulation for migration in two and three dimensions.* Geophysics, 43, 49-76.

Stein, S., Wysession, M., 2003. *An introduction to seismology, earthquakes, and earth structure*. Oxford: Blackwell.

Taylor, J.R., 1982. *An introduction to error analysis*: *The study of uncertainties in physical measurements.* 2nd ed. Sausalito, California: University of Science Books.

Taner M.T., Koehler F., 1969. *Velocity spectra-digital computer derivation and application of velocity function.* Geophysics, 34, 859-881.

Thomsen, L., 1986. *Weak elastic anisotropy*. Geophysics, 51, 1954-1966.

Yilmaz, O., 2001. *Seismic data analysis.* Tulsa, Oklahoma: Society of Exploration Geophysicists (SEG). (2vols).

Zhang, K., Cheng, J., Ma, Z., Zhang, W., 2006. *Pre-stack time migration and velocity analysis methods with common scatter-point gathers*. Journal of Geophysics and Engineering, 3, 283-289.

1 Appendix: Scanning technique

Below the MATLAB code based on the scanning technique described in *Chapter 4.2.1* is shown. The example below is for the High 3 function.

M-file

```
data0=load('Ascii_file');                                   Load data
data=data0;                                                 Model which is tested
array=data(:,1);                                            Length of array
one_w_time=data(:,2);                                       One way travel times

s=array;                                                    Shot array
r=array;                                                    Receiver array


for a=1:max(size(s));                                       Generate TWT surface
   for b=1:max(size(r));
        two_w_time(a,b)=one_w_time(a)+one_w_time(b);

   end
end

dmin_index=find(one_w_time==min(one_w_time));               M-point in Figure 3.1.
MM=data(dmin_index);


vM_min= minimum velocity;                                   Specify scanning interval,
vM_max= maximum velocity;                                   and spacing of coefficients
vM_step=spacing;
vM=vM_min:vM_step:vM_max;

t_min= minimum TWT;
t_max= maximum TWT;
t_step= spacing;
t=t_min:t_step:t_max;

c_3min= minimum;
c_3max= maximum;
c_3step=spacing;
c_3=c_3min:c_3step:c_3max;
```

```
res_min = 9999;                                          Perform approximation


for m=1:max(size(vM));
   for p=1:max(size(t));
      for q=1:max(size(c_3));
                    res=0;
             for n=1:max(size(s));
                for o=1:max(size(r));

time(m,p,q,n,o)=sqrt(((t(p)/2)^2)+((s(n)MM)^2)/(vM(m)^2)+((c_3(q))*(s(n)-MM)^3))+
                     sqrt(((t(p)/2)^2)+((r(o)-MM)^2)/(vM(m)^2)+((c_3(q))*(r(o)-MM)^3));
              res=res+(two_w_depth(n,o)-time(m,p,q,n,o))^2;
               end
             end
                if res < res_min
                res_min=res;
                min_vM=m;
                min_t=p;
                min_c3=q;
         end
      end
   end
end

res_min;                                                 Residual
num = max(size(s))^2;                                    Number of measurements
rms_min = sqrt(res_min/num)                              RMS error in s

min_vM;                                                  Position index on time,
min_t;                                                   velocity and c3 array
min_c3;

new_t=t(min_t)                                           TWT surface based on new
new_v=vM(min_vM)                                         values
new_c3=c_3(min_c3)


 for n=1:max(size(s));
       for o=1:max(size(r));
         time1(n,o)=sqrt(((new_t/2)^2)+(((s(n)-MM)^2)/new_v^2)+(new_c3*(s(n)-MM)^3))+
                        sqrt(((new_t/2)^2)+(((r(o)-MM)^2)/new_v^2)+(new_c3*(r(o)-MM)^3));
       end
     end
```

figure (1) *Plot approximated surface*

```
[x,y]=meshgrid(1:0.1:19, 1:0.1:19);
z=time1;
z(z==999)=nan;
surf(x,y,z);

cmin=4
cmax=7
caxis([cmin cmax])
xlim([1 19])
ylim([1 19])
zlim([3 8])
ylabel('Horizontal receiver coordinate r (km)')
xlabel( 'Horizontal source coordinate s (km)')
zlabel( 'Time (s)')
```

figure(2) *Plot synthetic surface*

```
[x,y]=meshgrid(1:0.1:19, 1:0.1:19);
z=two_w_depth;
surf(x,y,z)

cmin=4
cmax=7
caxis([cmin cmax])
xlim([1 19])
ylim([1 19])
zlim([3 8])
ylabel('Horizontal receiver coordinate r (km)')
xlabel( 'Horizontal source coordinate s (km)')
zlabel( 'Time (s)')
```

2 Appendix: Non linear least square surface fitting technique

Below the MATLAB code based on the non linear least square surface fitting technique described in *Chapter 4.2.2* is shown. The example below is for the High 6 function.

M-file

```
function F = myfun(x)

data=load('Ascii_file');                    Load model which is tested
array=data(:,1)                             Length of array
one_way_time=data(:,2);                     One way travel times

S1=array;
s=S1';                                      Shot array
R1=array;
r=R1';                                      Receiver array


k=0;
for a=1:max(size(s));                       Generate TWT

   for b=1:max(size(r));
      k=k+1;
      TDall(k)=one_w_time(a) + one_w_time(b);
      Sall(k)=s(a);
      Rall(k)=r(b);

    end
end

                                            Define function to minimize

F=abs(TDall-sqrt((x(1)^2)/4+x(2)*(Sall-10).^2 + x(3)*(Sall-10).^3 +x(4)*(Sall-10).^4 + x(5)*(Sall-10).^5 + x(6)*(Sall-10).^6) - sqrt((x(1)^2)/4+x(2)*(Rall-10).^2 +x(3)*(Rall-10).^3 + x(4)*(Rall-10).^4 + x(5)*(Rall-10).^5 + x(6)*(Rall-10).^6));
```

In command window

```
x0 = [0.3 0.4 0.0 0.0 0.0 0.0]              Select starting point

[x,resnorm] = lsqnonlin(@myfun,x0);         Invoke optimizer
```

3 Appendix

3.1 D-series

Below one see the test results obtained by the diffraction-time functions for D-series.

Velocity gradient (s^{-1})	DSR		
	T (s)	V (km/s)	RMS(s)
0.000	6.000	2.000	0.000
0.050	5.579	2.156	0.001
0.075	5.396	2.235	0.002
0.150	4.932	2.475	0.005
0.200	4.675	2.636	0.007
0.300	4.450	2.798	0.010
0.350	4.073	3.123	0.013
0.400	3.912	3.285	0.014
0.450	3.766	3.447	0.015
0.500	3.633	3.609	0.016

Velocity gradient (s^{-1})	High3			
	T (s)	V (km/s)	C3	RMS (s)
0.000	6.000	2.000	0.0000	0.000
0.050	5.579	2.156	0.0000	0.001
0.075	5.396	2.235	0.0000	0.002
0.150	4.932	2.475	0.0000	0.005
0.200	4.675	2.636	0.0000	0.007
0.300	4.450	2.798	0.0000	0.010
0.350	4.073	3.123	0.0000	0.013
0.400	3.912	3.285	0.0000	0.014
0.450	3.766	3.447	0.0000	0.015
0.500	3.633	3.609	0.0000	0.016

Velocity gradient (s^{-1})	High4				
	T (s)	V (km/s)	C3	C4	RMS (s)
0.000	6.000	2.000	0.0000	0.0000	0.000
0.050	5.578	2.153	0.0000	0.0000	0.000
0.075	5.394	2.229	0.0000	-0.0002	0.000
0.150	4.923	2.452	0.0000	0.0000	0.000
0.200	4.663	2.598	0.0000	-0.0001	0.000
0.300	4.435	2.743	0.0000	-0.0001	0.001
0.350	4.052	3.029	0.0000	-0.0001	0.006
0.400	3.889	3.171	0.0000	-0.0001	0.009
0.450	3.742	3.312	0.0000	-0.0001	0.014
0.500	3.608	3.452	0.0000	-0.0001	0.019

Velocity gradient (s^{-1})	High5					
	T (s)	V (km/s)	C3	C4	C5	RMS (s)
0.000	6.000	2.000	0.0000	0.0000	0.0000	0.000
0.050	5.578	2.153	0.0000	0.0000	0.0000	0.000
0.075	5.394	2.229	0.0000	0.0000	0.0000	0.000
0.150	4.923	2.452	0.0000	0.0000	0.0000	0.000
0.200	4.663	2.598	0.0000	-0.0001	0.0000	0.000
0.300	4.435	2.743	0.0000	-0.0001	0.0000	0.001
0.350	4.052	3.029	0.0000	-0.0001	0.0000	0.006
0.400	3.889	3.171	0.0000	-0.0001	0.0000	0.009
0.450	3.742	3.312	0.0000	-0.0001	0.0000	0.014
0.500	3.608	3.452	0.0000	-0.0001	0.0000	0.019

Velocity gradient (s^{-1})	High6						
	T (s)	V (km/s)	C3	C4	C5	C6	RMS (s)
0.000	6.000	2.000	0.0000	0.0000	0.0000	0.0000	0.000
0.050	5.578	2.153	0.0000	0.0000	0.0000	0.0000	0.000
0.075	5.393	2.229	0.0000	0.0000	0.0000	0.0000	0.000
0.150	4.923	2.451	0.0000	-0.0001	0.0000	0.0000	0.000
0.200	4.663	2.597	0.0000	-0.0001	0.0000	0.0000	0.000
0.300	4.435	2.740	0.0000	-0.0001	0.0000	0.0000	0.000
0.350	4.052	3.023	0.0000	-0.0001	0.0000	0.0000	0.000
0.400	3.889	3.163	0.0000	-0.0001	0.0000	0.0000	0.000
0.450	3.741	3.301	0.0000	-0.0001	0.0000	0.0000	0.000
0.500	3.606	3.438	0.0000	-0.0001	0.0000	0.0000	0.000

Velocity gradient (s^{-1})	Hellman				
	T (s)	V (km/s)	C4	C6	RMS (s)
0.000	6.000	2.000	0.0000	0.0000	0.000
0.050	5.578	2.153	0.0000	0.0000	0.000
0.075	5.394	2.229	0.0000	0.0000	0.000
0.150	4.923	2.451	-0.0001	0.0000	0.000
0.200	4.663	2.597	-0.0001	0.0000	0.000
0.300	4.435	2.740	-0.0001	0.0000	0.000
0.350	4.051	3.023	-0.0001	0.0000	0.000
0.400	3.889	3.163	-0.0001	0.0000	0.000
0.450	3.741	3.301	-0.0001	0.0000	0.000
0.500	3.606	3.438	-0.0001	0.0000	0.000

3.2 A-series

Below one see the test results obtained by the diffraction-time functions for all A-series.

3.2.1 A15-series

Velocity gradient (s^{-1})	DSR		
	T (s)	V (km/s)	RMS(s)
0.035	5.510	2.179	0.068
0.071	5.103	2.352	0.120
0.106	4.758	2.520	0.161
0.141	4.462	2.684	0.193
0.177	4.203	2.843	0.218
0.212	3.975	3.000	0.239
0.247	3.772	3.153	0.255
0.283	3.589	3.304	0.268
0.318	3.425	3.451	0.279

Velocity gradient (s^{-1})	High3			
	T (s)	V (km/s)	C3	RMS (s)
0.035	5.510	2.178	-0.0015	0.014
0.071	5.101	2.349	-0.0025	0.025
0.106	4.756	2.514	-0.0031	0.033
0.141	4.458	2.674	-0.0035	0.040
0.177	4.197	2.829	-0.0037	0.045
0.212	3.968	2.979	-0.0039	0.049
0.247	3.763	3.126	-0.0039	0.053
0.283	3.579	3.270	-0.0039	0.056
0.318	3.414	3.410	-0.0039	0.058

Velocity gradient (s^{-1})	High4				
	T (s)	V (km/s)	C3	C4	RMS (s)
0.035	5.510	2.179	-0.0015	0.0000	0.014
0.071	5.103	2.354	-0.0025	0.0000	0.025
0.106	4.759	2.526	-0.0031	0.0000	0.033
0.141	4.464	2.695	-0.0035	0.0000	0.040
0.177	4.206	2.862	-0.0037	0.0000	0.045
0.212	3.979	3.028	-0.0039	0.0001	0.049
0.247	3.777	3.192	-0.0039	0.0001	0.052
0.283	3.596	3.355	-0.0039	0.0001	0.055
0.318	3.433	3.517	-0.0039	0.0001	0.057

Velocity gradient (s^{-1})	High5					
	T (s)	V (km/s)	C3	C4	C5	RMS (s)
0.035	5.510	2.380	-0.0025	0.0000	0.0000	0.009
0.071	5.102	2.350	-0.0041	0.0000	0.0000	0.015
0.106	4.758	2.518	-0.0051	0.0000	0.0000	0.020
0.141	4.461	2.265	-0.0057	0.0000	0.0000	0.024
0.177	4.203	2.842	-0.0061	0.0000	0.0000	0.027
0.212	3.975	3.000	-0.0063	0.0000	0.0000	0.030
0.247	3.772	3.155	-0.0064	0.0000	0.0000	0.032
0.283	3.591	3.308	-0.0064	0.0000	0.0000	0.034
0.318	3.427	3.459	-0.0064	0.0000	0.0000	0.035

Velocity gradient (s^{-1})	High6						
	T (s)	V (km/s)	C3	C4	C5	C6	RMS (s)
0.035	5.510	2.179	-0.0025	0.0000	0.0000	0.0000	0.000
0.071	5.103	2.354	-0.0041	0.0000	0.0000	0.0000	0.015
0.106	4.759	2.525	-0.0051	0.0000	0.0000	0.0000	0.020
0.141	4.463	2.675	-0.0057	0.0001	0.0000	0.0000	0.024
0.177	4.205	2.862	-0.0061	0.0001	0.0000	0.0000	0.027
0.212	3.978	3.028	-0.0063	0.0001	0.0000	0.0000	0.030
0.247	3.776	3.192	-0.0064	0.0001	0.0000	0.0000	0.032
0.283	3.595	3.355	-0.0064	0.0001	0.0000	0.0000	0.034
0.318	3.432	3.517	-0.0064	0.0001	0.0000	0.0000	0.035

Velocity gradient (s^{-1})	Hellman				
	T (s)	V (km/s)	C4	C6	RMS (s)
0.035	5.510	2.179	0.0000	0.0000	0.068
0.071	5.103	2.351	0.0000	0.0000	0.120
0.106	4.759	2.521	0.0000	0.0000	0.161
0.141	4.463	2.689	0.0000	0.0000	0.193
0.177	4.205	2.852	0.0000	0.0000	0.218
0.212	3.978	3.014	0.0000	0.0000	0.239
0.247	3.776	3.172	0.0000	0.0000	0.255
0.283	3.594	3.329	0.0000	0.0000	0.268
0.318	3.431	3.485	0.0000	0.0000	0.279

3.2.2 A30-series

Velocity gradient (s^{-1})	DSR		
	T (s)	V (km/s)	RMS(s)
0.035	5.321	2.252	0.122
0.071	4.784	2.492	0.204
0.106	4.347	2.724	0.259
0.141	3.985	2.948	0.297
0.177	3.679	3.167	0.323
0.212	3.417	3.379	0.341
0.247	3.190	3.588	0.353
0.283	2.991	3.792	0.361
0.318	2.815	3.993	0.366

Velocity gradient (s^{-1})	High3			
	T (s)	V (km/s)	C3	RMS (s)
0.035	5.320	2.249	-0.0026	0.025
0.071	4.780	2.484	-0.0040	0.042
0.106	4.340	2.706	-0.0046	0.053
0.141	3.974	2.919	-0.0049	0.060
0.177	3.665	3.123	-0.0049	0.065
0.212	3.400	3.321	-0.0048	0.069
0.247	3.171	3.514	-0.0047	0.071
0.283	2.970	3.702	-0.0045	0.072
0.318	2.793	3.886	-0.0043	0.073

Velocity gradient (s^{-1})	High4				
	T (s)	V (km/s)	C3	C4	RMS (s)
0.035	5.322	2.256	-0.0026	0.0000	0.025
0.071	4.788	2.509	-0.0040	0.0000	0.041
0.106	4.355	2.759	-0.0046	0.0001	0.052
0.141	3.996	3.008	-0.0049	0.0001	0.059
0.177	3.694	3.257	-0.0049	0.0001	0.063
0.212	3.435	3.504	-0.0049	0.0001	0.065
0.247	3.210	3.751	-0.0047	0.0002	0.067
0.283	3.014	3.997	-0.0046	0.0002	0.067
0.318	2.841	4.242	-0.0044	0.0002	0.067

Velocity gradient (s^{-1})	High5					
	T (s)	V (km/s)	C3	C4	C5	RMS (s)
0.035	5.322	2.252	-0.0043	0.0000	0.0000	0.015
0.071	4.786	2.497	-0.0065	0.0000	0.0000	0.025
0.106	4.351	2.735	-0.0075	0.0000	0.0000	0.032
0.141	3.990	2.968	-0.0078	0.0001	0.0000	0.037
0.177	3.686	3.198	-0.0078	0.0001	0.0000	0.040
0.212	3.426	3.425	-0.0077	0.0001	0.0000	0.042
0.247	3.201	3.649	-0.0074	0.0001	0.0000	0.043
0.283	3.003	3.873	-0.0071	0.0001	0.0000	0.043
0.318	2.829	4.095	-0.0067	0.0001	0.0000	0.044

Velocity gradient (s^{-1})	High6						
	T (s)	V (km/s)	C3	C4	C5	C6	RMS (s)
0.035	5.322	2.255	-0.0043	0.0000	0.0000	0.0000	0.015
0.071	4.788	2.508	-0.0065	0.0001	0.0000	0.0000	0.025
0.106	4.354	2.759	-0.0075	0.0001	0.0000	0.0000	0.032
0.141	3.995	3.008	-0.0078	0.0002	0.0000	0.0000	0.036
0.177	3.692	3.257	-0.0079	0.0002	0.0000	0.0000	0.039
0.212	3.433	3.504	-0.0077	0.0002	0.0000	0.0000	0.041
0.247	3.209	3.751	-0.0074	0.0002	0.0000	0.0000	0.043
0.283	3.012	3.997	-0.0071	0.0003	0.0000	0.0000	0.043
0.318	2.839	4.242	-0.0068	0.0000	0.0000	0.0000	0.043

Velocity gradient (s^{-1})	Hellman				
	T (s)	V (km/s)	C4	C6	RMS (s)
0.035	5.322	2.253	0.0000	0.0000	0.122
0.071	4.787	2.501	0.0000	0.0000	0.204
0.106	4.353	2.745	0.0000	0.0000	0.259
0.141	3.994	2.986	0.0000	0.0000	0.297
0.177	3.691	3.222	0.0001	0.0000	0.323
0.212	3.431	3.459	0.0001	0.0000	0.341
0.247	3.207	3.692	0.0001	0.0000	0.353
0.283	3.010	3.918	0.0001	0.0000	0.361
0.318	2.836	4.147	0.0001	0.0000	0.366

3.2.3 A45-series

Velocity gradient (s^{-1})	DSR		
	T (s)	V (km/s)	RMS(s)
0.035	5.183	2.306	0.164
0.071	4.561	2.595	0.260
0.106	4.071	2.872	0.319
0.141	3.676	3.139	0.356
0.177	3.350	3.397	0.378
0.212	3.076	3.650	0.391
0.247	2.843	3.897	0.397
0.283	2.643	4.141	0.400
0.318	2.468	4.380	0.399

Velocity gradient (s^{-1})	High3			
	T (s)	V (km/s)	C3	RMS (s)
0.035	5.181	2.302	-0.0034	0.033
0.071	4.554	2.580	-0.0049	0.053
0.106	4.059	2.840	-0.0054	0.065
0.141	3.659	3.088	-0.0054	0.071
0.177	3.329	3.326	-0.0053	0.075
0.212	3.053	3.556	-0.0051	0.078
0.247	2.817	3.781	-0.0048	0.078
0.283	2.615	4.000	-0.0045	0.079
0.318	2.439	4.216	-0.0043	0.078

Velocity gradient (s^{-1})	High4				
	T (s)	V (km/s)	C3	C4	RMS (s)
0.035	5.186	2.315	-0.0035	0.0000	0.033
0.071	4.569	2.629	-0.0049	0.0001	0.052
0.106	4.085	2.941	-0.0054	0.0001	0.081
0.141	3.695	3.253	-0.0055	0.0002	0.068
0.177	3.374	3.565	-0.0053	0.0002	0.070
0.212	3.104	3.876	-0.0051	0.0002	0.070
0.247	2.875	4.187	-0.0049	0.0002	0.070
0.283	2.677	4.497	-0.0046	0.0002	0.068
0.318	2.505	4.808	-0.0043	0.0002	0.066

Velocity gradient (s^{-1})	High5					
	T (s)	V (km/s)	C3	C4	C5	RMS (s)
0.035	5.185	2.309	-0.0056	0.0000	0.0000	0.020
0.071	4.565	2.607	-0.0079	0.0000	0.0000	0.032
0.106	4.078	2.898	-0.0086	0.0001	0.0001	0.039
0.141	3.686	3.184	-0.0086	0.0001	0.0001	0.043
0.177	3.363	3.468	-0.0083	0.0001	0.0000	0.045
0.212	3.093	3.749	-0.0078	0.0001	0.0000	0.046
0.247	2.862	4.030	-0.0073	0.0001	0.0000	0.047
0.283	2.664	4.311	-0.0068	0.0001	0.0000	0.047
0.318	2.492	4.592	-0.0063	0.0001	0.0000	0.046

Velocity gradient (s^{-1})	High6						
	T (s)	V (km/s)	C3	C4	C5	C6	RMS (s)
0.035	5.186	2.315	-0.0056	0.0001	0.0000	0.0000	0.020
0.071	4.568	2.629	-0.0079	0.0001	0.0000	0.0000	0.032
0.106	4.084	2.941	-0.0086	0.0002	0.0001	0.0000	0.039
0.141	3.693	3.253	-0.0086	0.0003	0.0001	0.0000	0.043
0.177	3.372	3.565	-0.0083	0.0003	0.0000	0.0000	0.045
0.212	3.102	3.876	-0.0078	0.0003	0.0000	0.0000	0.046
0.247	2.872	4.187	-0.0073	0.0003	0.0000	0.0000	0.046
0.283	2.675	4.498	-0.0068	0.0003	0.0000	0.0000	0.046
0.318	2.503	4.808	-0.0063	0.0003	0.0000	0.0000	0.046

Velocity gradient (s^{-1})	Hellman				
	T (s)	V (km/s)	C4	C6	RMS (s)
0.035	5.185	2.311	0.0000	0.0000	0.164
0.071	4.567	2.616	0.0000	0.0000	0.260
0.106	4.083	2.915	0.0001	0.0000	0.319
0.141	3.692	3.214	0.0001	0.0000	0.356
0.177	3.369	3.503	0.0001	0.0000	0.378
0.212	3.100	3.797	0.0001	0.0000	0.390
0.247	2.869	4.078	0.0001	0.0000	0.397
0.283	2.671	4.363	0.0001	0.0000	0.399
0.318	2.499	4.653	0.0001	0.0000	0.399

3.2.4 A60-series

Velocity gradient (s^{-1})	DSR		
	T (s)	V (km/s)	RMS(s)
0.035	5.099	2.339	0.193
0.071	4.428	2.657	0.298
0.106	3.910	2.959	0.358
0.141	3.499	3.250	0.392
0.177	3.165	3.533	0.410
0.212	2.888	3.809	0.419
0.247	2.655	4.080	0.421
0.283	2.456	4.347	0.420
0.318	2.284	4.610	0.416

Velocity gradient (s^{-1})	High3			
	T (s)	V (km/s)	C3	RMS (s)
0.035	5.095	2.333	-0.0040	0.039
0.071	4.418	2.635	-0.0054	0.060
0.106	3.894	2.916	-0.0058	0.072
0.141	3.478	3.183	-0.0057	0.078
0.177	3.140	3.439	-0.0055	0.081
0.212	2.860	3.689	-0.0052	0.082
0.247	2.624	3.932	-0.0048	0.082
0.283	2.423	4.171	-0.0045	0.082
0.318	2.250	4.406	-0.0042	0.081

Velocity gradient (s^{-1})	High4				
	T (s)	V (km/s)	C3	C4	RMS (s)
0.035	5.103	2.353	-0.0040	0.0000	0.039
0.071	4.439	2.705	-0.0054	0.0001	0.059
0.106	3.929	3.058	-0.0058	0.0002	0.068
0.141	3.525	3.411	-0.0058	0.0002	0.072
0.177	3.196	3.764	-0.0056	0.0002	0.073
0.212	2.923	4.116	-0.0052	0.0002	0.072
0.247	2.693	4.469	-0.0049	0.0002	0.070
0.283	2.497	4.822	-0.0046	0.0002	0.067
0.318	2.328	5.175	-0.0043	0.0002	0.065

Velocity gradient (s^{-1})	High5					
	T (s)	V (km/s)	C3	C4	C5	RMS (s)
0.035	5.101	2.344	-0.0065	0.0000	0.0000	0.024
0.071	4.434	2.675	-0.0087	0.0001	0.0001	0.037
0.106	3.921	3.000	-0.0092	0.0001	0.0001	0.044
0.141	3.514	3.320	-0.0089	0.0001	0.0001	0.047
0.177	3.183	3.638	-0.0084	0.0001	0.0000	0.049
0.212	2.910	3.957	-0.0078	0.0001	0.0000	0.049
0.247	2.680	4.275	-0.0071	0.0001	0.0000	0.049
0.283	2.483	4.595	-0.0065	0.0002	0.0003	0.048
0.318	2.314	4.917	-0.0060	0.0002	0.0000	0.047

Velocity gradient (s^{-1})	High6						
	T (s)	V (km/s)	C3	C4	C5	C6	RMS (s)
0.035	5.102	2.353	-0.0065	0.0001	0.0000	0.0000	0.024
0.071	4.438	2.705	-0.0087	0.0002	0.0001	0.0000	0.037
0.106	3.928	3.058	-0.0092	0.0003	0.0001	0.0000	0.043
0.141	3.522	3.411	-0.0090	0.0003	0.0001	0.0000	0.047
0.177	3.193	3.764	-0.0085	0.0003	0.0000	0.0000	0.048
0.212	2.920	4.116	-0.0078	0.0003	0.0000	0.0000	0.048
0.247	2.691	4.468	-0.0072	0.0003	0.0000	0.0000	0.048
0.283	2.494	4.821	-0.0060	0.0003	0.0000	0.0000	0.047
0.318	2.325	5.174	-0.0060	0.0003	0.0000	0.0000	0.046

Velocity gradient (s^{-1})	Hellman				
	T (s)	V (km/s)	C4	C6	RMS (s)
0.035	5.102	2.347	0.0000	0.0000	0.193
0.071	4.437	2.686	0.0000	0.0000	0.298
0.106	3.926	3.025	0.0001	0.0000	0.358
0.141	3.520	3.356	0.0001	0.0000	0.391
0.177	3.191	3.680	0.0001	0.0000	0.410
0.212	2.917	4.006	0.0001	0.0000	0.418
0.247	2.687	4.330	0.0001	0.0000	0.421
0.283	2.491	4.652	0.0001	0.0000	0.419
0.318	2.321	4.973	0.0001	0.0000	0.415

3.2.5 A75-series

Velocity gradient (s^{-1})	DSR		
	T (s)	V (km/s)	RMS(s)
0.035	5.069	2.350	0.211
0.071	4.380	2.675	0.322
0.106	3.853	2.984	0.383
0.141	3.436	3.281	0.415
0.177	3.099	3.570	0.432
0.212	2.821	3.853	0.438
0.247	2.588	4.130	0.439
0.283	2.389	4.405	0.435
0.318	2.218	4.675	0.430

Velocity gradient (s^{-1})	High3			
	T (s)	V (km/s)	C3	RMS (s)
0.035	5.065	2.342	-0.0044	0.043
0.071	4.369	2.649	-0.0058	0.065
0.106	3.835	2.933	-0.0061	0.076
0.141	3.412	3.204	-0.0060	0.082
0.177	3.071	3.464	-0.0057	0.085
0.212	2.790	3.717	-0.0053	0.086
0.247	2.554	3.965	-0.0049	0.086
0.283	2.354	4.210	-0.0046	0.085
0.318	2.182	4.451	-0.0042	0.084

Velocity gradient (s^{-1})	High4				
	T (s)	V (km/s)	C3	C4	RMS (s)
0.035	5.074	2.366	-0.0044	0.0001	0.043
0.071	4.394	2.733	-0.0058	0.0001	0.063
0.106	3.875	3.101	-0.0062	0.0002	0.072
0.141	3.465	3.470	-0.0061	0.0002	0.075
0.177	3.134	3.838	-0.0058	0.0002	0.075
0.212	2.860	4.207	-0.0054	0.0003	0.073
0.247	2.631	4.576	-0.0050	0.0003	0.071
0.283	2.435	4.946	-0.0047	0.0002	0.067
0.318	2.266	5.315	-0.0043	0.0002	0.064

Velocity gradient (s^{-1})	High5					
	T (s)	V (km/s)	C3	C4	C5	RMS (s)
0.035	5.072	2.356	-0.0071	0.0000	0.0000	0.026
0.071	4.388	2.698	-0.0093	0.0001	0.0001	0.040
0.106	3.865	3.033	-0.0097	0.0001	0.0001	0.046
0.141	3.453	3.366	-0.0093	0.0001	0.0001	0.049
0.177	3.121	3.697	-0.0086	0.0002	0.0000	0.051
0.212	2.846	4.030	-0.0079	0.0002	0.0000	0.051
0.247	2.617	4.364	-0.0072	0.0002	0.0000	0.050
0.283	2.421	4.700	-0.0065	0.0002	0.0000	0.049
0.318	2.253	5.039	-0.0059	0.0002	0.0000	0.048

Velocity gradient (s^{-1})	High6						
	T (s)	V (km/s)	C3	C4	C5	C6	RMS (s)
0.035	5.074	2.366	-0.0071	0.0001	0.0000	0.0000	0.026
0.071	4.393	2.733	-0.0093	0.0002	0.0001	0.0000	0.039
0.106	3.873	3.101	-0.0097	0.0003	0.0001	0.0000	0.046
0.141	3.463	3.469	-0.0093	0.0003	0.0001	0.0000	0.049
0.177	3.131	3.838	-0.0087	0.0004	0.0000	0.0000	0.050
0.212	2.858	4.206	-0.0080	0.0004	0.0000	0.0000	0.050
0.247	2.628	4.575	-0.0073	0.0004	0.0000	0.0000	0.050
0.283	2.432	4.945	-0.0066	0.0003	0.0000	0.0000	0.049
0.318	2.264	5.313	-0.0060	0.0003	0.0000	0.0000	0.047

Velocity gradient (s^{-1})	Hellman				
	T (s)	V (km/s)	C4	C6	RMS (s)
0.035	5.073	2.361	0.0000	0.0000	0.211
0.071	4.391	2.712	0.0001	0.0000	0.322
0.106	3.871	3.059	0.0001	0.0000	0.382
0.141	3.461	3.405	0.0001	0.0000	0.415
0.177	3.128	3.742	0.0001	0.0000	0.431
0.212	2.855	4.085	0.0001	0.0000	0.438
0.247	2.625	4.417	0.0001	0.0000	0.438
0.283	2.429	4.752	0.0001	0.0000	0.435
0.318	2.260	5.086	0.0001	0.0000	0.429

3.3 G-series

Below one see the test results obtained by the diffraction-time functions for G-series.

Velocity gradient (s^{-1})	DSR		
	T (s)	V (km/s)	RMS(s)
0.025	2.009	5.736	0.032
0.050	1.927	5.976	0.050
0.075	1.852	6.211	0.066
0.100	1.782	6.442	0.081
0.125	1.717	6.669	0.093
0.150	1.657	6.891	0.104
0.175	1.600	7.111	0.113
0.200	1.547	7.327	0.121
0.225	1.498	7.541	0.128
0.250	1.451	7.752	0.134

Velocity gradient (s^{-1})	High3			
	T (s)	V (km/s)	C3	RMS (s)
0.025	2.009	5.735	-0.0002	0.021
0.050	1.926	5.969	-0.0004	0.020
0.075	1.851	6.198	-0.0005	0.021
0.100	1.780	6.420	-0.0006	0.021
0.125	1.715	6.635	-0.0007	0.022
0.150	1.654	6.846	-0.0007	0.023
0.175	1.597	7.051	-0.0008	0.024
0.200	1.543	7.253	-0.0008	0.025
0.225	1.493	7.450	-0.0008	0.026
0.250	1.445	7.644	-0.0008	0.026

Velocity gradient (s^{-1})	High4				
	T (s)	V (km/s)	C3	C4	RMS (s)
0.025	1.996	5.549	-0.0002	0.0000	0.019
0.050	1.915	5.796	-0.0004	0.0000	0.019
0.075	1.842	6.047	-0.0005	0.0000	0.020
0.100	1.774	6.298	-0.0006	0.0000	0.021
0.125	1.711	6.550	-0.0007	0.0000	0.022
0.150	1.652	6.802	-0.0007	0.0000	0.023
0.175	1.597	7.055	-0.0008	0.0000	0.024
0.200	1.545	7.307	-0.0008	0.0000	0.025
0.225	1.497	7.561	-0.0008	0.0000	0.026
0.250	1.452	7.815	-0.0008	0.0000	0.026

Velocity gradient (s^{-1})	High5					
	T (s)	V (km/s)	C3	C4	C5	RMS (s)
0.025	1.995	5.548	-0.0003	0.0000	0.0000	0.018
0.050	1.915	5.789	-0.0006	0.0000	0.0000	0.018
0.075	1.841	6.031	-0.0008	0.0000	0.0000	0.017
0.100	1.773	6.272	-0.0009	0.0000	0.0000	0.017
0.125	1.709	6.510	-0.0011	0.0000	0.0000	0.017
0.150	1.650	6.747	-0.0011	0.0000	0.0000	0.017
0.175	1.595	6.983	-0.0012	0.0000	0.0000	0.017
0.200	1.543	7.217	-0.0012	0.0000	0.0000	0.018
0.225	1.494	7.451	-0.0013	0.0000	0.0000	0.018
0.250	1.449	7.684	-0.0013	0.0000	0.0000	0.018

Velocity gradient (s^{-1})	High6						
	T (s)	V (km/s)	C3	C4	C5	C6	RMS (s)
0.025	1.972	5.019	-0.0003	-0.0003	0.0000	0.0000	0.012
0.050	1.894	5.253	-0.0006	-0.0003	0.0004	0.0000	0.012
0.075	1.822	5.497	-0.0008	-0.0002	0.0000	0.0000	0.012
0.100	1.755	5.741	-0.0009	-0.0002	0.0000	0.0000	0.013
0.125	1.693	5.986	-0.0010	-0.0002	0.0000	0.0000	0.014
0.150	1.635	6.233	-0.0011	-0.0002	0.0000	0.0000	0.015
0.175	1.581	6.479	-0.0012	-0.0001	0.0000	0.0000	0.015
0.200	1.531	6.725	-0.0012	-0.0001	0.0000	0.0000	0.016
0.225	1.483	6.973	-0.0012	-0.0001	0.0000	0.0000	0.016
0.250	1.439	7.221	-0.0013	-0.0001	0.0000	0.0000	0.017

Velocity gradient (s^{-1})	Hellman				
	T (s)	V (km/s)	C4	C6	RMS (s)
0.025	1.972	5.019	-0.0003	0.0000	0.027
0.050	1.894	5.250	-0.0003	0.0000	0.047
0.075	1.822	5.492	-0.0003	0.0000	0.065
0.100	1.755	5.731	-0.0002	0.0000	0.080
0.125	1.693	5.968	-0.0002	0.0000	0.092
0.150	1.635	6.208	-0.0002	0.0000	0.103
0.175	1.581	6.444	-0.0002	0.0000	0.113
0.200	1.530	6.682	-0.0001	0.0000	0.121
0.225	1.483	6.920	-0.0001	0.0000	0.128
0.250	1.438	7.155	-0.0001	0.0000	0.134

3.4 P-series

Below one see the test results obtained by the diffraction-time functions for the two P-series.

3.4.1 P1-series

Period (Km)	DSR		
	T (s)	V (km/s)	RMS(s)
1.50	5.945	1.983	0.031
2.00	5.934	1.981	0.038
2.50	5.926	1.978	0.044
3.00	5.915	1.973	0.047
3.50	5.911	1.975	0.052
4.00	5.901	1.971	0.055
4.50	5.888	1.964	0.055
5.00	5.877	1.963	0.058
5.50	5.874	1.966	0.062
6.00	5.871	1.968	0.064
6.50	5.863	1.966	0.066
7.00	5.849	1.960	0.066

Period (Km)	High3			
	T (s)	V (km/s)	C3	RMS (s)
1.50	5.945	1.983	0.0000	0.031
2.00	5.934	1.981	0.0000	0.038
2.50	5.926	1.978	0.0000	0.044
3.00	5.915	1.973	0.0000	0.047
3.50	5.911	1.975	0.0000	0.052
4.00	5.901	1.971	0.0000	0.055
4.50	5.888	1.964	0.0000	0.055
5.00	5.877	1.963	0.0000	0.058
5.50	5.874	1.966	0.0000	0.062
6.00	5.871	1.968	0.0000	0.064
6.50	5.863	1.966	0.0000	0.066
7.00	5.849	1.960	0.0000	0.066

Period (Km)	High4 T (s)	V (km/s)	C3	C4	RMS (s)
1.50	5.924	1.946	0.0000	-0.0002	0.028
2.00	5.906	1.932	0.0000	-0.0002	0.034
2.50	5.892	1.924	0.0000	-0.0002	0.039
3.00	5.885	1.923	0.0000	-0.0002	0.044
3.50	5.869	1.906	0.0000	-0.0003	0.045
4.00	5.854	1.893	0.0000	-0.0003	0.047
4.50	5.851	1.902	0.0000	-0.0003	0.050
5.00	5.839	1.898	0.0000	-0.0003	0.053
5.50	5.820	1.877	0.0000	-0.0004	0.051
6.00	5.797	1.850	0.0000	-0.0005	0.045
6.50	5.773	1.826	0.0000	-0.0006	0.036
7.00	5.751	1.809	0.0000	-0.0007	0.026

Period (Km)	High5 T (s)	V (km/s)	C3	C4	C5	RMS (s)
1.50	5.9237	1.9454	0.0000	-0.0002	0.0000	0.028
2.00	5.9062	1.9318	0.0000	-0.0002	0.0000	0.034
2.50	5.8942	1.9241	0.0000	-0.0002	0.0000	0.039
3.00	5.8851	1.9227	0.0000	-0.0002	0.0000	0.044
3.50	5.8694	1.9055	0.0000	-0.0003	0.0000	0.045
4.00	5.8537	1.8927	0.0000	-0.0003	0.0000	0.047
4.50	5.8511	1.9024	0.0000	-0.0003	0.0000	0.050
5.00	5.8385	1.8983	0.0000	-0.0003	0.0000	0.053
5.50	5.8195	1.8772	0.0000	-0.0004	0.0000	0.051
6.00	5.7971	1.8500	0.0000	-0.0005	0.0000	0.045
6.50	5.7725	1.8255	0.0000	-0.0006	0.0000	0.036
7.00	5.7512	1.8094	0.0000	-0.0007	0.0000	0.026

Period (Km)	High6 T (s)	V (km/s)	C3	C4	C5	C6	RMS (s)
1.50	5.904	1.881	0.0000	-0.0009	0.0000	0.0000	0.025
2.00	5.885	1.864	0.0000	-0.0010	0.0000	0.0000	0.031
2.50	5.868	1.842	0.0000	-0.0012	0.0000	0.0000	0.035
3.00	5.852	1.821	0.0000	-0.0015	0.0000	0.0000	0.038
3.50	5.834	1.801	0.0000	-0.0016	0.0000	0.0000	0.040
4.00	5.825	1.810	0.0000	-0.0014	0.0000	0.0000	0.043
4.50	5.806	1.775	0.0000	-0.0019	0.0000	0.0000	0.041
5.00	5.806	1.719	0.0000	-0.0027	0.0000	0.0000	0.033
5.50	5.744	1.684	0.0000	-0.0032	0.0000	0.0000	0.021
6.00	5.728	1.677	0.0000	-0.0031	0.0000	0.0000	0.012
6.50	5.716	1.685	0.0000	-0.0027	0.0000	0.0000	0.006
7.00	5.709	1.705	0.0000	-0.0023	0.0000	0.0000	0.004

Period (Km)	Hellman T (s)	V (km/s)	C4	C6	RMS (s)
1.50	5.904	1.881	-0.0009	0.0000	0.025
2.00	5.885	1.864	-0.0010	0.0000	0.031
2.50	5.868	1.842	-0.0012	0.0000	0.035
3.00	5.852	1.821	-0.0015	0.0000	0.038
3.50	5.834	1.801	-0.0016	0.0000	0.040
4.00	5.825	1.810	-0.0014	0.0000	0.043
4.50	5.806	1.775	-0.0019	0.0000	0.041
5.00	5.772	1.719	-0.0027	0.0000	0.033
5.50	5.744	1.684	-0.0032	0.0000	0.021
6.00	5.728	1.677	-0.0031	0.0000	0.012
6.50	5.716	1.685	-0.0028	0.0000	0.006
7.00	5.709	1.705	-0.0023	0.0000	0.004

3.4.2 P2-series

Period (Km)	DSR		
	T (s)	V (km/s)	RMS(s)
1.50	5.957	1.985	0.027
2.00	6.018	2.027	0.047
2.50	5.957	1.986	0.049
3.00	5.915	1.973	0.047
3.50	5.937	1.982	0.059
4.00	5.984	1.994	0.069
4.50	6.039	2.011	0.073
5.00	6.084	2.024	0.071
5.50	6.109	2.027	0.069
6.00	6.122	2.027	0.070
6.50	6.129	2.029	0.074
7.00	6.133	2.034	0.078

Period (Km)	High3			
	T (s)	V (km/s)	C3	RMS (s)
1.50	5.957	1.985	0.0000	0.027
2.00	6.018	2.003	0.0000	0.047
2.50	5.957	1.986	0.0003	0.047
3.00	5.915	1.973	0.0000	0.047
3.50	5.937	1.981	-0.0004	0.057
4.00	5.984	1.993	-0.0004	0.067
4.50	6.039	2.011	-0.0005	0.071
5.00	6.083	2.024	-0.0005	0.069
5.50	6.109	2.027	-0.0003	0.068
6.00	6.122	2.027	0.0000	0.070
6.50	6.129	2.029	0.0002	0.073
7.00	6.133	2.034	0.0003	0.077

Period (Km)	High4 T (s)	V (km/s)	C3	C4	RMS (s)
1.50	5.940	1.955	0.0000	-0.0001	0.024
2.00	6.031	2.030	0.0000	0.0001	0.046
2.50	5.941	1.957	0.0003	-0.0001	0.046
3.00	5.885	1.928	0.0000	-0.0002	0.044
3.50	5.908	1.932	-0.0004	-0.0002	0.054
4.00	5.979	1.985	-0.0004	0.0000	0.067
4.50	6.054	2.041	-0.0005	0.0001	0.070
5.00	6.114	2.085	-0.0005	0.0002	0.066
5.50	6.162	2.141	-0.0003	0.0004	0.060
6.00	6.198	2.199	0.0000	0.0006	0.051
6.50	6.220	2.239	0.0002	0.0007	0.046
7.00	6.225	2.247	0.0003	0.0007	0.051

Period (Km)	High5 T (s)	V (km/s)	C3	C4	C5	RMS (s)
1.50	5.940	1.955	0.0000	-0.0001	0.0000	0.024
2.00	6.031	2.030	0.0000	0.0001	0.0000	0.046
2.50	5.941	1.957	0.0010	-0.0001	0.0000	0.046
3.00	5.885	1.923	0.0000	-0.0002	0.0000	0.044
3.50	5.908	1.932	-0.0011	-0.0002	0.0000	0.054
4.00	5.979	1.985	-0.0023	0.0000	0.0000	0.064
4.50	6.054	2.040	-0.0024	0.0001	0.0000	0.067
5.00	6.114	2.085	-0.0014	0.0002	0.0000	0.065
5.50	6.162	2.141	-0.0005	0.0004	0.0000	0.059
6.00	6.198	2.199	0.0000	0.0006	0.0000	0.051
6.50	6.220	2.238	0.0006	0.0007	0.0000	0.046
7.00	6.225	2.247	0.0015	0.0007	0.0000	0.049

Period (Km)	High6						
	T (s)	V (km/s)	C3	C4	C5	C6	RMS (s)
1.50	5.924	1.900	0.0000	-0.0007	0.0000	0.0000	0.022
2.00	6.042	2.082	0.0000	0.0006	0.0000	0.0000	0.045
2.50	5.927	1.912	0.0010	-0.0006	0.0000	0.0000	0.045
3.00	5.852	1.821	0.0000	-0.0015	0.0000	0.0000	0.038
3.50	5.884	1.855	-0.0011	-0.0011	0.0000	0.0000	0.052
4.00	5.976	1.972	-0.0023	-0.0002	0.0000	0.0000	0.064
4.50	6.075	2.130	-0.0024	0.0009	0.0000	0.0000	0.066
5.00	6.169	2.373	-0.0014	0.0023	0.0000	0.0000	0.055
5.50	6.238	2.618	-0.0006	0.0033	0.0000	0.0000	0.035
6.00	6.275	2.726	0.0000	0.0035	0.0000	0.0000	0.017
6.50	6.282	2.667	0.0006	0.0030	0.0000	0.0000	0.024
7.00	6.269	2.528	0.0015	0.0023	0.0000	0.0000	0.040

Period (Km)	Hellman				
	T (s)	V (km/s)	C4	C6	RMS (s)
1.50	5.924	1.900	-0.0007	0.0000	0.022
2.00	6.042	2.082	0.0006	0.0000	0.045
2.50	5.927	1.912	-0.0006	0.0000	0.047
3.00	5.852	1.821	-0.0015	0.0000	0.038
3.50	5.884	1.855	-0.0011	0.0000	0.054
4.00	5.976	1.972	-0.0002	0.0000	0.069
4.50	6.075	2.130	0.0009	0.0000	0.071
5.00	6.169	2.373	0.0023	0.0000	0.059
5.50	6.238	2.618	0.0033	0.0000	0.037
6.00	6.275	2.726	0.0035	0.0000	0.017
6.50	6.282	2.667	0.0030	0.0000	0.025
7.00	6.269	2.528	0.0023	0.0000	0.044

3.5 K-series

Below one see the test results obtained by the diffraction-time functions for K-series.

	DSR		
	T (s)	V (km/s)	RMS(s)
K1	2.566	4.534	0.133
K2	2.509	4.466	0.110
K3	2.601	4.590	0.105
K4	2.550	4.509	0.123
K5	2.622	4.616	0.125
K6	2.607	4.565	0.120

	High3			
	T (s)	V (km/s)	C3	RMS (s)
K1	2.563	4.516	-0.0012	0.073
K2	2.508	4.454	0.0011	0.049
K3	2.600	4.581	-0.0010	0.053
K4	2.547	4.493	-0.0012	0.052
K5	2.621	4.603	-0.0011	0.068
K6	2.605	4.552	-0.0011	0.051

	High4				
	T (s)	V (km/s)	C3	C4	RMS (s)
K1	2.557	4.461	-0.0012	0.0000	0.073
K2	2.474	4.189	-0.0011	-0.0001	0.044
K3	2.610	4.688	-0.0010	0.0000	0.052
K4	2.536	4.391	-0.0012	0.0000	0.052
K5	2.638	4.847	-0.0011	0.0001	0.066
K6	2.611	4.623	-0.0011	-0.0011	0.051

	High5					
	T (s)	V (km/s)	C3	C4	C5	RMS (s)
K1	2.554	4.424	-0.0026	0.0000	0.0000	0.065
K2	2.473	4.176	-0.0018	-0.0001	0.0000	0.041
K3	2.609	4.682	-0.0012	0.0000	0.0000	0.052
K4	2.534	4.368	-0.0021	0.0000	0.0000	0.047
K5	2.637	4.830	-0.0017	0.0001	0.0000	0.064
K6	2.610	4.603	-0.0019	0.0000	0.0000	0.048

	High6						
	T (s)	V (km/s)	C3	C4	C5	C6	RMS (s)
K1	2.548	4.323	-0.0026	-0.0001	0.0000	0.0000	0.064
K2	2.443	3.807	-0.0017	-0.0006	0.0000	0.0000	0.037
K3	2.621	4.970	-0.0012	0.0002	0.0000	0.0000	0.051
K4	2.521	4.165	-0.0021	-0.0003	0.0000	0.0000	0.046
K5	2.650	5.301	-0.0017	0.0004	0.0000	0.0000	0.062
K6	2.615	4.751	-0.0019	0.0001	0.0000	0.0000	0.046

	Hellman				
	T (s)	V (km/s)	C4	C6	RMS (s)
K1	2.548	4.307	-0.0002	0.0000	0.133
K2	2.443	3.799	-0.0006	0.0000	0.106
K3	2.621	4.960	0.0002	0.0000	0.104
K4	2.521	4.149	-0.0003	0.0000	0.122
K5	2.650	5.290	0.0004	0.0000	0.124
K6	2.615	4.739	0.0001	0.0000	0.120

4 Appendix

4.1 VTI-series

Below one see the test results obtained by the diffraction-time functions for VTI-series.

	DSR		
	T (s)	V (km/s)	RMS(s)
VTI1	4.242	3.478	0.006
VTI2	4.262	3.381	0.015
VTI3	4.287	3.278	0.026
VTI4	4.320	3.170	0.039
VTI5	4.366	3.053	0.055

	High3			
	T (s)	V (km/s)	C3	RMS (s)
VTI1	4.242	3.478	0.0000	0.006
VTI2	4.262	3.381	0.0000	0.015
VTI3	4.287	3.278	0.0000	0.026
VTI4	4.320	3.170	0.0000	0.039
VTI5	4.366	3.053	0.0000	0.055

	High4				
	T (s)	V (km/s)	C3	C4	RMS (s)
VTI1	4.231	3.413	0.0000	0.0000	0.000
VTI2	4.237	3.242	0.0000	-0.0001	0.003
VTI3	4.247	3.073	0.0000	-0.0002	0.007
VTI4	4.261	2.903	0.0000	-0.0003	0.012
VTI5	4.283	2.730	0.0000	-0.0004	0.019

	High5					
	T (s)	V (km/s)	C3	C4	C5	RMS (s)
VTI1	4.231	3.413	0.0000	0.0000	0.0000	0.000
VTI2	4.237	3.242	0.0000	-0.0001	0.0000	0.003
VTI3	4.247	3.073	0.0000	-0.0002	0.0000	0.007
VTI4	4.261	2.903	0.0000	-0.0003	0.0000	0.012
VTI5	4.283	2.730	0.0000	-0.0004	0.0000	0.019

	High6						
	T (s)	V (km/s)	C3	C4	C5	C6	RMS (s)
VTI1	4.231	3.407	0.0000	-0.0001	0.0000	0.0000	0.000
VTI2	4.233	3.196	0.0000	-0.0002	0.0000	0.0000	0.001
VTI3	4.237	2.984	0.0000	0.0000	0.0000	0.0000	0.002
VTI4	4.243	2.774	0.0000	-0.0007	0.0000	0.0000	0.005
VTI5	4.256	2.563	0.0000	-0.0011	0.0000	0.0000	0.008

	Hellman				
	T (s)	V (km/s)	C4	C6	RMS (s)
VTI1	4.231	3.408	-0.0001	0.0000	0.000
VTI2	4.233	3.196	-0.0002	0.0000	0.001
VTI3	4.237	2.984	-0.0004	0.0000	0.002
VTI4	4.244	2.774	-0.0007	0.0000	0.005
VTI5	4.256	2.564	-0.0011	0.0000	0.008

4.2 TTI-series

Below one see the test results obtained by the diffraction-time functions for TTI-series.

	DSR		
	T (s)	V (km/s)	RMS(s)
TTI1	4.200	3.442	0.127
TTI2	4.229	3.378	0.121
TTI3	4.264	3.307	0.115
TTI4	4.307	3.227	0.112
TTI5	4.365	3.137	0.112

	High3			
	T (s)	V (km/s)	C3	RMS (s)
TTI1	4.197	3.434	-0.0018	0.061
TTI2	4.226	3.370	-0.0018	0.048
TTI3	4.262	3.300	-0.0018	0.037
TTI4	4.306	3.222	-0.0018	0.033
TTI5	4.364	3.132	-0.0017	0.043

	High4				
	T (s)	V (km/s)	C3	C4	RMS (s)
TTI1	4.190	3.391	-0.0018	0.0000	0.061
TTI2	4.210	3.278	-0.0018	-0.0001	0.047
TTI3	4.235	3.158	-0.0018	-0.0001	0.033
TTI4	4.267	3.031	-0.0017	-0.0002	0.022
TTI5	4.310	2.893	-0.0017	-0.0003	0.027

	High5					
	T (s)	V (km/s)	C3	C4	C5	RMS (s)
TTI1	4.188	3.366	-0.0047	-0.0001	0.0000	0.037
TTI2	4.208	3.260	-0.0042	-0.0001	0.0000	0.025
TTI3	4.234	3.146	-0.0037	-0.0001	0.0000	0.013
TTI4	4.266	3.024	-0.0030	-0.0002	0.0000	0.010
TTI5	4.309	2.891	-0.0023	-0.0003	0.0000	0.009

	High6						
	T (s)	V (km/s)	C3	C4	C5	C6	RMS (s)
TTI1	4.190	3.390	-0.0047	0.0000	0.0000	0.0000	0.037
TTI2	4.207	3.247	-0.0042	-0.0001	0.0000	0.0000	0.025
TTI3	4.229	3.103	-0.0037	-0.0003	0.0000	0.0000	0.012
TTI4	4.258	2.954	-0.0030	-0.0004	0.0000	0.0000	0.007
TTI5	4.297	2.800	-0.0023	-0.0006	0.0000	0.0000	0.009

	Hellman				
	T (s)	V (km/s)	C4	C6	RMS (s)
TTI1	4.189	3.375	-0.0001	0.0000	0.127
TTI2	4.207	3.237	-0.0002	0.0000	0.120
TTI3	4.229	3.096	-0.0003	0.0000	0.114
TTI4	4.258	2.952	-0.0004	0.0000	0.109
TTI5	4.297	2.800	-0.0006	0.0000	0.106

4.3 *VTI-series

Below one see the test results obtained by the diffraction-time functions for *VTI-series.

	DSR		
	T (s)	V (km/s)	RMS(s)
*VTI1	3.588	3.887	0.246
*VTI2	3.605	3.771	0.252
*VTI3	3.626	3.649	0.259
*VTI4	3.654	3.517	0.268
*VTI5	3.692	3.372	0.279

	High3			
	T (s)	V (km/s)	C3	RMS (s)
*VTI1	3.579	3.839	-0.0033	0.058
*VTI2	3.595	3.725	-0.0034	0.058
*VTI3	3.616	3.605	-0.0036	0.060
*VTI4	3.643	3.475	-0.0038	0.063
*VTI5	3.681	3.333	-0.0041	0.070

	High4				
	T (s)	V (km/s)	C3	C4	RMS (s)
*VTI1	3.595	3.971	-0.0033	0.0001	0.057
*VTI2	3.601	3.764	-0.0034	0.0000	0.058
*VTI3	3.608	3.559	-0.0036	0.0000	0.059
*VTI4	3.621	3.351	-0.0038	-0.0001	0.061
*VTI5	3.640	3.137	-0.0040	-0.0002	0.065

	High5					
	T (s)	V (km/s)	C3	C4	C5	RMS (s)
*VTI1	3.589	3.892	-0.0057	0.0000	0.0000	0.035
*VTI2	3.594	3.694	-0.0059	0.0000	0.0000	0.035
*VTI3	3.602	3.496	-0.0062	-0.0001	0.0000	0.035
*VTI4	3.614	3.296	-0.0066	-0.0001	0.0000	0.036
*VTI5	3.632	3.088	-0.0071	-0.0002	0.0000	0.038

	High6						
	T (s)	V (km/s)	C3	C4	C5	C6	RMS (s)
*VTI1	3.594	3.972	-0.0057	0.0001	0.0000	0.0000	0.035
*VTI2	3.596	3.720	-0.0059	0.0000	0.0000	0.0000	0.035
*VTI3	3.600	3.468	-0.0062	-0.0001	0.0000	0.0000	0.035
*VTI4	3.606	3.217	-0.0066	-0.0003	0.0000	0.0000	0.035
*VTI5	3.616	2.961	-0.0070	-0.0006	0.0000	0.0000	0.037

	Hellman				
	T (s)	V (km/s)	C4	C6	RMS (s)
*VTI1	3.593	3.920	0.0000	0.0000	0.246
*VTI2	3.595	3.679	-0.0001	0.0000	0.252
*VTI3	3.598	3.434	-0.0003	0.0000	0.258
*VTI4	3.604	3.187	-0.0005	0.0000	0.267
*VTI5	3.615	2.937	-0.0007	0.0000	0.277

4.4 *TTI-series

Below one see the test results obtained by the diffraction-time functions for *TTI-series.

	DSR		
	T (s)	V (km/s)	RMS(s)
*TTI1	3.554	3.814	0.359
*TTI2	3.753	3.736	0.361
*TTI3	3.602	3.649	0.365
*TTI4	3.635	3.550	0.369
*TTI5	3.679	3.435	0.377

	High3			
	T (s)	V (km/s)	C3	RMS (s)
*TTI1	3.532	3.719	-0.0047	0.110
*TTI2	3.555	3.646	-0.0048	0.098
*TTI3	3.582	3.563	-0.0050	0.084
*TTI4	3.616	3.469	-0.0052	0.070
*TTI5	3.660	3.360	-0.0055	0.057

	High4				
	T (s)	V (km/s)	C3	C4	RMS (s)
*TTI1	3.565	3.961	-0.0047	0.0001	0.108
*TTI2	3.581	3.826	-0.0049	0.0001	0.096
*TTI3	3.600	3.682	-0.0050	0.0001	0.083
*TTI4	3.625	3.526	-0.0052	0.0000	0.070
*TTI5	3.659	3.354	-0.0055	0.0000	0.057

	High5					
	T (s)	V (km/s)	C3	C4	C5	RMS (s)
*TTI1	3.549	3.763	-0.0093	0.0000	0.0001	0.066
*TTI2	3.566	3.659	-0.0091	0.0000	0.0001	0.056
*TTI3	3.587	3.543	-0.0089	0.0000	0.0001	0.045
*TTI4	3.613	3.415	-0.0087	0.0000	0.0001	0.031
*TTI5	3.649	3.270	-0.0086	-0.0001	0.0001	0.018

	High6						
	T (s)	V (km/s)	C3	C4	C5	C6	RMS (s)
*TTI1	3.562	3.867	-0.0093	0.0003	0.0001	0.0000	0.066
*TTI2	3.576	3.800	-0.0091	0.0002	0.0001	0.0000	0.056
*TTI3	3.594	3.632	-0.0089	0.0001	0.0001	0.0000	0.044
*TTI4	3.617	3.455	-0.0088	0.0000	0.0001	0.0000	0.031
*TTI5	3.649	3.268	-0.0086	-0.0001	0.0001	0.0000	0.018

	Hellman				
	T (s)	V (km/s)	C4	C6	RMS (s)
*TTI1	3.559	3.851	0.0000	0.0000	0.359
*TTI2	3.573	3.708	0.0000	0.0000	0.361
*TTI3	3.591	3.558	-0.0001	0.0000	0.365
*TTI4	3.614	3.400	-0.0002	0.0000	0.369
*TTI5	3.647	3.229	-0.0003	0.0000	0.377